nature portfolio

Peer Review File

The m^{6}A reader YTHDF2 regulates mRNA transport and axon outgrowth in developing neurons

Corresponding Author: Dr Ki-Jun Yoon

This file contains all reviewer reports in order by version, followed by all author rebuttals in order by version.

Version 0:

Reviewer comments:

Reviewer #1

(Remarks to the Author)
Koo B et al investigated the mechanisms of m6A RNA modification in mRNA transport to axons and its function in axon development in the perinatal brain. The authors identify YTHDF2 as the reader protein responsible for selective transport of m6A-mRNAs, and suggest YTHDF2 complexing with FMRP and Kif5c along microtubules to deliver cytoskeleton-associated mRNA transcripts to the distal axons and neurites, although whether the translation of those mRNA is regulated through YTHDF2 is unclear. The authors further identify m6A modification at single-nucleotide resolution with stoichiometry on mRNAs expressed in the P0 mouse forebrains. This data resource is novel and important for advancing our understanding of the function of m6A in the perinatal brain. The authors have employed a variety of omics techniques as well as single-molecular detection techniques in vivo and in vitro to elucidate the function and mechanisms of the pathway. The manuscript is well written and presents a novel mechanism for the m6A signaling to regulate perinatal axon development. However, some concerns need to be addressed. In particular, the function of YTHDF2 in axonal mRNA transport is unclear. No functional experiments on axonal mRNA localization related to YTHDF2 cKO were presented in the manuscript. Additional CC-seq in DF2-cKO mice and Tau (or other axonal marker) co-staining in cultured neurons can provide required evidence for the authors' claims. Furthermore, the translational fates of the localized mRNAs need to be studied to link the function of m6A-YTHDF2 to axonal development. What happens to the axonal expressions of proteins of Gap43, NCam1, Cntn1, Ank2, Actb?

Major concerns:

-Fig1 and 4 : Although an assumption that CAG-RFP and hCRE-IRES-GFP or DCX-GFP are always co-expressed can be made, the results can be highly dependent on the techniques and cells so need to be carefully validated. Although the authors included images with overlaid channels in extended figure 1d, it is unclear to the viewers whether GFP is expressed in all RFP-positive neurons (note that this can be compared at soma level since the intensity of IRES-GFP may be too low to be quantified at the axonal terminals; if the GFP is too low even in the soma, an immunostaining against GFP needs to added to amplify the signals. Alternatively, iCre immunostaining and confirmation of METTL14 reduction in the RFP+ cells can be shown; and it needs to be confirmed that iCRE is expressed in all RFP+ neurons (alternatively exclude neurons from analysis when iCRE can not be detected in them). It is unclear what promoter is used in the hCRE-IRES-GFP-RV construct. Fig1a : the intensity of RFP is less in M14 cKO electroporated cell soma than control cells, which could have led to the observation of less axon intensity; for example, in Fig1d, the contralateral axon bundle appears thicker in the cKO. In addition, the enlarged images in Fig1d do not match the insets in the same figure.

-Fig 3e - Fig4h - Fig 5e,g - Fig 6 b,d,f,h : Primary neurites/dendrites are being analyzed instead of axons in these figures. This causes a major problem to the authors' claim on the role of m6A and DF2 in axonal mRNA transport and development. Co-staining with an axonal marker such as Tau is required for identifying the correct subcellular compartment. In addition, the distance from the nucleus is not enough in smFISH; instead, the percentages of mRNA puncta in cell soma versus axon and/or number need to be shown and validated that Mettl14 or YTHDF2 KO do not decrease the total number of the mRNAs tested but alter distribution.

-Fig 3a. Although the CC-seq results suggest altered axonal mRNA population in the crossing axons, the same line (Mettl14 nestin-cre cross) has shown deficits in corticogenesis. Therefore it remains unclear whether the alteration is due to axonal transport of the RNA or disturbed corticogenesis. In lines 212-213, does the decrease or increase refer to the abundance of

the mRNA or distribution (I noted that in extended Fig 3, layer ⅔ cortex was dissected). Did the author sequence soma-derived mRNAs to normalize expression level?

-Fig 3g : The lysosomal live-cell tracking analysis shows only one and two moving lysosomes in the kymographs. This number seems low. How many spots were detected in a continuous axon on average? In addition, the transport needs to be evaluated by using anterograde and retrograde displacement lengths and speed. More importantly, lysosome transport is used as a control for mRNA transport but there is no live-cell imaging of any mRNA that the authors claimed to be dependent on m6A. Since mRNA transport is the main focus of the paper, it will be important to include mRNA live-cell imaging in the axonal compartment and compare non-target mRNA to target mRNAs.

-Fig 3. The rationale for narrowing down to YTHDF2 for further studies provided in the text (lines 254-263) is not sufficient for excluding YTHDF1 or YTHDF3. Previously reported YTHDF2 null mice (using ubiquitous expressed Cre) showed severe deficits in proliferation and differentiation of neural progenitor cells thus does not provide evidence of exclusive association of YTHDF2 to mRNA axonal transport (https://doi.org/10.1186/s13059-018-1436-y). The same paper has suggested the JAK-STAT cascade inhibitory genes contribute to neurite outgrowth. The behavior of this pathway in the YTHDF2 nestin-Cre and link to the axon deficits in YTHDF2 cKO need to be discussed. Furthermore, the statement in line 259-260 “Ythdf1 or Ythdf3 knockout mice did not exhibit obvious developmental abnormalities” was not consistent with the cited paper, which concluded “YTHDF1 and YTHDF2 have redundant functions in m6A regulation of cortical neurogenesis” (https://doi.org/10.1016/j.isci.2022.104908). A bioRxiv paper demonstrated the role of YTHDF1 in axon development through regulating translation of APC protein (https://www.biorxiv.org/content/10.1101/2020.11.14.382556v3). Given that multiple lines of evidence suggesting molecular interactions and functional redundancy of YTHDF1/2/3 have been reported in multiple cell contexts, the authors need to explore/confirm the involvement of YTHDF1 and YTHDF3 instead of drawing specific connections to YTHDF2 without further investigation.

-Fig 4. The nestin-cre mice are used for generating both Mettl14 cKO and YTHDF2 cKO. It will be helpful to conduct CC-seq in the YTHDF2 cKO mice and compare results to Mettl14 cKO. The results can further be used to clarify the observations in lines 298-299 “the stability of Ncam1, Cntn1, and Ank2 mRNAs increased in M14 cKO condition, while their stability decreased in the DF2 cKO condition” and further clarify the potential functional redundancy between the three cytoplasmic readers YTHDF1, 2, and 3. What is the role of YTHDF2 in axonal expression of L1CAM and NTNG1 proteins shown in Extended Data Fig 4h? Better representative images in extended figure 4h are needed. The yellow intensity in the opposite brain hemisphere shows increase in the DF2 cKO mice contrary to the other side.

-Fig 5. To strengthen the association between DF2 and microtubule through the motor proteins thus its function in transport, PLA DF2/KIF5c is more informative than PLA DF2/Tubb3 to demonstrate the interaction with the MT transport machinery. Better representative image is needed in Fig 5g since most of the green dots in the image are outside of the neurites. The analysis needs to be done in axons instead of dendrites/neurites. “Distance from the nucleus” alone is not sufficient for quantification or conclusion on axonal distribution. “Density” needs to be added.

--Line 320-325. The m6A-dependent interaction between YTHDF2 and microtubule-related proteins suggest that their association is through the modified mRNAs. Thus the data do not prove a more active role of YTHDF2 than piggybacking the mRNAs being transported. Live-cell imaging of mRNA in YTHDF2 cKO cells is critical.

-Fig 6. PLA FMRP/Tubb3 or YTHDF2/Tubb3 offers less specificity of microtubule association and RNA transport than PLA Kif5c. Additional live-cell imaging to monitor co-movement DF2/Kif5c and FMRP/Kif5c will better support the conclusions that YTHDF2 cooperates with FMRP to transport mRNAs into axons through Kif5c along the microtubule. The role of FMRP in YTHDF2/Tubb3 association or axonal mRNA transport is unclear. Is FMRP responsible for axonal mRNA transport as an independent reader protein?

Minor concerns:

- Line 53. It is unclear what “context” refers to in “context-guiding interactor”. Please be more explicit.

-Line 106. The sentence suggests interaction between YTHDF2 to m6A sites in the 3’UTR. Is the evidence shown in this paper or previous reports?

-Line 170. Replace “high” with “higher”.

- Please check the figure citations in the text. Misplaced citations were found. Where is Fig 2h cited? In line 159, is Fig 2h a typo? Did the authors mean to cite Extended Fig 2a?

-Fig 2. Adding a frequency distribution plot of m6A stoichiometry and the cutoff for separating m6A RNAs vs non m6A-RNAs can help the audience understand the overall m6A modification landscape.

-Line 194-195: “transcripts with high m6A stoichiometry were less stabilized than transcripts with low m6A stoichiometry in the M14 cKO neurons”. This observation is interesting and anti-intuitive. The authors stated in lines 202-203 “This suggests the presence of additional functions of m6A-tagging beyond mRNA degradation in the brain”. However the statement does not address the phenomenon. Additional discussions on potential regulatory mechanisms would be appreciated.
-Line 199. Which results suggest that “high m6A stoichiometry transcripts” are related to axon development? Please clarify.

-The gene names analyzed for qPCR need to be given in Lines 211 and 212.

-Lines 257-259. Possibly the embryonic expression of the YTHDFs is not as important as the perinatal stage (P0-P5) when axons develop. The input data in m6A-SAC-seq data may provide better rationale for this argument.

- Line 301. “Select” should be added in front of “mRNA”.

-Line 306. Again “Select” should be added in front of “mRNA” to avoid giving the audience the impression that this is a general phenomenon.

-Extended Fig. 1g: presenting the data as a percentage would be more meaningful. The exact N numbers should be kept in the figure legend or the text.

-Does each dot in Fig.3f, h, 4i, 5f, h, 6 e,g,i represent a single RNA puncta? How many neurons have contributed to the analysis?

-In line 288, the authors suggested that YTHDF2 affects axon branching, however, no experiment/quantification in the manuscript supports this claim. The claim can be removed or additional analysis can be provided.

-Extended Fig. 4a: beta-actin may not be the best loading control here given that its expression might be affected in the DF2 KO model.

-Extended Fig. 4b: beta-actin may not be the best loading control here given that its expression might be affected in the DF2 KO model.

-Extended Fig. 5: Negative controls using combinations of IgG with the other target protein antibody should be performed to validate the puncta.

-Lines 345-346. Fig 6a. The motifs of FXR2 and FMRP are similar to the m6A motif in m6A-SAC-seq. Given that both proteins have been identified as reader proteins of m6A in a previous report (https://doi.org/10.1038/nsmb.3462), these two proteins may be directly recruited to m6A-mRNAs independently of YTHDF2 binding.

Fig. 6f: Better representative images matching the quantification results are required.

Lines 420-421, the authors concluded that “YTHDF2 along the axon significantly decreases under m6A depletion condition (Fig. 5g-h)”. However, Fig 5g-h represents initial dendrites/neurites.

Reviewer #2

(Remarks to the Author)
Reviewer comments

This study investigates the role of m6A mRNA modifications in the regulation of neural development, particularly focusing on mRNA transport in developing neurons. This study demonstrates that knockout of Mettl14 in postmitotic neurons leads to impaired axonal projection, with RNA-seq and single-molecule in situ hybridization showing mislocalization of mRNAs in the neurites of neurons with m6A loss-of-function. Furthermore, the research identifies YTHDF2 as a key m6A reader protein that facilitates the distal transport of m6A-tagged mRNAs in callosal projection axons by interacting with FMRP, guiding the YTHDF2 complex to promote the efficient transport of m6A-tagged mRNA rather than its degradation. Although the topic is timely and has significant implications for advancing our understanding of mRNA regulation in neurons, the study has several limitations that affect its overall rigor and impact. The findings on YTHDF2’s role in mRNA transport and its interaction with FMRP are intriguing, but the lack of robust methodological detail weakens their support. This limited clarity and depth ultimately reduce the study's potential impact on the field.

Major comments:
(1) The interaction between FMRP and YTHDF2, as proposed in the study, is an intriguing finding. However, the authors fail to provide a clear explanation of how FMRP modulates YTHDF2's function in the context of mRNA transport. Is FMRP acting as a direct modulator of YTHDF2’s mRNA binding activity, or is it facilitating the transport process through indirect interactions? This lack of clarification leaves the reader uncertain about the specific mechanism by which FMRP influences mRNA transport. More detailed mechanistic insights, ideally supported by functional experiments, are needed to fully substantiate the proposed model.
(2) The study would greatly benefit from the inclusion of live imaging experiments to directly observe the co-transport of RNA-binding proteins (RBPs) and their associated mRNAs within the axons of developing neurons. While the manuscript suggests that YTHDF2 mediates mRNA transport, it remains unclear how the RBP interacts with the mRNA in real-time and how these dynamics unfold within the complex environment of the axon.
(3) The authors should provide a clear and comprehensive definition of the specific role of YTHDF2 in regulating mRNA, particularly distinguishing whether it primarily facilitates the degradation or transport of mRNA. Additionally, it is crucial to explain how these processes influence mRNA translation in neurons and, ultimately, how they impact neuronal function. Specifically, they should address whether YTHDF2’s action is associated with enhancing mRNA localization to axons for local translation or whether it leads to mRNA degradation, resulting in reduced protein synthesis. By clarifying these

mechanisms, the authors can establish a more direct link between mRNA regulation by YTHDF2 and the functional outcomes on neuronal processes such as axon guidance, synaptic plasticity, and neurodevelopment.
(4) The PLA (Proximity Ligation Assay) experiment, while useful for indicating proximity between YTHDF2 and its interacting proteins, does not provide sufficient evidence to confirm their co-localization or direct interaction. To strengthen the validation of these interactions, the authors should incorporate immunostaining experiments to visualize the precise subcellular localization of YTHDF2 and its interacting partners within neurons. This would provide clearer evidence of whether these proteins are truly co-localized in regions critical for mRNA transport, such as axons or growth cones. Additionally, co-immunoprecipitation (Co-IP) experiments are essential for confirming physical interactions between YTHDF2 and its binding partners at the molecular level. Co-IP would enable the authors to directly demonstrate that these proteins form a stable complex, supporting the proposed mechanism involving YTHDF2's role in mRNA transport.
(5) The differential role of YTHDF2 in axon growth requires further discussion. Previous research by Zhuang et al. (Molecular Psychiatry, 2023) found that Ythdf2 ablation led to mossy fiber overgrowth, while the present study reports that Ythdf2 knockout causes axonal growth defects. This discrepancy suggests that YTHDF2 may function differently across various neuronal subtypes or brain regions, potentially due to distinct mRNA targets, protein interactions, or local signaling contexts. It would greatly strengthen the manuscript if the authors could address these contrasting findings in their discussion, exploring possible mechanisms such as cell type-specific roles, developmental timing, or differential mRNA regulatory requirements. Clarifying these aspects will help readers better understand the complex, context-dependent functions of YTHDF2 in axonal growth regulation and could guide future research on m6A modification in neural development.
(6) The title could be refined to better reflect the focus of the study. As the primary emphasis is on how the m6A reader protein, specifically YTHDF2, mediates mRNA transport and influences axon outgrowth, it would be more accurate for the title to highlight the m6A reader protein's active role. The m6A modification serves as a marker rather than directly facilitating transport; thus, specifying YTHDF2's function would give readers a clearer understanding of the study's main findings. Adjusting the title accordingly would improve precision and help readers immediately grasp the study's central focus.

Minor comments:
(1) In Line 157, the statement "We identified 10,304 m6A sites in 3,830 genes (Fig. 2h, Extended Data Fig. 2j)" lacks alignment with Figure 2h, as no relevant information appears in this figure panel.
(2) In Figure 1f, the method used to define neuron morphology is unclear. The high density of neurons in the image makes it difficult to clearly trace the entire morphology of individual neurons. This could lead to ambiguity in interpreting the results.
(3) In Figure 1g, the text describes the "total length of neurites," but the panel itself shows the "longest neurite." This discrepancy should be addressed for consistency.
(4) In Figure 3e, the position of the soma should be clearly marked to provide context for the measurements and observations related to neurite outgrowth. This is important for understanding the spatial distribution of neurites and the directionality of growth. The same clarification should be applied to the other figures where soma position is relevant but not explicitly indicated.
(5) In Figure 3g, the live imaging of lysosomes would benefit from labeling the direction of the soma and the distal axon.
(6) In Figure 5b, the interaction between YTHDF2 and its associated proteins should be validated through additional biochemical experiments, such as co-immunoprecipitation (Co-IP), particularly for FMR1 and TUBB3.
(7) The study suggests that the knockout of YTHDF2 leads to decreased mRNA transport; however, this finding should be further validated using quantitative PCR (qPCR) from compartmentalized neuron cultures by analyzing mRNA levels in distinct neuronal compartments, such as the soma and axons.

Reviewer #3

(Remarks to the Author)
In this manuscript, Koo and colleagues explore the roles of m6A RNA methylation and the YTHDF2 proteins in axonogenesis and brain development. They make several claims, most of which are well substantiated by their date. They first use a Mettl14 KO paradigm to show that loss of M14 leads to a reduction in the number of axon projections and arborization in vivo and to reduce growth cones dynamics in vitro. To gain further insights in the role of m6A in these processes, m6A-SAC-seq is then used to map and quantify m6A in the forebrain of mice pups. This analysis reveals that that m6A is enriched in 3'UTRs of mRNAs coding for proteins with known localization and functions in axons and dendrites. Surprisingly, high m6A stoichiometry RNAs are less stabilized than low stoichiometry RNA in M14 cKO. Through the sequencing of RNAs extracted from the corpus callosum (CC-seq), RNAs dependent on m6A for their localization are identified and validated using FISH in primary neurons. The authors then repeat some of these experiments using YTHDF2 cKO mice, finding similar effects on axon growth and guidance. Overall, these finding convincingly shows that m6A and YTHDF2 may have functions beyond the control of mRNA stability in neurons (localization), corroborating evidence found in other neuronal systems. The authors next performed an IP-MS experiments to explore the mechanisms by which YTHDF2 and m6A contribute to axonogenesis. They identify 283 proteins with reduced interactions in M14 cKO mice, notably KIF5C, TUBB2B, TUBB3, MAP2, in addition to RBPs FXR1, FMR1 and FUS. Some of these interactions are then confirmed using proximity ligation assays in cultured neurons. Overall, I find that the last two figures are weaker than the first 4. Nonetheless, the data presented are novel and addresses an interesting and important topic that remains debated in the field. As such I think that a large audience would show interest in this paper. However, I have some minor comments that should be addressed before publication in order to improve the quality of the manuscript:

Minor points
• m6A-SAC-seq: m6A-SAC-seq is a recently developed method for the profiling of m6A. The data is interesting and the overlap with other existing datasets is reassuring. However, I found that the details provided in method sections were

lacking. The authors should specify the number of biological replicates (This was only found in the GEO dataset). Moreover, it is unclear how replicable this approach is. Are all identified sites found in both biological replicates? Overall, more details would help the readers to understand and replicate these experiments if needed.
o At line 157, the authors indicate: “m6A peaks”. I think this should be replaced with “sites” since m6A-SAC-seq has single-nucleotide resolution.
• RNA stability assays: RNA stability cannot be determined using only two points on a curve as RNA decay is not linear. At line 185, the author could change calculate to estimate.
• Figures 3b, 3c and 3d are called before figure 3a in the text.
• CC-seq: Extracting the exact same regions in all 3 biological replicates may be challenging. Moreover, I expect that glial cells residing in the CC will also be extracted. What fraction of the RNAs extracted is expected to come from axons in these samples? A filtering step to remove RNAs abundant in glia would be useful. For example, see Cajigas et al., Neuron 2013, who did such an analysis for the hippocampal neuropil.
• Mass spectrometry: How many biological replicates were performed? Is the data deposited? Additional details on these samples should be provided. Since the authors indicate enrichment and depletion of in M14 cKO, this information is important, and these experiments should be performed in multiple replicates. Otherwise, the results could be caused by changes in the negative IgG control.
• smFISH: a linear map of targeted RNAs and their mapped m6A sites should be provided in supplements. This would help the reader to assess the number of sites and the stoichiometry of m6A on targets which require m6A for their localization.
• It is unclear what is being quantified in fig 4i, 5f, 5g, 6e, 6g, 6i. Are these observations for all mRNA/PLA signals across all cells in all biological replicate? It would be better to also present the data in individual experiments and cell to assess the variability between each cell.
• Overall, I do not think that the data presented for Figure 6 is convincing.
o The identified motif (NGACNNN) for FXR2 and FMRP is very similar to the m6A motif, which could explain its enrichment. Is there an enrichment for the canonical DRACH m6A motif?
o Additional images for YTHDF2 PLA with FMRP should be provided (as is presented in figure S5 for DF2-CNOT1).
o The signal intensity in the images presented in fig. 6d is drastically different. Are the observed effects caused by differences in expression or of cell-to-cell variability? This signal is not represented in the quantification in figure 6e. Indeed, I would expect many interactions near the nucleus in control cells.
o FMRP controls the localization of many RNAs without YTHDF2. Is the reduction in localization in fig. 6i dependent on YTHDF2? Does a double KD/KO potentiate this effect?
o Overall, I think that more/better quality images and their deposition in a repository would increase the confidence in this data.

General comments:
I find the finding on the RNA stability in M14 cKO and DF2 cKO cells very interesting. It seems that most changes in stability occur on RNAs that do not contain m6A. Rather than seeing a shift of the ECDF curve to the right, we see a change in its shape: the most stabilized and destabilized transcripts do not contain m6A sites. To me, this suggests that in mature neurons, the main function of m6A might not be RNA decay, but rather other functions such as trafficking or translational control. Since this study uses both in vivo samples (subjected to potential differentiation effects) and cultured neurons, it would be interesting to discuss potential differences between m6A/DF function in dividing cells and post-mitotic neurons.

Version 1:

Reviewer comments:

Reviewer #1

(Remarks to the Author)
In the revised manuscript, the authors have performed new experiments and analysis, and improved the overall quality of the manuscript. However, evidence to fully support some of the authors’ major claims remains insufficient.
A general concern in the manuscript is that primary dendrites are examined in the analyses instead of axons and the authors call them “distal neurites”. This is seen in the PLA, immunostaining, morphological analysis, live-cell MS2 tracking experiments, etc. I highly recommend the authors to use consistent nomenclatures.
Another concern is the lack of evidence to claim a specific role of YTHDF2 in promoting distal mRNA transport. Expression levels of the three YTHDF cytoplasmic reader proteins were similar at the developmental stage of the study based on TPM measurement. A previous report has revealed the role of YTHDF1 in controlling APC expression and APC-mediated axonal mRNA transport in hippocampal neurons and cortical neurons (PMID: 40402742; this publication should be cited given its direct relevance to the current work). The authors proposed that YTHDF2 promote distal transportation of select mRNAs through its interaction with FMRP and KIF5C, but evidence showing that the other two reader proteins do NOT interact with FMRP or HUBB3 or KIF5C was not presented. In fact, an interaction between YTHDF1 and FMRP regulated by the phosphorylation state of FMRP has been reported (PMCID: PMC10872974). If the same logic applies, what mechanisms enable YTHDF2 to promote mRNA transport, whereas YTHDF1 does not?
Finally, the mechanism of promoting axonal mRNA transport by YTHDF2 remains unclear. Interactions between YTHDF2 and microtubule, motor proteins, and FMRP do not suggest a positive role of YTHDF2 for transportation. The evidence that does support a positive role of YTHDF2 is the KD and live-cell imaging experiments, however the mechanistic link is unaddressed in these experiments. A shift of mRNAs between granule complexes upon YTHDF2 KD will address this question better than FMRP KD.

Minor Comments:

1. Fig 1b, statistics appears only to be applied at the distal part after midline. Please add statistics to the proximal part before midline for a full examination.

2. Fig 1d, RFP signals in the contralateral cortex in cKO appear in abundance next to the inset, possibly comparable to Het (M14f/+ if I understood correctly). The authors need to explain why those signals were excluded from the analysis. Is it possible that the axons are mistargeted to the neighboring region?

3. Fig 1f, the DIV6 cortical neurons appear to have tau staining in the dendrites M14 cKO, resulting in very distinct morphology between Control and M14 cKO. For projection and length analysis, a "filler" will serve better than tau staining. Is it possible that tau is subcellularly mistargeted?

4. Fig 1k, For "Transient protrusion through axon projection/ Hour" quantification, please demonstrate the representative images to help readers understand what is being quantified.

5. Fig 3b, this figure compares stabilization with localization in M14cKO/ WT, but the authors do not clarify if the localization is for neurites or axons.

6. Fig 3g, earlier smFISH experiments show staining(e) and quantification of distance from soma (f) for the transcript of interest but panel g mentions the relative density of smFISH puncta in neurites which is not shown in e or in extended figures.

7. Fig 3i-n,Why different time stamps (3i, 3l) are displayed when showing the anterograde/retrograde/interrupted RNA localization. Also, what is "interrupted"? For how long were the granules tracked? Please clarify.

8. Fig 3j, m, it appears that there are differences in the retrograde RNA location as well, however this was not addressed by the authors. A graph before normalization may also help address this question.

9. Fig 4b: Statistical analysis could be applied before the "midline" in order to highlight the significant difference at the contralateral side.

10. Fig 4f: Please clarify in the text/methods what "transient protrusion" means in this panel.

11. Fig 4h, The panel discussing M14 when the focus is YTHDF2's role in axonal projection, is confusing. Is this information important for interpreting the proceeding panels?

12. Fig 4l, It would be helpful to show a representation of the "retrograde" movement and what its relevance is to DF2's role in axonal trafficking.

13. Fig 4j-m: A lot of information (eg. n numbers, p-values) is given. I suggest the authors organize the information to be given in a more concise/organized manner.

14. Fig 5b, According to the text, 283 proteins showed reduced DF2 interaction while 87 had enhanced interaction in DF2-cKO versus WT mice. This is not reflected in the graph.

15. Fig 5 legend - "Red circles highlight proteins involved in transport system as categorized by gene ontology analysis" - labeling method of 'transport-relevant' / microtubule proteins is confusing to readers.

16. Fig 5f, g: Experiments done on N2A and HEK293T cells show that DF2 and KIF5C or FMRP, respectively, interact with one another. However, these experiments do not show their interactions are dependent on m6A, particularly m6A modifications on the interacting mRNAs.

17. Fig 5k-m: Transition from DF2-TUBB3 interaction (5h-j) to the role of KIF5C in this interaction is unclear.

18. Fig 6d is insufficient to support the claim that YTHDF2 interacts with two protein complexes (presumably CNOT1-DF2-FXR versus DF2-FMRP-KIF5C). A staining of CNOT1 – DF2 – FMR1 – quantifies co-localization is required. SuperRes imaging of either SIM or STORM would be helpful. Biochemical analysis such as co-immunoprecipitation will also do.

19. Fig 6 (d-e): There is a typo in the figure legend which does not match the quantification in the figure. It says "YTHDF2-CNOT1 associations decreased in Fmr1 KD mouse primary neurons.", whereas there is an increase following Fmr1 KD.

20. Lines 22, 41, 147, etc: replace "base-pair" with "nucleotide".

21. Line 91, 111, PMID: 40402742 directly addresses this question.

22. Line 139 "formation of distal neuronal processes is impaired". What mechanisms may support specific deficits in forming "distal" neuronal processes?

23. Line 196-200, better suit discussion.

24. Line 238-239, why not translation of the target proteins?

25. Line 240-253. m6A-Actb-MS2 reporter showed an overall reduced motility in M14 KO neurons, whereas deltam6A-Actb-MS2 showed deficits in anterograde movement. How to reconcile the difference in phenotypes?

26. Lines 307-308, it is unclear what dataset “m6A-modified transcripts” refer to or where the mRNA stability dataset is used.

27. Lines 315, 321, replace “selected” with “select”.

Reviewer #2

(Remarks to the Author)
The revisions satisfactorily resolve all issues. the manuscript is now suitable for publication.

Reviewer #3

(Remarks to the Author)
The revisions to the text and figures have greatly improved the manuscript. My concerns have all been addressed and I am now fully satisfied with the manuscript.

Mathieu Flamand
Assistant Professor, Université Laval

Version 2:

Reviewer comments:

Reviewer #1

(Remarks to the Author)
I am satisfied with the revised manuscript.

Open Access This Peer Review File is licensed under a Creative Commons Attribution 4.0 International License, which permits use, sharing, adaptation, distribution and reproduction in any medium or format, as long as you give appropriate credit to the original author(s) and the source, provide a link to the Creative Commons license, and indicate if changes were made.
In cases where reviewers are anonymous, credit should be given to 'Anonymous Referee' and the source.
The images or other third party material in this Peer Review File are included in the article’s Creative Commons license, unless indicated otherwise in a credit line to the material. If material is not included in the article’s Creative Commons license and your intended use is not permitted by statutory regulation or exceeds the permitted use, you will need to obtain

permission directly from the copyright holder.
To view a copy of this license, visit https://creativecommons.org/licenses/by/4.0/

We sincerely thank the reviewers for their insightful comments and for recognizing the importance of our study. This letter provides point-by-point responses to all reviewer comments, along with descriptions of the new experiments and computational analyses we have conducted. The original reviewers' comments are shown in black, followed by our responses in blue. Revisions to the text and figures appears in red within the yellow highlights, and paragraph line numbers in the revised manuscript are indicated in cyan. To address the reviewers' comments, we have also revised the figure numbering.

Point-to-Point Responses to Reviewers' Comments

Reviewer #1 (Remarks to the Author):

Koo B et al investigated the mechanisms of m6A RNA modification in mRNA transport to axons and its function in axon development in the perinatal brain. The authors identify YTHDF2 as the reader protein responsible for selective transport of m6A-mRNAs, and suggest YTHDF2 complexing with FMRP and Kif5c along microtubules to deliver cytoskeleton-associated mRNA transcripts to the distal axons and neurites, although whether the translation of those mRNA is regulated through YTHDF2 is unclear. The authors further identify m6A modification at single-nucleotide resolution with stoichiometry on mRNAs expressed in the P0 mouse forebrains. This data resource is novel and important for advancing our understanding of the function of m6A in the perinatal brain. The authors have employed a variety of omics techniques as well as single-molecular detection techniques in vivo and in vitro to elucidate the function and mechanisms of the pathway. The manuscript is well written and presents a novel mechanism for the m6A signaling to regulate perinatal axon development. However, some concerns need to be addressed.

We appreciate the reviewer's summary and critiques. Below, we address all of reviewer's comments in detail.

1) In particular, the function of YTHDF2 in axonal mRNA transport is unclear. No functional experiments on axonal mRNA localization related to YTHDF2 cKO were presented in the manuscript. Additional CC-seq in DF2-cKO mice and Tau (or other axonal marker) co-staining in cultured neurons can provide required evidence for the authors' claims.

We fully agree with the reviewer's point. Although we analyze smFISH/PLA signals on mCherry positive neurite-like structure, it is necessary to distinguish the neurite/axon. To address this concern, we repeated the experiments with co-staining for the axonal marker Tau and re-assessed the quantifications in Tau^+ axons. The revised analyses yielded results consistent with our original conclusions. Accordingly, we have updated the corresponding figures and statistical data in the revised Fig. 3–6 and revised Extended Data Fig. 5-8. In addition, we have corrected the terminology from *neurites* to *axons* throughout the manuscript text, figure legends, and Methods. These new results further strengthen the scope and impact of our study.

In addition, we performed CC-seq in *Ythdf2* cKO mice. The Ythdf2 CC-seq data revealed a transcriptional profile comparable to that observed in the Mettl14 cKO CC-seq (Reviewer Fig. 1a).

We identified 565 m⁶A-modified genes enriched among the downregulated genes, while 237 m⁶A-modified genes enriched among the upregulated genes. This data indicating that YTHDF2 depletion reduces the localization of m⁶A-modified mRNAs to distal axons.

Furthermore, GO and GSEA analyses showed that downregulated genes were significantly associated with synapse organization and axonogenesis, whereas upregulated genes were linked to housekeeping processes such as cell division and chromosome organization (Reviewer Fig. 1b-d). These results confirm our original conclusion that YTHDF2 acts as the key m⁶A reader responsible for transporting m⁶A-tagged transcripts to axons.

We respectfully note that we intend to use the CC-seq dataset from *Ythdf2* cKO mice in a separate ongoing study. Therefore, we prepared this figure solely for the reviewer's evaluation to address the current question, but have not included it in the revised manuscript.

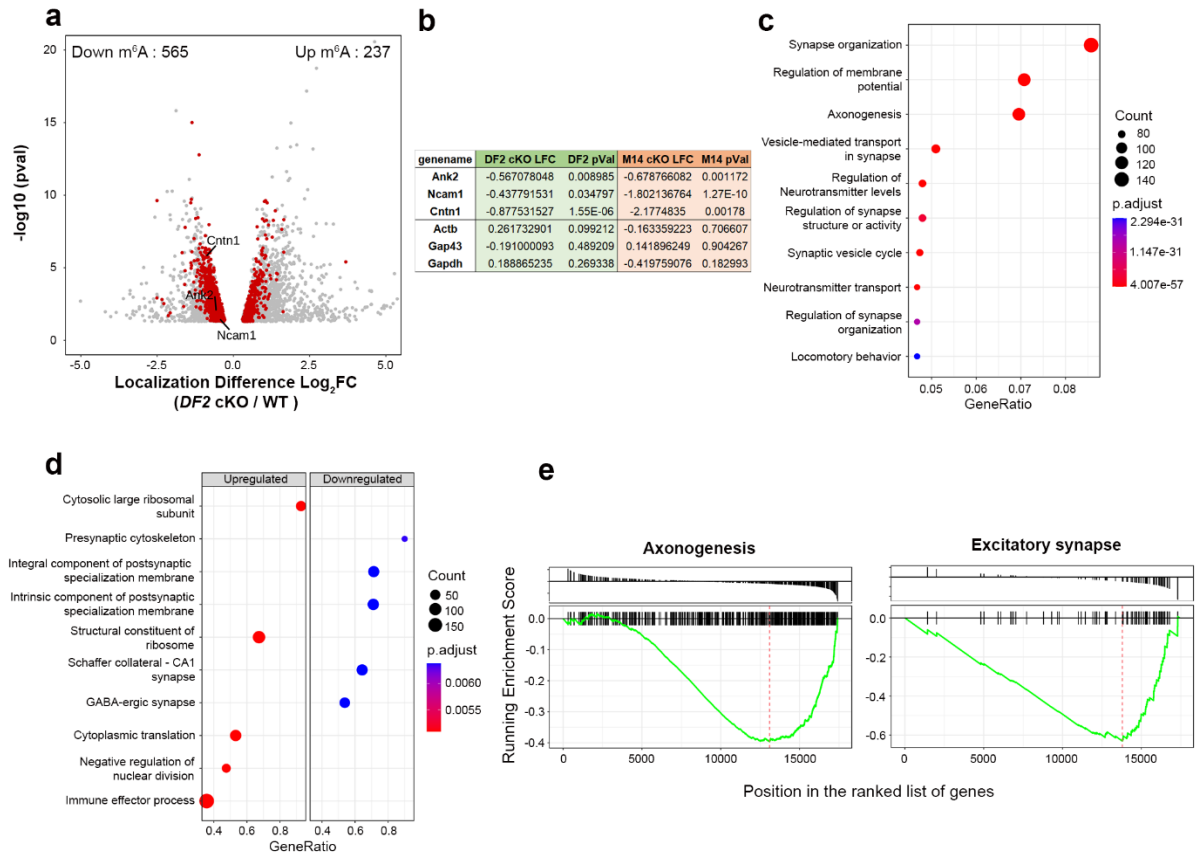

genename	DF2 cKO LFC	DF2 pVal	M14 cKO LFC	M14 pVal
Ank2	-0.567078048	0.008985	-0.678766082	0.001172
Ncam1	-0.437791531	0.034797	-1.802136764	1.27E-10
Cntn1	-0.877531527	1.55E-06	-2.1774835	0.00178
Actb	0.261732901	0.099212	-0.163359223	0.706607
Gap43	-0.191000093	0.489209	0.141896249	0.904267
Gapdh	0.188865235	0.269338	-0.419759076	0.182993

Reviewer Fig. 1. The *DF2* cKO CC-seq data revealed a transcriptional profile comparable to that observed in the *M14* cKO CC-seq

(a) The volcano plot shows genes that are depleted and enriched in the corpus callosum of P4 *DF2* cKO mice. Red indicates m⁶A-modified genes and targets of interest are highlighted. **(b)** The table summary of *DF2* cKO CCseq and *Mettl14* cKO CCseq result of the target RNAs. **(c)** Gene Ontology analysis of downregulated DEGs. **(d-e)** Gene Set Enrichment Analysis (GSEA) for the position in the DEG fraction ranked genes. The summary dot plot for

the position in the DEG ranked genes were represent on (d) and specific term were represented on (e).

2) Furthermore, the translational fates of the localized mRNAs need to be studied to link the function of m6A-YTHDF2 to axonal development. What happens to the axonal expressions of proteins of Gap43, NCam1, Cntn1, Ank2, Actb?

Thank you for raising this important point. As suggested, we examined the expression of GAP43, ANK2, NCAM1, and ACTB by immunostaining in the growth cones of differentiating neurons. Notably, the relative protein levels of ANK2, NCAM1, and ACTB were reduced upon Mettl14 depletion, while GAP43 showed no significant change. This result indicates that m^{6}A-mediated mRNA transport is essential for proper axonal expression of these target proteins. We included the results in the text and the Revised Extended Data Fig. 5a-b.

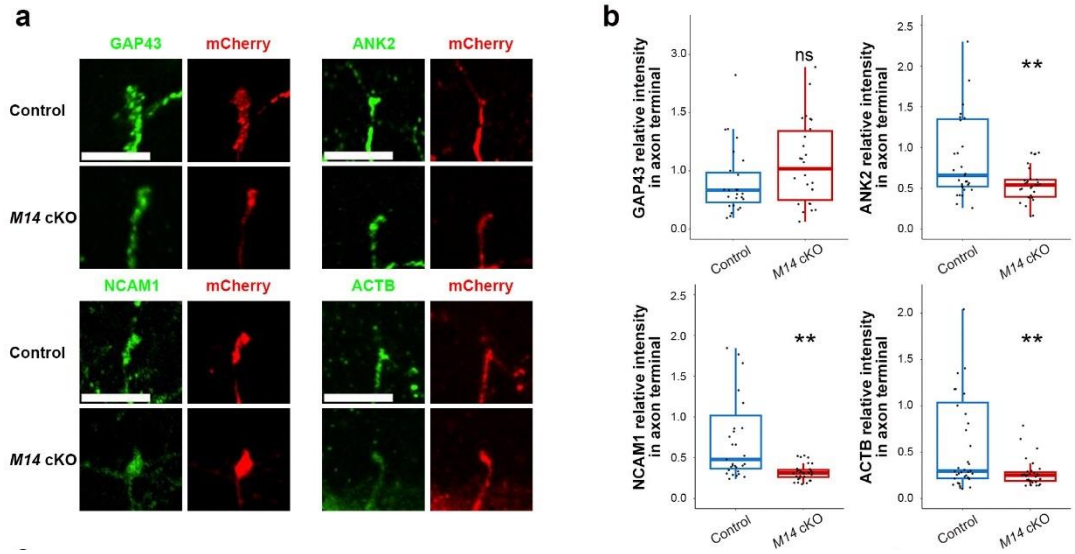

Revised Extended Data Fig. 5. Loss of Mettl14 leads to a reduced neuronal gene expression and localization in axons. (a-b) *Mettl14* cKO showed reduced expression of the target protein in the axon terminal. Shown in (a) the target protein and mCherry ICC image (Scale bar: 10μm) and the quantification of the relative intensity was shown in (b) (GAP43: Control n=27, *Mettl14* cKO n=26, *P*=0.06521; NCAM1: Control n=31, *Mettl14* cKO n=32, *P*=0.002766; ANK2: Control n=31, *Mettl14* cKO n=30, *P*=0.004337; ACTB: Control n=40, *Mettl14* cKO n=31, *P*=0.01434). Significance was evaluated using two-tailed unpaired Student's t-tests (b), ns, not significant; **P < 0.01.

Changes in the text:

(Line 237-239) Consequently, the axonal protein levels of NCAM1, ANK2, and ACTB were relatively reduced at growth cones, indicating that m^{6}A-mediated mRNA transport is essential for proper axonal expression of these target proteins (Extended Data Fig. 5a-b).

Major concerns:

3) Fig1 and 4 : Although an assumption that CAG-RFP and hCRE-IRES-GFP or DCX-GFP are always co-expressed can be made, the results can be highly dependent on the techniques and cells so need to be carefully validated. Although the authors included images with overlaid channels in extended figure 1d, it is unclear to the viewers whether GFP is expressed in all RFP-positive neurons (note that this can be compared at soma level since the intensity of IRES-GFP may be too low to be quantified at the axonal terminals; if the GFP is too low even in the soma, an immunostaining against GFP needs to added to amplify the signals. Alternatively, iCre immunostaining and confirmation of METTL14 reduction in the RFP+ cells can be shown; and it needs to be confirmed that iCRE is expressed in all RFP+ neurons (alternatively exclude neurons from analysis when iCRE can not be detected in them). It is unclear what promoter is used in the hCRE-IRES-GFP-RV construct.

Thank you for your thoughtful and detailed observations. In utero electroporation (IUE) is a widely used technique, and numerous studies have demonstrated the reliable co-expression of multiple constructs when mixed together in the injection solution [1–3]. To further clarify this point, we have added new data showing co-immunostaining of Dcx-iCre-GFP and CAG-RFP in electroporated brains. As shown in Extended Figure 1f, GFP is expressed in most RFP-positive neurons, confirming efficient co-transfection. (Revised Extended Data Fig.1f).

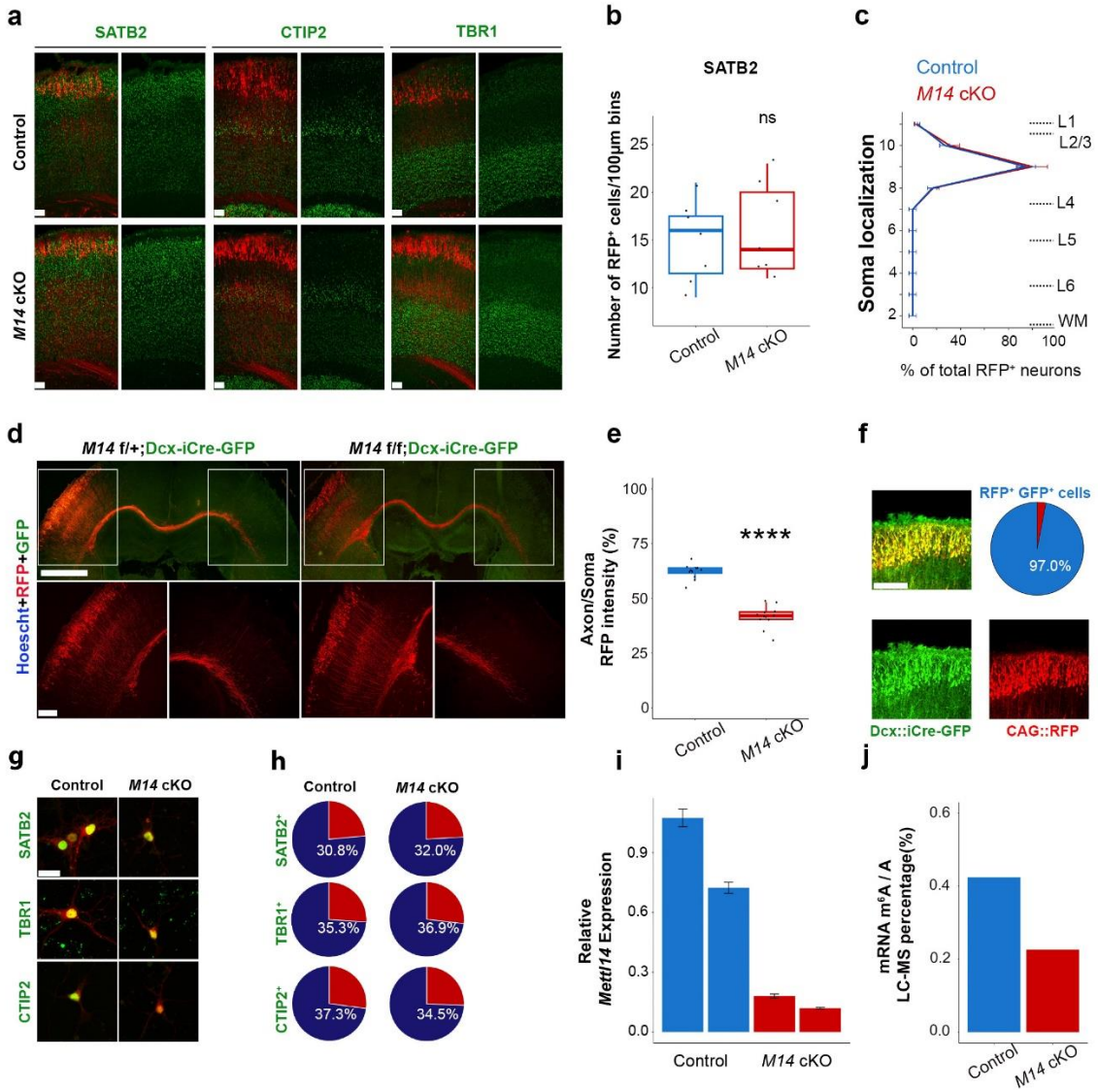

Revised Extended Data Fig. 1. Loss of *Mettl14* leads to reduced contralateral axon projection.

(a-c) Confocal images of SATB2 (layer 2/3), CTIP2 (layer 5), and TBR1 (layer 6) in P5 mouse brain coronal sections are shown in (a) (Scale bar: 50μm). Quantification of the number of SATB2$^+$RFP$^+$ cells is shown in (b) (n = 6 for each, P = 0.651), and the migration of upper-layer neurons is shown in (c). **(d-e)** Corpus callosal axon projection in control and *M14* cKO P5 brains, examined by *in utero* electroporation with pCAG-RFP plus Dcx-CRE-IRES-GFP plasmids. Shown in (d) are neuronal migration and axonal arborization in the S1 region (upper panel scale bar: 500μm, lower panel scale bar: 100μm). (e) The integrated density of the RFP signal per axon per soma was quantified (n = 10 for each, P = 4.37e-11). **(f)** Confocal image to validate plasmid co-IUE efficiency (Scale bar: 200μm). The percentage of GFP$^+$; RFP$^+$ cells were quantified (n=200). **(g)** Cortical markers SATB2, CTIP2, and TBR1 in *M14* cKO and control upper-layer neurons after AAV-mCherry-IRES-Cre virus infection at DIV1 and fixation at DIV6. The percentage of mCherry$^+$ cells were quantified in (h). **(i)** Validation of *M14* cKO in cortical neurons at DIV6 by qPCR. Values represent mean ± SEM after being normalized by GAPDH expression. **(j)** Validation of m^{6}A depletion in cortical neurons at DIV6 by LC-MS analysis. Significance was evaluated using two-tailed unpaired Student's t-tests (b, e). ns, not significant; ****P < 0.0001.

Additionally, we repeated the immunostaining using METTL14 and GFP antibodies on the previously hCRE-IRES-GFP–electroporated P5 brain sections to further validate the efficiency of Cre-mediated METTL14 ablation in GFP-positive cells. Our analysis showed that METTL14 signals were largely undetectable in GFP-positive cells of the *Mettl14*$^{f/f}$ samples, whereas the control group and GFP-negative cells exhibited clear METTL14 expression (Reviewer Fig. 2).

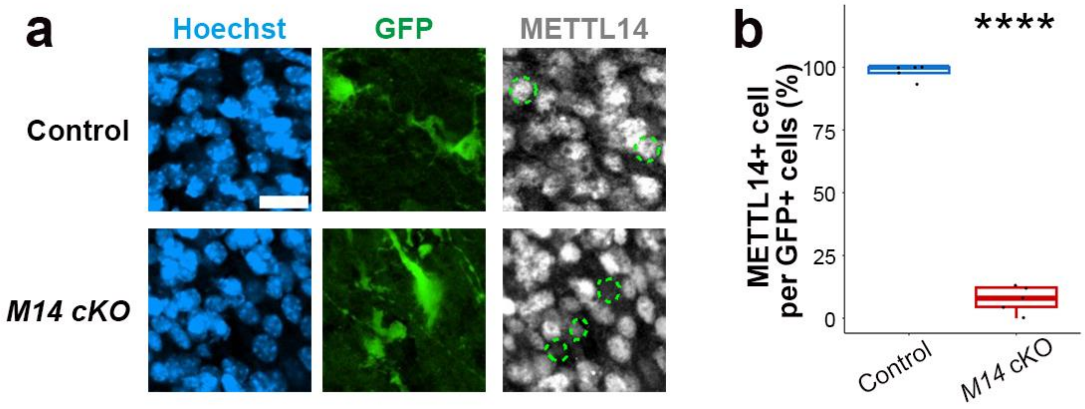

Reviewer Fig. 2. Efficiency of in utero electroporation of Cre plasmid in reducing Mettl14 expression in the *Mettl14*$^{f/f}$ brain.
(a-b) Confocal images showing GFP and METTL14 expression in the P5 mouse cortex. Cre recombination efficiency was assessed by in utero electroporation with Dcx-CRE-IRES-GFP plasmids (Scale bar: 50μm). The percentage of METTL14^{+} cells per GFP^{+} Cells was quantified in (b). (n = 5 per group, P = 8.36 x10^{-10})

Last, we apologize for not mentioning the correct promoter of the hCRE-IRES-GFP-RV construct, which has a CMV promoter [4]. We added more detailed information in the method section, including all plasmids used in this research and the cloning strategies.

Changes in the text:
(Line 514-529)
Plasmid information
To knockout *in vivo* and *in vitro*, hCRE-IRES-GFP-RV[5] (From Dr. William Paul at the National Institute of Health), Dcx-CRE-IRES-GFP[17] (From Dr. Ulrich Mueller at Johns Hopkins University), CAG-RFP (From Dr. Hongjun Song at the University of Pennsylvania), and pAAV-mCherry-IRES-Cre (Addgene, #55632) were used. To knock down the YTHDF1, YTHDF3, KIF5C, and FMRP, the sh sequence was cloned into the pUEG vector. Further, sh*Fmr1* sequence was cloned into the pUEtdTomato vector (From Dr. Hongjun Song at the University of Pennsylvania)[6]. For the Co-IP, pT7-EGFP-HsYTHDF2 plasmid (Addgene, #148310) and each of pFRT-HA-FLAG-hFMRP (Addgene, #48690) and pRK5-myc-KIF5C (Addgene, #127618) were used. For the RNA live imaging, we used phage-ubc-nls-ha-tdMCP-gfp (Addgene #30649), and pcDNA-puro-TagBFP-β-ACTIN-3′UTR-24xMS2 (Addgene #205161). For the point-mutant reporter (BFP-Actb-3′UTRΔm^{6}A-MS2x24), we used the Site-directed Mutagenesis kit (Enzynomics, EZ004S) according to the manufacturer's instructions. In brief, the reporter plasmid was amplified using a pair of

primers that substituted the conserved m^{6}A site with a cytosine residue. Next, the PCR product was ligated and transformed into E. coli for selection and amplification.
All detailed sequence information wrote in supplementary table S6.

4) the intensity of RFP is less in M14 cKO electroporated cell soma than control cells, which could have led to the observation of less axon intensity; for example, in Fig1d, the contralateral axon bundle appears thicker in the cKO.

We appreciate the reviewer's feedback and apologize for not providing a clearer explanation of Figures 1a and 1d. We acknowledge the reviewer's concern that axonal RFP intensity is influenced by soma RFP intensity. In the original submission, we had already used normalized axonal RFP intensity to soma RFP intensity with sufficient replicates, demonstrating statistically significant differences (Fig. 1b and 1c). We added a more detailed explanation in the Methods section describing how the axonal RFP signals were normalized to the soma RFP signals.

Changes in the text:
(Line 816-821)
Image analysis
For image acquisition and quantification, we used the open-source Fiji [7]. To ensure linearity and consistency across samples, minimum and maximum threshold signals were determined. Quantification was performed to obtain binary values from pixel intensity. Callosal axon projection and contralateral fluorescence intensity values were normalized to relative RFP-positive soma at the ipsilateral position [8].

5) In addition, the enlarged images in Fig1d do not match the insets in the same figure.

We apologize for the incorrect description of the lower panel in Figure 1d. The lower panel does not show enlarged images of the insets in the upper panel; instead, it presents z-projected images at higher magnification, focusing on the areas outlined by the insets.

We have revised the Figure 1 legend accordingly:

(Line 895-896) The lower panels display z-projected images at higher magnification of axonal arborization in the S1 region.

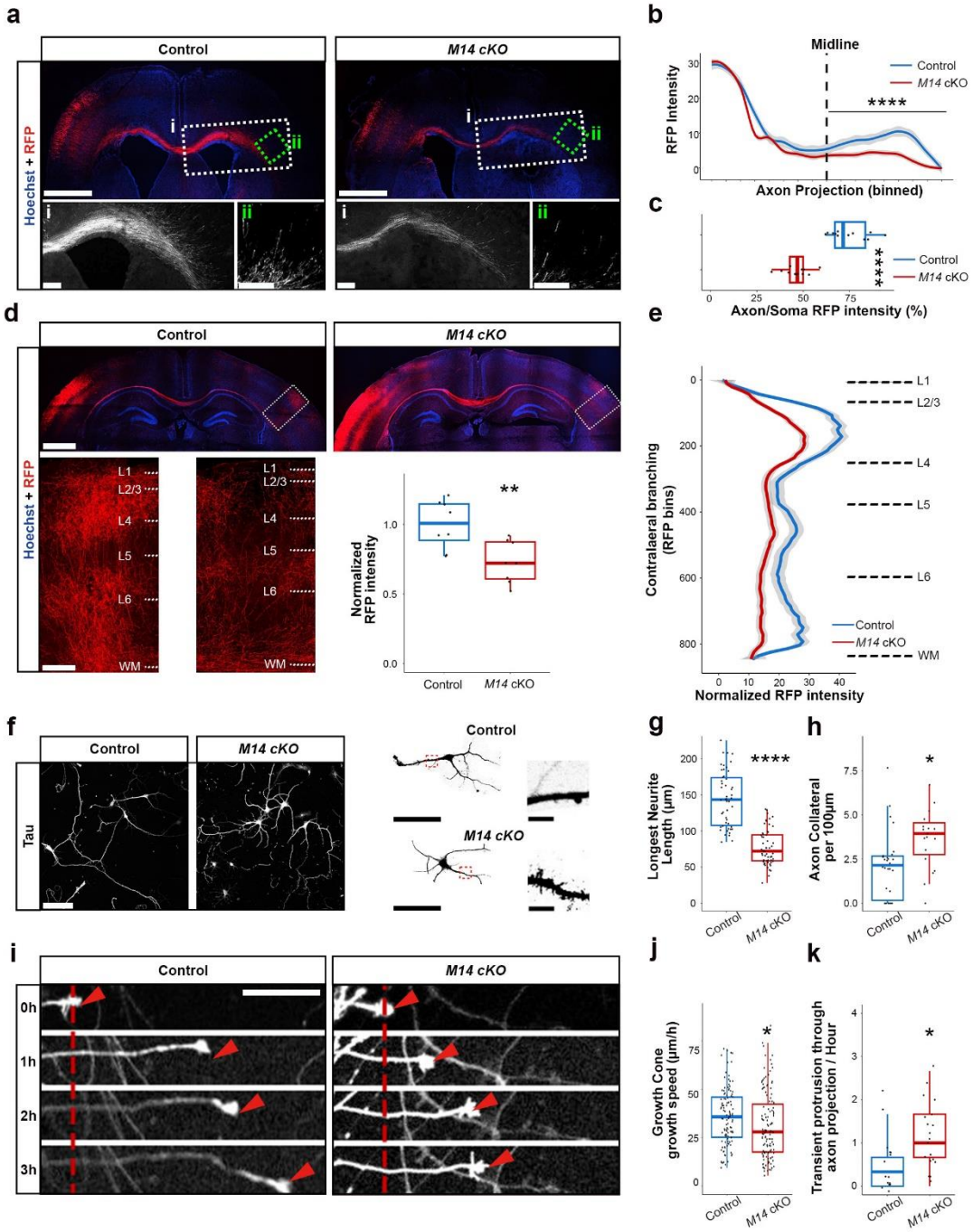

Revised Fig. 1. *Mettl14* deletion during corticogenesis leads to reduced axon projection, shorter neurite length, increased axon collaterals, and slower growth cone dynamics. **(a-c)** Corpus callosal axon projection in control (*Mettl14*$^{+/f}$) and *Mettl14*$^{f/f}$ P5 brains after electroporation of hCRE-IRES-GFP-RV and pCAG-RFP plasmids at E14.5 **(a)** The upper panel shows ipsilateral to contralateral axon projections crossing the white matter and corpus callosum area in coronal sections. The lower panels (i, ii) are selected to magnify the corpus callosum and projected axon terminals (scale bars: 1 mm, i, ii; scale bars: 200 μm). **(b)** The frequency distribution plot represents RFP intensity during axon projections from the ipsilateral to the contralateral position. (n=3 for each, confidence level=0.99, *P*=2.13e-14). **(c)** The integrated density of the RFP signal per soma was quantified. (n=12 for each, *P*=8.14e-08). **(d)** Corpus callosal axon projection in control (*Mettl14*$^{+/f}$) and *Mettl14*$^{f/f}$ P14 brains after

electroporation of Dcx-CRE-IRES-GFP and pCAG-RFP plasmids at E14.5. The upper panels show representative images of ipsilateral to contralateral axon projections. The lower panels display z-projected images at higher magnification of axonal arborization in the S1 region. (scale bars: upper panels, 1 mm; lower panels, 200 μm). The plot represents the quantitative intensity of RFP in total contralateral branching, projections, and arborization normalized to the RFP^+ soma intensity of upper-layer neurons. A significant reduction was observed in *M14* cKO compared to the control. (n=8 for each, P=0.004932). **(e)** Quantitative analysis of contralateral branching distribution along the radial axis of the cortical wall shows reduced axon projections and arborization (L2/3, L5, and L6) of cortical projection neurons normalized to soma RFP intensity compared to the control at P14. (n=4 for each, confidence level=0.99). **(f-j)** *M14* cKO primary neuron exhibited abnormal neurite growth at DIV6. Shown in **(f)** are representative confocal images and skeletal images (scale bars: 100 μm). The right panels show enlarged area of squared skeletal images (scale bars: 10um). Neurite length and collateral branching frequency were quantified in **(g)** (Control n=50, *M14* cKO n=56; P < 2.2e-16) and **(f)** (Control n= 30, *M14* cKO n=19; P=0.03536). **(i)** Live imaging of growth cones in control and *M14* cKO neurons over 3 hours at DIV6. Red arrowheads indicate the locations of growth cones (scale bar: 20 μm). Shown in **(j)** is the quantification of total growth length divided by tracking time. (Control n=114, *M14* cKO n=134; P=0.02441). **(k)** The quantification of the transient protrusion. (Control n=15, M14 cKO n=19, P=0.01692). Significance was evaluated using two-tailed unpaired Student's t-tests (c, d, g, h, and j). The significance of RFP intensity across the midline was evaluated using two-way ANOVA (b). *P < 0.05, **P < 0.01, ****P < 0.0001.

6) Fig 3e - Fig4h - Fig 5e, g - Fig 6 b,d,f,h : Primary neurites/dendrites are being analyzed instead of axons in these figures. This causes a major problem to the authors' claim on the role of m6A and DF2 in axonal mRNA transport and development. Co-staining with an axonal marker such as Tau is required for identifying the correct subcellular compartment.

We fully agree with the reviewer's point. Although we analyze smFISH/PLA signals on mCherry positive neurite-like structure, it is necessary to distinguish the neurite/axon. To address this concern, we repeated the experiments with co-staining for the axonal marker Tau and re-assessed the quantifications in Tau^+ axons. The revised analyses yielded results consistent with our original conclusions. Accordingly, we have updated the corresponding figures and statistical data in the revised Fig. 3–6 and revised Extended Data Fig. 5-8. In addition, we have corrected the terminology from *neurites* to *axons* throughout the manuscript text, figure legends, and Methods. These new results further strengthen the scope and impact of our study.

(Supporting data for the Fig. 3e-g)

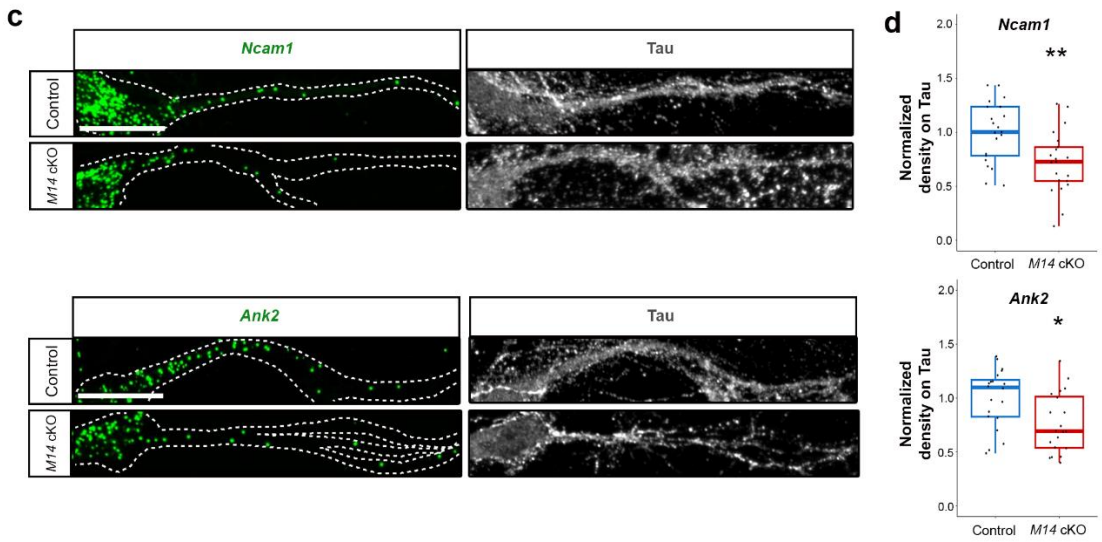

Revised Extended Data Fig. 5. Loss of *Mettl14* leads to a reduced neuronal gene expression and localization in axons. (c-d) *Mettl14* cKO primary cultured neuron showed reduced axonal RNA localization. Shown in (c) are representative smFISH signals (Green) representing endogenous *Ncam1,* and *Ank2* (Scale bars: 20 μm) with axon marker Tau staining. The relative density is quantified in (d) (*Ncam1*: Control n=21, *M14* cKO n=21; *P*=0.002887, *Ank2*: Control n=20, *DF2* cKO n=20; *P*=0.01048). *$P < 0.05$, **$P < 0.01$.

(Supporting data for the Fig. 4i-k)

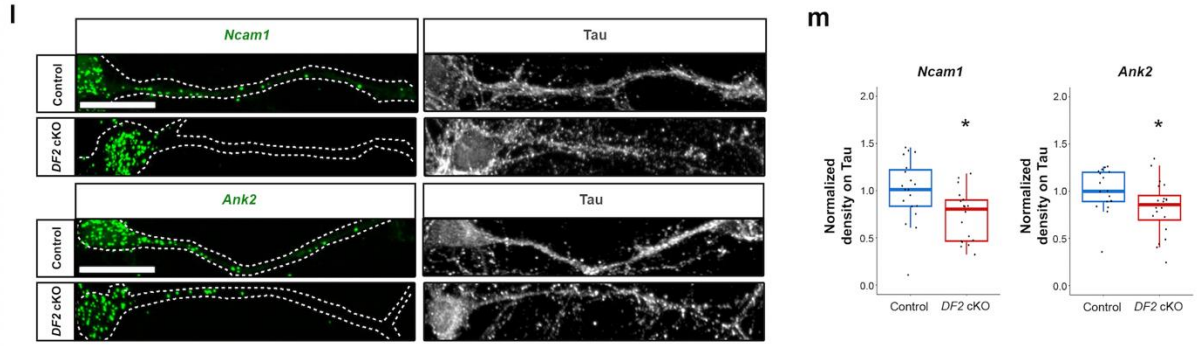

Revised Extended Data Fig. 6. Loss of *Ythdf2* leads to a reduced survival rate, lower body weight, motor impairments, and disrupted neuron projection. (l-m) *DF2* cKO primary cultured neuron showed reduced axonal RNA localization. Shown in (l) are representative smFISH signals (Green) representing endogenous *Ncam1,* and *Ank2* (Scale bars: 20 μm) with axon marker Tau staining. The relative density is quantified in (m) (*Ncam1*: Control n=19, *DF2* cKO n=18; *P*=0.01159, *Ank2*: Control n=18, *DF2* cKO n=20; *P*=0.04176).

(Supporting data for the Fig. 5h-m)

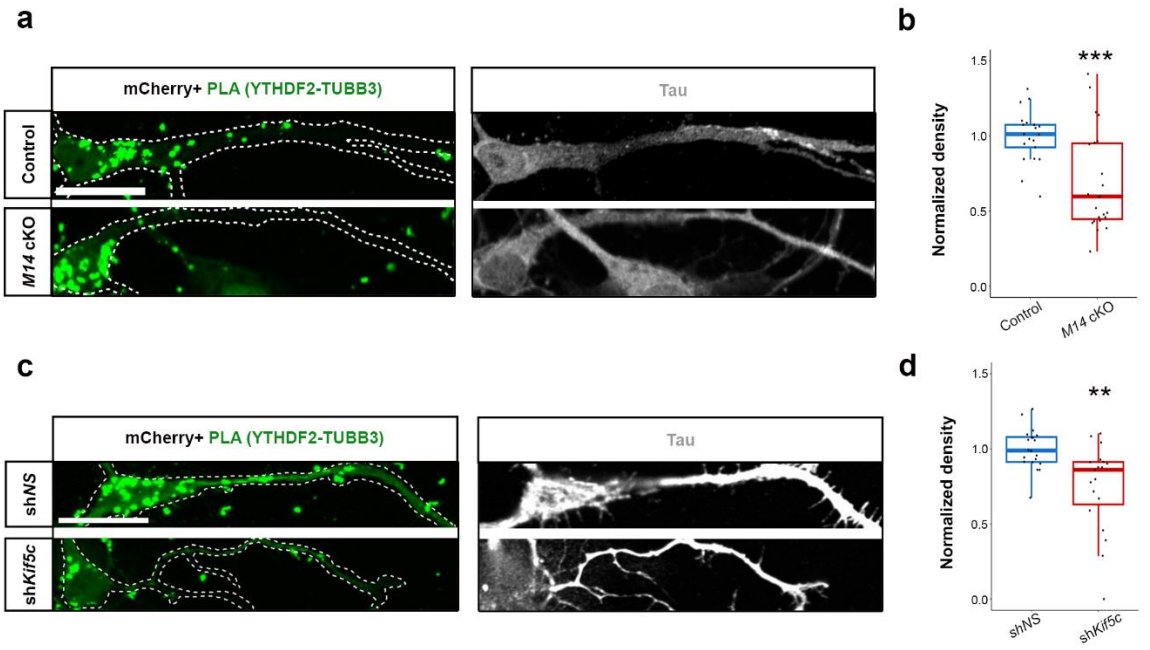

Reviewer Fig. 3. (a-b) YTHDF2 localization to distal neurite decreased in *M14* cKO mouse primary neuron. Shown in (a) are representative PLA signals (Green) representative PLA signals (Green) showing endogenous YTHDF2-TUBB3 association (Scale bars: 20 μm) with axon marker Tau staining. The relative density is quantified in (b) (Control n=20, *M14* cKO n=19, *P*= 0.0003697). **(c-d)** YTHDF2 localization to distal neurites decreased in mouse primary neuron upon *Kif5c* knockdown. Shown in (c) are representative PLA signals (Green) representative PLA signals (Green) showing endogenous YTHDF2-TUBB3 association (Scale bars: 20 μm) with axon marker Tau staining. The relative density is quantified in (d) (Control n=20, sh*Kif5c* n=19, *P*=0.001124).

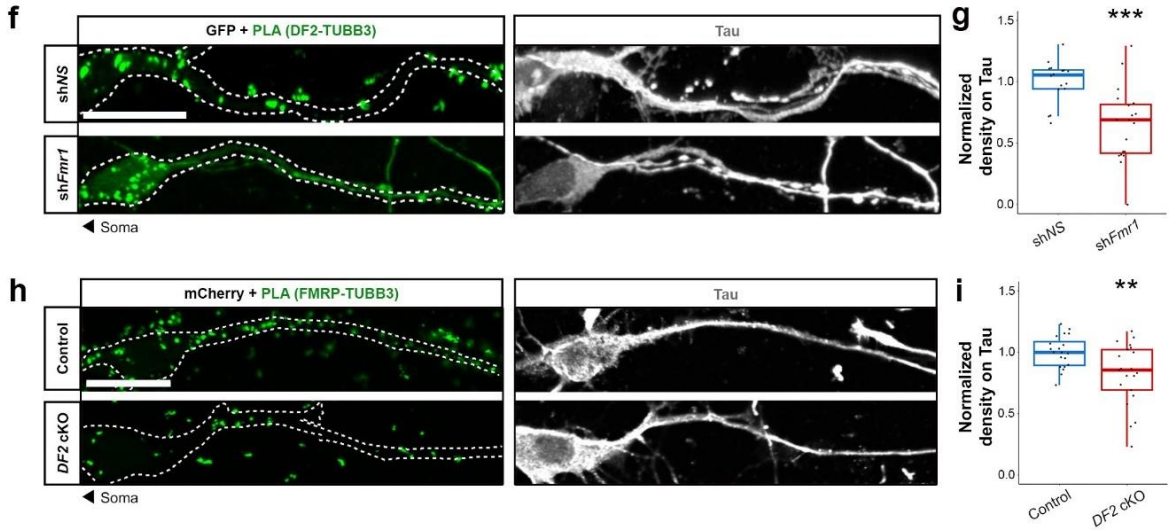

Revised Fig. 6. FMRP interacts with YTHDF2 to facilitate transport of m⁶A-tagged mRNAs to distal neurites in developing neurons. **(f-g)** YTHDF2 localization to neurites decreased in *Fmr1* KD mouse primary neurons. Shown in (f) are representative PLA signals (green) and Tau indicating endogenous YTHDF2-TUBB3 associations in control and *Fmr1* KD mouse primary neurons (Scale bar: 20μm). The relative density on tau is quantified in (g) (Control n=16, *Fmr1* KD n=19, *P*= 0.0002645). **(h-i)** FMRP localization to neurites decreased in *DF2* cKO mouse primary neurons. Shown in (h) are representative PLA signals (green) and Tau indicating endogenous FMRP-TUBB3 associations in control and *DF2* cKO mouse primary neurons (Scale bar: 20μm). The relative density on tau is quantified in (i) (Control n=20, *DF2* cKO n=21, *P*= 0.006918).

Changes in the text:

(Line 663-665)

Finally, Hoechst solution was added for 3 minutes after washing, and mounting media was applied to the slides to fix the coverslips for storage in the dark at 4°C. If required, immunocytochemistry was performed after the smFISH.

(Line 682-684)

After two washes with TBS, mounting media was applied to the slides to fix the coverslips for storage in the dark at 4°C. If required, immunocytochemistry was performed after the PLA.

7) In addition, the distance from the nucleus is not enough in smFISH; instead, the percentages of mRNA puncta in cell soma versus axon and/or number need to be shown and validated that Mettl14 or YTHDF2 KO do not decrease the total number of the mRNAs tested but alter distribution.

We fully agree with the reviewer's point. As suggested, we re-assessed smFISH results using the normalized ratio of total mRNA puncta to on neurite puncta. The revised quantifications were updated in the revised Fig. 3g, Fig. 4k, and Fig. 6j. We described the detailed method to calculate the density and added to the method section, image analysis part.

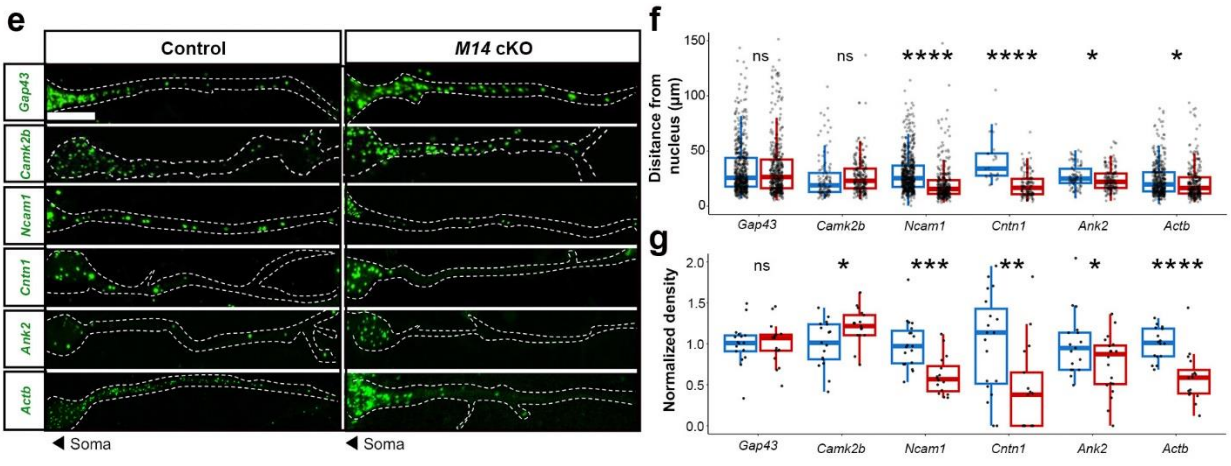

Revised Fig.3 m⁶A modification is crucial for the distal translocation of cytoskeletal mRNAs in differentiating neurons. **(e-g)** *M14* cKO primary cultured neurons show depleted

RNA localization. Shown in (e) are representative smFISH signals (green) representing endogenous *Gap43*, *Camk2b*, *Ncam1*, *Cntn1*, *Ank2*, and *Actb* (scale bars: 20 μm). The distance from the nucleus is quantified in (f) (*Gap43*: Control n=568, *M14* cKO n=460; *P*=0.6987, *Camk2b*: Control n=113, *M14* cKO n=238; *P*=0.6099, *Ncam1*: Control n=609, *M14* cKO n=343; *P* ≤ 2.2e-16, *Cntn1*: Control n=28, *M14* cKO n=137; *P*=1.46e-14, *Ank2*: Control n=90, *M14* cKO n=164; *P*=0.02853, *Actb*: Control n=397, *M14* cKO n=294; *P*=0.01343), and the relative density of smFISH puncta in neurites compared to the total is quantified in (g) (*Gap43*: Control n=17, *M14* cKO n=17; *P*=0.9671, *Camk2b*: Control n=17, *M14* cKO n=17; *P*=0.01711, *Ncam1*: Control n=19, *M14* cKO n=16; *P*=0.0001537, *Cntn1*: Control n=19, *M14* cKO n=17; *P*=0.005298, *Ank2*: Control n=17, *M14* cKO n=20; *P*=0.04917, *Actb*: Control n=16, *M14* cKO n=16; *P*=9.801e-05).

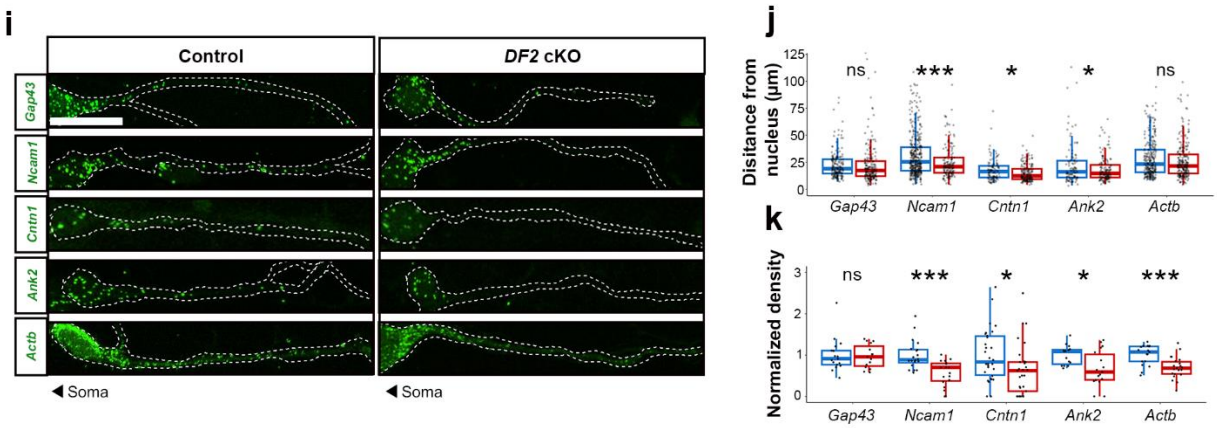

Revised Fig.4 *Ythdf2* deletion reduces axonal projection and neurite length and impairs growth cone dynamics in *DF2* cKO. (i-k) *DF2* cKO primary cultured neuron showed reduced distal RNA localization. Shown in (i) are representative smFISH signals (Green) representing endogenous *Gap43, Ncam1, Cntn1, Ank2, Actb* (Scale bars: 20 μm). The distance from the nucleus was quantified in (j) (*Gap43* Control n=178, *DF2* cKO n=194; *P*=0.8605, *Ncam1*: Control n=383, *DF2* cKO n=157; *P*=0.0007246, *Cntn1*: Control n=106, *DF2* cKO n=165; *P*= 0.01605, *Ank2*: Control n=102, *DF2* cKO n=140; *P*= 0.02627, *Actb*: Control n=264, *DF2* cKO n= 231; *P*=0.1793) and the relative density of smFISH puncta in neurites compared to the total is quantified in (k) (*Gap43*: Control n=15, *DF2* cKO n=17; *P*= 0.8093, *Ncam1*: Control n=19, *DF2* cKO n=20; *P*=0.0002398, *Cntn1*: Control n=29, *DF2* cKO n=30; *P*=0.03339, *Ank2*: Control n=18, *DF2* cKO n=15; *P*=0.01088, *Actb*: Control n=22, *DF2* cKO n=17; *P*=0.0007279).

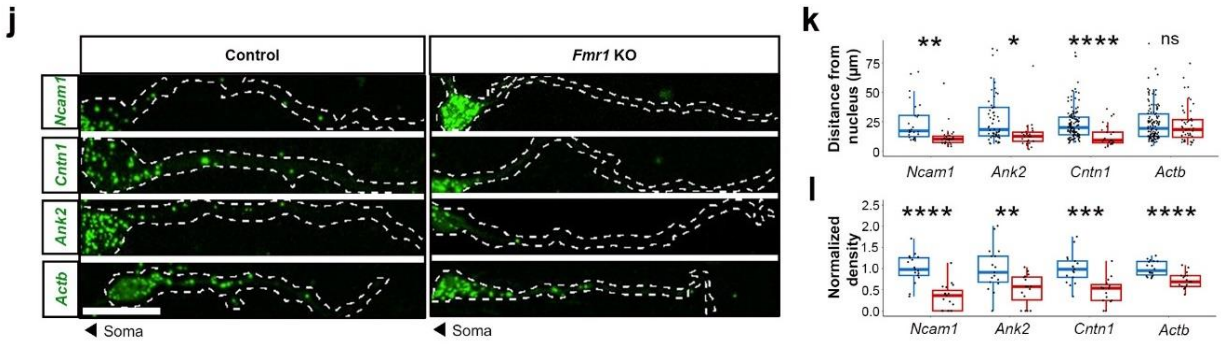

Revised Fig.6 FMRP interacts with YTHDF2 to assist m^{6}A-tagged mRNA transport to distal neurites of developing neurons. **(j-l)** RNA localization to neurites decreased in *Fmr1* KO mouse primary neurons. Shown in (j) are representative smFISH signals (green) representing endogenous *Ncam1*, *Cntn1*, *Ank2*, and *Actb* in control and *Fmr1* KO conditions (Scale bar: 20μm). The distance from the nucleus was quantified in (k) (*Ncam1*: Control n = 26, *Fmr1* KO n = 33; *P* = 0.0005381. *Cntn1*: Control n = 62, *Fmr1* KO n = 27; *P* = 0.04902. *Ank2*: Control n = 125, *Fmr1* KO n = 25; *P* = 0.0005668. *Actb*: Control n = 123, *Fmr1* KO n = 48; *P* = 0.6665) and the relative density of smFISH puncta in neurites compared to the total is quantified in (l) (*Ncam1*: Control n=17, *FMRP* cKO n=19; *P*=, 4.408e-07 *Cntn1*: Control n=17, *FMRP* cKO n=16; *P*=0.003859, *Ank2*: Control n=17, *FMRP* cKO n=15; *P*=0.0001217, *Actb*: Control n=18, *FMRP* cKO n=17; *P*=5.784e-05).

Changes in the text:

(Line 233-237)

We measured the distance from the soma and the relative density of smFISH signals in neurites, and found that *Ncam1*, *Cntn1*, *Ank2,* and *Actb* mRNAs were reduced in distal neurites in *M14* cKO compared to the control at DIV6. However, levels of *Gap43* and *Camk2b* mRNAs remained unchanged (Fig. 3e-g, Extended Data Fig. 5c-d).

(Line 824-828)

Quantification of smFISH single molecules and PLA analysis was conducted with NeuronJ by measuring the distance between a single RNA molecule and the center of the nucleus along axon tracks labeled with fluorescent proteins or Tau. The normalized density of smFISH and PLA was quantified as the ratio of neurite signal to total signal, then normalized to the control ratio.

8) Fig 3a. Although the CC-seq results suggest altered axonal mRNA population in the crossing axons, the same line (Mettl14 nestin-cre cross) has shown deficits in corticogenesis. Therefore it remains unclear whether the alteration is due to axonal transport of the RNA or disturbed corticogenesis. In lines 212-213, does the decrease or increase refer to the abundance of the mRNA or distribution (I noted that in extended Fig 3, layer ⅔ cortex was dissected). Did the author sequence soma-derived mRNAs to normalize expression level?

We thank the reviewer for this insightful comment. As suggested, we performed qPCR analyses for our target mRNAs (*Gap43*, *Ncam1*, *Ank2*, and *Cntn1*) and normalized neurite-derived mRNA levels to soma-derived mRNAs (Reviewer Fig. 4). The results indicate that the

axonal distribution of these transcripts was reduced, rather than a general decrease in overall mRNA abundance.

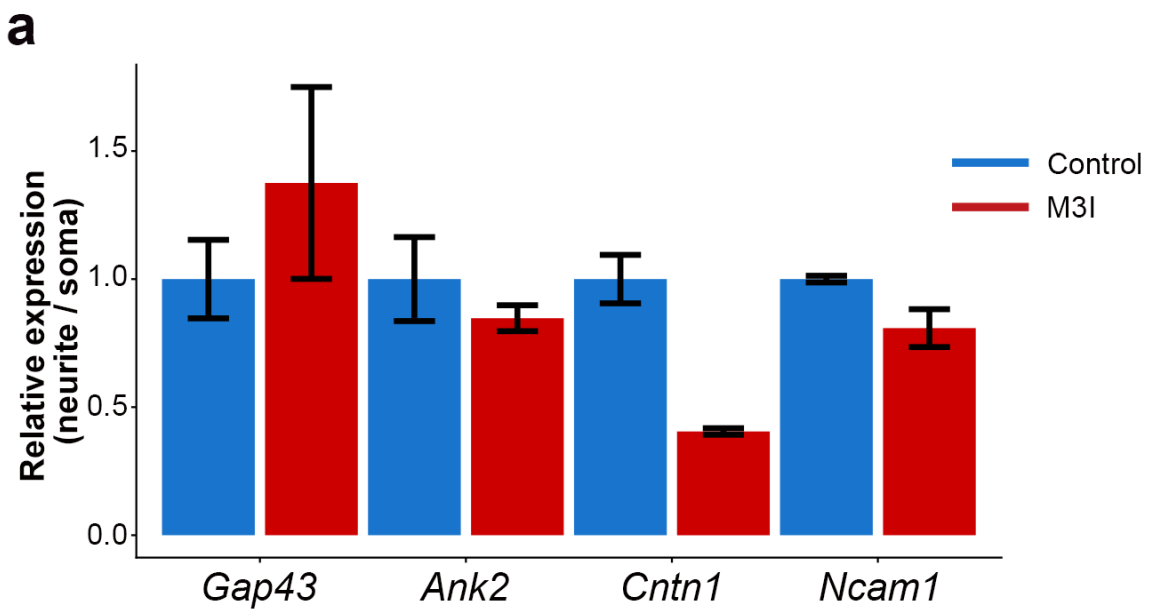

Reviewer Fig. 4. CC-seq validation by qRT-PCR comparing soma and neurite fractions in WT and m⁶A loss-of-function primary neurons.
(a) Bar graphs show the relative expression levels of *Gap43*, *Ank2*, *Cntn1*, and *Ncam1* measured by qRT-PCR in soma and neurite fractions isolated using a transwell system from WT mouse primary neurons and METTL3 inhibitor-treated samples. Three biological replicates were analyzed. Values represent mean ± SEM and were normalized to *GAPDH* expression.

9) Fig 3g: The lysosomal live-cell tracking analysis shows only one and two moving lysosomes in the kymographs. This number seems low. How many spots were detected in a continuous axon on average? In addition, the transport needs to be evaluated by using anterograde and retrograde displacement lengths and speed.

More importantly, lysosome transport is used as a control for mRNA transport but there is no live-cell imaging of any mRNA that the authors claimed to be dependent on m6A. Since mRNA transport is the main focus of the paper, it will be important to include mRNA live-cell imaging in the axonal compartment and compare non-target mRNA to target mRNAs.

9) Fig 3g : The lysosomal live-cell tracking analysis shows only one and two moving lysosomes in the kymographs. This number seems low. How many spots were detected in a continuous axon on average? In addition, the transport needs to be evaluated by using anterograde and retrograde displacement lengths and speed.
More importantly, lysosome transport is used as a control for mRNA transport but there is no live-cell imaging of any mRNA that the authors claimed to be dependent on m6A. Since mRNA transport is the main focus of the paper, it will be important to include mRNA live-cell imaging in the axonal compartment and compare non-target mRNA to target mRNAs.

We agree with the comment of reviewer about lysosomal live imaging, so we replaced them into better representative images that can shows enough numbers of lysosomes on neurites (Extended Figure 5e, Extended Movie 7, 8). The number of lysosome tracks in continuous axons are varied by the length of the neurite, but we found about 10 lysosome tracks are found on axon on average. Also, we newly added the graph which show proportion of anterograde and retrograde movement of the lysosome for better understanding of effect of m^{6}A on lysosome transport (Extended Figure. 5f). With this, we also added the graph for track max speed of lysosomal track on axon that reviewer asked (Extended Figure 5h). Throughout the whole additional analysis, not only speed and total displacement, the direction of total displacement did not change in M14 cKO condition. These data indicating that the general transport machinery was unaffected by m^{6}A depletion.

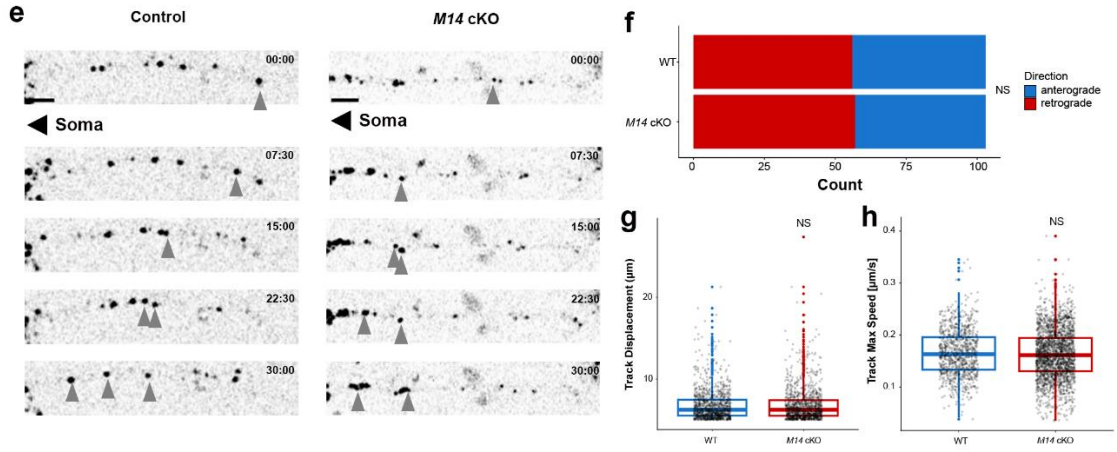

Extended Data Fig. 5. Loss of *Mettl14* leads to a reduced neuronal gene expression and localization in axons.

(**e-h)** Live imaging of lysosomes in *M14* cKO and control cortical neurons at DIV6. Shown in (e) is a time-lapse image representing lysosome dynamics over 30 minutes (scale bars: 10 µm). Direction of lysosome movement is counted in two categories, anterograde and retrograde, and validated in (f) (Control n=103, *M14* cKO n=103, *P*=0.1573). Lysosome track displacement length is quantified in (g) (Control n=1130, *M14* cKO n=1195, *P*=0.5133), and lysosome track max speed is quantified in (h) (Control n=1130, *M14* cKO n=1195, *P*=0.1509). Significance was evaluated using two-tailed unpaired Student's t-tests (b, d, g, h), and Pearson's Chi-squared test (f). ns, not significant; **P* < 0.05, ***P* < 0.01.

We thank the reviewer for this valuable suggestion, which was also raised by Reviewer #2. To address this, we performed live-cell mRNA imaging using the MS2 reporter system. Specifically, we used a BFP-Actb-3′UTR-MS2x24 reporter construct that retains the endogenous 3′UTR m^{6}A motif (the 1217th position, 5nt after the STOP codon) identified by m^{6}A-SAC-seq. The reporter was co-transfected into primary neurons together with MCP-GFP-HA, which binds to the reporter RNA and enables visualization via GFP fluorescence (Revised Fig. 3h). As a result, we detected RNA reporter signals in neurites of DIV6 primary neurons under both control and *Mettl14* cKO conditions. Notably, anterograde transport of RNA granules was markedly reduced in *Mettl14* cKO neurons (Revised Fig. 3i-j, Extended Movie 3, 4). Moreover, the total motile time of mRNA reporter drastically decreased in *Mettl14* cKO conditions. (Revised Fig. 3k)

It is well established that neurons are polarized cells with axonal microtubules oriented in a plus-end–out configuration [9]. Consistent with this, our LC–MS/MS data revealed that YTHDF2 interacts with kinesins, including KIF5C, in an m⁶A-dependent manner (Revised Fig. 5b-d). Moreover, we demonstrated direct interactions between YTHDF2, TUBB3, and KIF5C using PLA and co-immunoprecipitation assays (Revised Fig. 5e-o). Together, these findings suggest that m⁶A-modified RNAs are transported to distal axons via anterograde movement mediated by the YTHDF2–kinesin complex.

Next, to examine the direct impact of m⁶A tagging on RNA localization, we generated a point-mutant reporter (BFP-Actb-3′UTRΔm⁶A-MS2x24) lacking the single m⁶A site. The mutant reporter showed reduced anterograde transport of RNA granules and decreased total motile time compared with the wild-type construct (Revised Fig. 3l-n, Extended Movie 5, 6). These new results strongly support our original conclusion and further expand the mechanistic scope and impact of our study.

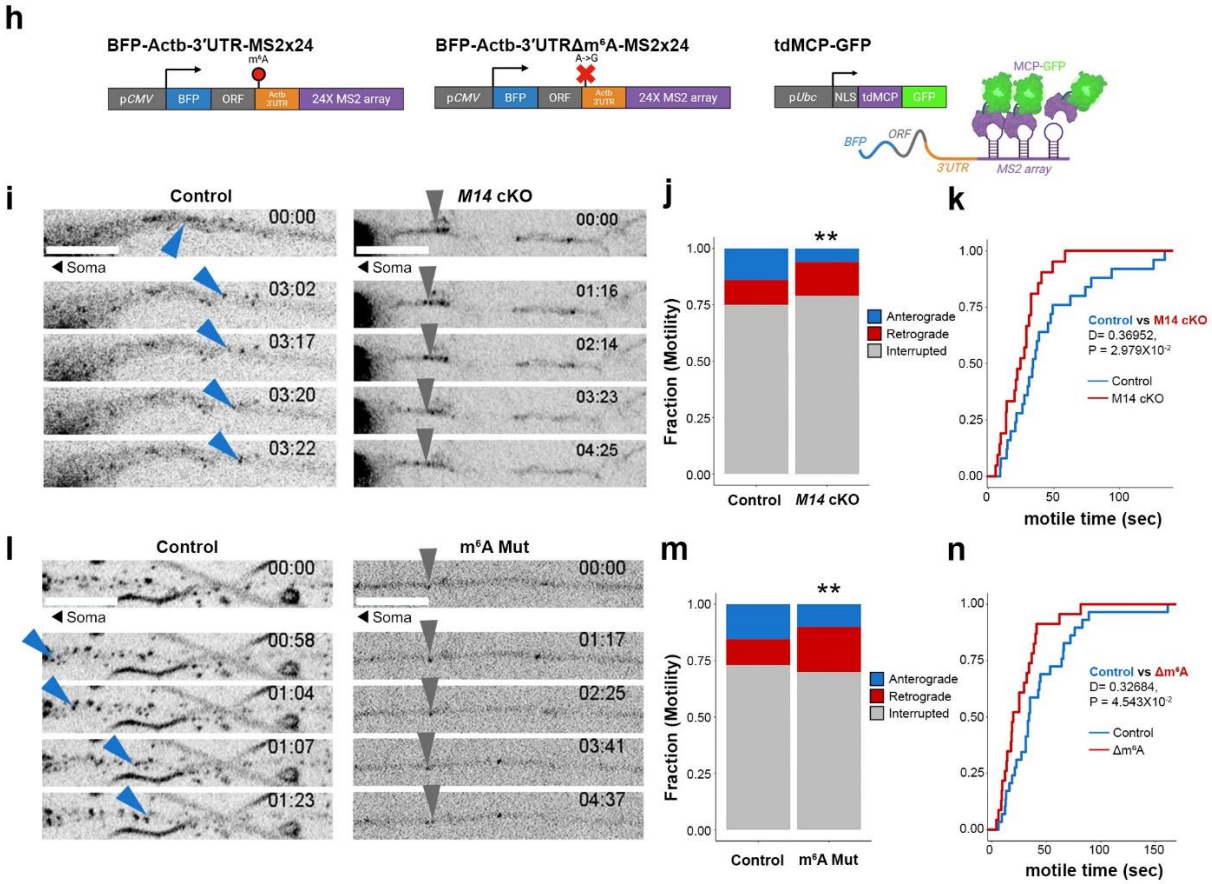

Revised Fig. 3. m⁶A modification is crucial for the distal translocation of cytoskeletal mRNAs in differentiating neurons.

(h) The schematic diagram of RNA live imaging MS2 system. **(i-k)** *M14* cKO primary cultured neurons show depleted anterograde RNA localization. Shown in (i) anterograde (blue arrowheads) and interrupted (grey arrowheads) RNA granules are indicated (scale bars: 10 μm). The RNA reporter dynamics were quantified in (j) (Control n=173, *M14* cKO n=181, *P*=0.007019). The motile time of RNA reporter were compared with each condition in (k) (Control n=25, *M14* cKO n=21) **(l-n)** The m⁶A point mutated reporter show depleted

anterograde RNA localization. Shown in (l) anterograde (blue arrowheads) and interrupted (grey arrowheads) RNA reporter are indicated (scale bars: 10 μm). The RNA reporter dynamics were quantified in (j) (Control n=148, Δm⁶A n=130, *P*=0.007464). The total motile time of RNA granules was compared with each condition in (k) (Control n=29, *M14* cKO n=23)

Significance was evaluated using two-tailed unpaired Student's t-tests (f, and g). The distribution difference of RNA motility between two groups was evaluated using the chi-square test (j, and k). The significance of two RNA motility time sets was evaluated using the Kolmogorov-Smirnov test (k, n). ns, not significant, $*P < 0.05$, $**P < 0.01$, $***P<0.001$, $****P < 0.0001$.

Changes in the text:

(Line 240-253)

To directly visualize RNA transport through neurites, we employed the MS2 system[10]. We used HA-tdMCP-GFP and BFP–actin–3′UTR–24×MS2 reporters containing a conserved m⁶A site in the 3′UTR (at the 1217th position, located xx nt downstream of the stop codon) (Fig. 3h). RNA dynamics were monitored in control and *Mettl14* cKO neurons using a spinning-disk microscope. Interestingly, anterograde RNA movement was significantly reduced under *M14* cKO conditions (Fig. 3i-j, Extended Movie 3,4). Moreover, the total motile time of RNA was also reduced under *M14* cKO conditions (Fig. 3k). To examine the direct role of m⁶A modification in RNA transport, we generated a mutant reporter, BFP–actin–3′UTRΔm⁶A–24×MS2, by introducing an A→G substitution at position 1217 to prevent m⁶A modification. RNA granule movement was then compared between the wild-type and Δm⁶A reporters in mouse primary neurons. As a result, anterograde RNA movement was markedly reduced in the Δm⁶A reporter (Fig. 3l-n, Extended Movie 5,6). These findings demonstrate that a single m⁶A modification within the 3′UTR is critical for efficient anterograde transport of *Actb* mRNAs in developing neurons.

(Line 523-528)

For the RNA live imaging, we used phage-ubc-nls-ha-tdMCP-gfp (Addgene #30649), and pcDNA-puro-TagBFP-β-ACTIN-3′UTR-24xMS2 (Addgene #205161). For the point-mutant reporter (BFP-Actb-3′UTRΔm⁶A-MS2x24) we used Site-directed Mutagenesis kit (Enzynomics, EZ004S) according to the manufacturer's instructions. In brief, reporter plasmid was amplified with a pair of primers substituting the conserved m6A site with a cytosine residue. Next, PCR product ligated and transformed in to E. coli for the selection and amplification.

(Line 609-615)

For the RNA live imaging, we co-electroporated phage-ubc-nls-ha-tdMCP-gfp, with pcDNA-puro-TagBFP-β-ACTIN-3′UTR-24xMS2 reporters which retains the endogenous 3′UTR m⁶A motif (the 1217th position, 5nt after the STOP codon) to cortical neurons on a confocal glass-bottom dish and culture to the DIV5~6. Live images were acquired with a Nikon Eclipse Ti inverted microscope equipped with a CSU-10 spinning disk (Yokogawa, Tokyo, Japan), an EMCCD camera, and a 100× oil immersion objective (NA 1.49) for 5minutes with 500ms intervals.

(Line 829-833)
For RNA live images, RNA molecules observed > 60 frames were selected for the consistency. Anterograde and retrograde movement were counted to calculate the fraction of transport and motile time. Movements longer than 2 μm were categorized to antero or retro group and less than 2 μm were categorized as interrupted group[11].

10) Fig 3. The rationale for narrowing down to YTHDF2 for further studies provided in the text (lines 254-263) is not sufficient for excluding YTHDF1 or YTHDF3. Previously reported YTHDF2 null mice (using ubiquitous expressed Cre) showed severe deficits in proliferation and differentiation of neural progenitor cells thus does not provide evidence of exclusive association of YTHDF2 to mRNA axonal transport (https://doi.org/10.1186/s13059-018-1436-y). The same paper has suggested the JAK-STAT cascade inhibitory genes contribute to neurite outgrowth. The behavior of this pathway in the YTHDF2 nestin-Cre and link to the axon deficits in YTHDF2 cKO need to be discussed. Furthermore, the statement in line 259-260 “Ythdf1 or Ythdf3 knockout mice did not exhibit obvious developmental abnormalities” was not consistent with the cited paper, which concluded “YTHDF1 and YTHDF2 have redundant functions in m6A regulation of cortical neurogenesis” (https://doi.org/10.1016/j.isci.2022.104908). A bioRxiv paper demonstrated the role of YTHDF1 in axon development through regulating translation of APC protein (https://www.biorxiv.org/content/10.1101/2020.11.14.382556v3). Given that multiple lines of evidence suggesting molecular interactions and functional redundancy of YTHDF1/2/3 have been reported in multiple cell contexts, the authors need to explore/confirm the involvement of YTHDF1 and YTHDF3 instead of drawing specific connections to YTHDF2 without further investigation.

Thank you for raising an important issue. As shown in Extended Data Fig. 6a, YTHDF2 is the most highly expressed member of the YTHDF family during early brain development, based on single-cell sequencing data. We also performed live imaging of growth cones following sh*YTHDF1* or sh*YTHDF3* knockdown. However, these neurons exhibited no significant changes in the velocity of growth cone advancement compared with *M14* cKO or *DF2* cKO neurons, suggesting that YTHDF2 is the primary m^{6}A reader required for regulating growth cone dynamics in early neuronal differentiation. We have added these new data in the text and the revised Extended Data Fig. 6b-e.

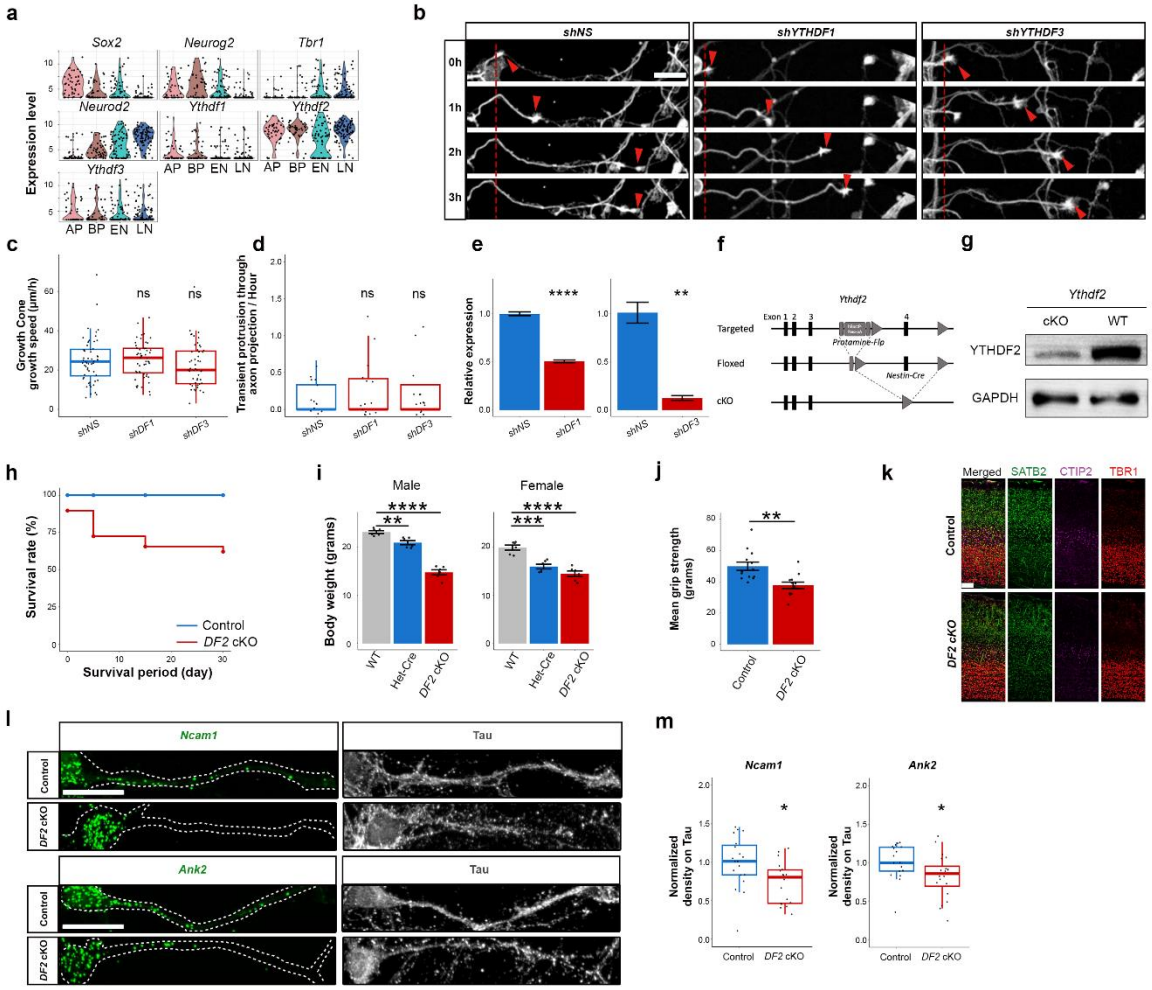

Revised Extended Data Fig. 6. Loss of *Ythdf2* leads to a reduced survival rate, lower body weight, motor impairments, and disrupted neuron projection (a) Expression of neuronal marker genes and m^{6}A reader proteins based on a published scRNA-seq dataset during mouse corticogenesis. (AP: apical progenitors; BP: basal progenitors; EN: early neurons; LN: late neurons). **(b-d)** Neurite projections within 3 hours were tracked under a confocal microscope at DIV6 (b) (scale bars: 20 μm). Shown in **(c)** is the quantification of total growth length divided by tracking time (sh*NS* n=56, sh*DF1* n=53, sh*DF3* n=51, sh*NS-DF1 P*= 0.6807, sh*NS-DF1 P*= 0.2417), and **(d)** is the quantification of the transient protrusion (sh*NS* n=14, sh*DF1* n=16, sh*DF3* n=15, sh*NS-DF1 P*= 0.4713, sh*NS-DF1 P*= 0.1851). **(e)** Validation of *DF1, DF3* KD in N2A by qPCR. Values represent mean ± SEM after being normalized by GAPDH expression. **(f)** Genetic deletion strategy of *Ythdf2* of *Nestin*-Cre; *Ythdf2*$^{f/f}$ cKO mice. **(g)** Validation of *DF2* cKO in the mouse cortex through western blotting. **(h)** Survival curve of *Ythdf2* Het (n = 33) and cKO (n = 29) pups. **(i)** Body weight of WT and *DF2* cKO pups at P14 (n = 6 for each, WT-het CRE *P* = 0.001598, WT-cKO *P* = 8.14e-08) and female mice (n = 6 for each, WT-het CRE *P* = 0.0002651, WT-cKO *P* = 3.97e-05). **(j)** Grip strength test of control and *DF2* cKO pups at P14 (Control: n = 13, cKO: n = 12, *P* = 0.001556). **(k)** Confocal images of SATB2 (layer 2/3), CTIP2 (layer 5), and TBR1 (layer 6) in coronal sections (Scale bar: 50μm). There is no significant difference after comparison between *DF2* cKO and control. **(l-m)** *DF2* cKO primary cultured neuron showed reduced axonal RNA localization. Shown in (l) are representative smFISH signals (Green) representing

endogenous *Ncam1,* and *Ank2* (Scale bars: 20 μm) with axon marker Tau staining. The relative density is quantified in (m) (*Ncam1*: Control n=19, *DF2* cKO n=18; *P*=0.01159, *Ank2*: Control n=18, *DF2* cKO n=20; *P*=0.04176). Significance was evaluated using two-tailed unpaired Student's t-tests (c, d, e, i, j, and m). ns, not significant; $^{**}P < 0.01$, $^{***}P < 0.001$, $^{****}P < 0.0001$.

Changes in the text:
(Line 275-278)
In contrast, *Ythdf2* null knockout mice exhibited embryonic lethality and impaired cortical development [12]. Furthermore, *YTHDF1* and *YTHDF3* knockdown did not alter the dynamics of growth cones and protrusion formation in cultured primary cortical neurons (Extended Data Fig. 6b-e).

11) Fig 4. The nestin-cre mice are used for generating both Mettl14 cKO and YTHDF2 cKO. It will be helpful to conduct CC-seq in the YTHDF2 cKO mice and compare results to Mettl14 cKO. The results can further be used to clarify the observations in lines 298-299 "the stability of Ncam1, Cntn1, and Ank2 mRNAs increased in M14 cKO condition, while their stability decreased in the DF2 cKO condition" and further clarify the potential functional redundancy between the three cytoplasmic readers YTHDF1, 2, and 3.

We appreciate the reviewer's suggestion. To address this, we performed CC-seq in *Ythdf2* cKO mice. The Ythdf2 CC-seq data revealed a transcriptional profile comparable to that observed in the Mettl14 cKO CC-seq (Reviewer Fig. 1a). We identified 565 m^{6}A-modified genes enriched among the downregulated genes, while 237 m^{6}A-modified genes enriched among the upregulated genes. This data indicating that YTHDF2 depletion reduces the localization of m^{6}A-modified mRNAs to distal axons.

Furthermore, GO and GSEA analyses showed that downregulated genes were significantly associated with synapse organization and axonogenesis, whereas upregulated genes were linked to housekeeping processes such as cell division and chromosome organization (Reviewer Fig. 1b-d). These results confirm our original conclusion that YTHDF2 acts as the key m^{6}A reader responsible for transporting m^{6}A-tagged transcripts to axons.

We respectfully request that we intend to use the CC-seq dataset from *Ythdf2* cKO mice in a separate ongoing study. Therefore, we prepared this figure exclusively for reviewer evaluation to address the current question, but have not included it in the revised manuscript.

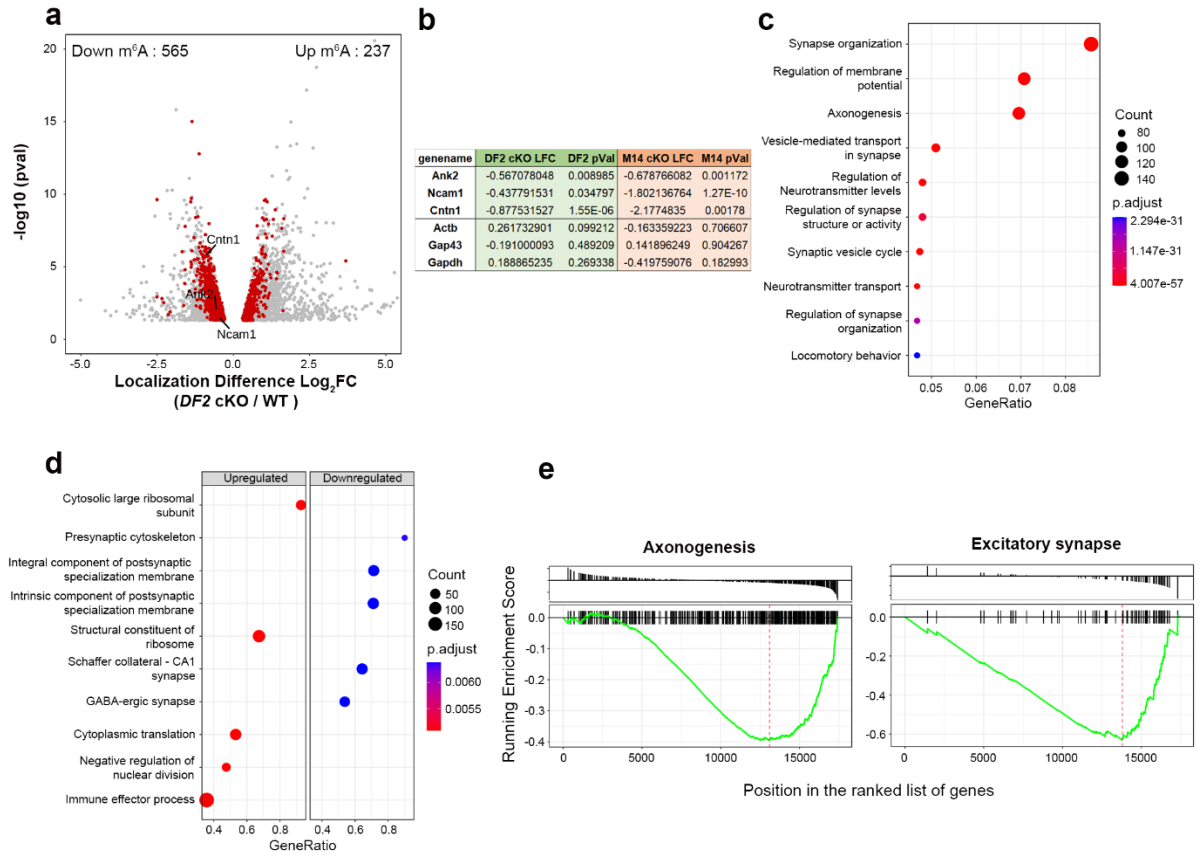

Reviewer Fig. 1. The *DF2* cKO CC-seq data revealed a transcriptional profile comparable to that observed in the *M14* cKO CC-seq

(a) The volcano plot shows genes that are depleted and enriched in the corpus callosum of P4 *DF2* cKO mice. Red indicates m^{6}A-modified genes and targets of interest are highlighted. **(b)** The table summary of *DF2* cKO CCseq and *Mettl14* cKO CCseq result of the target RNAs. **(c)** Gene Ontology analysis of downregulated DEGs. **(d-e)** Gene Set Enrichment Analysis (GSEA) for the position in the DEG fraction ranked genes. The summary dot plot for the position in the DEG ranked genes were represent on (d) and specific term were represented on (e).

12) What is the role of YTHDF2 in axonal expression of L1CAM and NTNG1 proteins shown in Extended Data Fig 4h? Better representative images in extended figure 4h are needed. The yellow intensity in the opposite brain hemisphere shows increase in the DF2 cKO mice contrary to the other side.

We originally intended to illustrate the reduction of axonal tracts extending to distal brain regions in the YTHDF2 cKO brain. However, we believe that the IUE experiments (Fig. 4a–b) already sufficiently demonstrate the disrupted axonal projection to the contralateral hemisphere. To avoid potential confusion, we have decided to remove the L1CAM and NTNG1 immunostaining data (previously shown in Extended Data Fig. 4h) from the revised manuscript.

13) Fig 5. To strengthen the association between DF2 and microtubule through the motor proteins thus its function in transport, PLA DF2/KIF5c is more informative than PLA DF2/Tubb3 to demonstrate the interaction with the MT transport machinery. Better representative image is needed in Fig 5g since most of the green dots in the image are outside of the neurites. The analysis needs to be done in axons instead of dendrites/neurites. “Distance from the nucleus” alone is not sufficient for quantification or conclusion on axonal distribution. “Density” needs to be added.

We appreciate the reviewer’s suggestion, which was also raised by Reviewer #2. To address this, we performed a PLA assay between YTHDF2 and KIF5C to directly demonstrate the interaction between YTHDF2 and the microtubule transport machinery (Revised Fig. 5n-o). We electroporated YTHDF-GFP plasmid in mouse primary neuron, and performed PLA in control and *M14* cKO conditions. As result, YTHDF2-KIF5C interaction on the neurite reduced in *M14* cKO conditions. This results supports our model, YTHDF2-KIF5C-FMRP complex localize m^6A modified RNA to the distal neurites.

As mentioned above, we also quantified the density of PLA signals within Tau^+ axons. The residual PLA signals observed outside neurites likely originated from AAV-noninfected or non-electroporated neurons, which retain endogenous YTHDF2 and TUBB3 expression. To minimize potential misinterpretation, we have replaced the representative images as suggested by the reviewer (Revised Fig. 5k) As suggested, we re-assessed PLA results by the normalized ratio of the total PLA signal versus on neurites to measure “Density” of the PLA results.

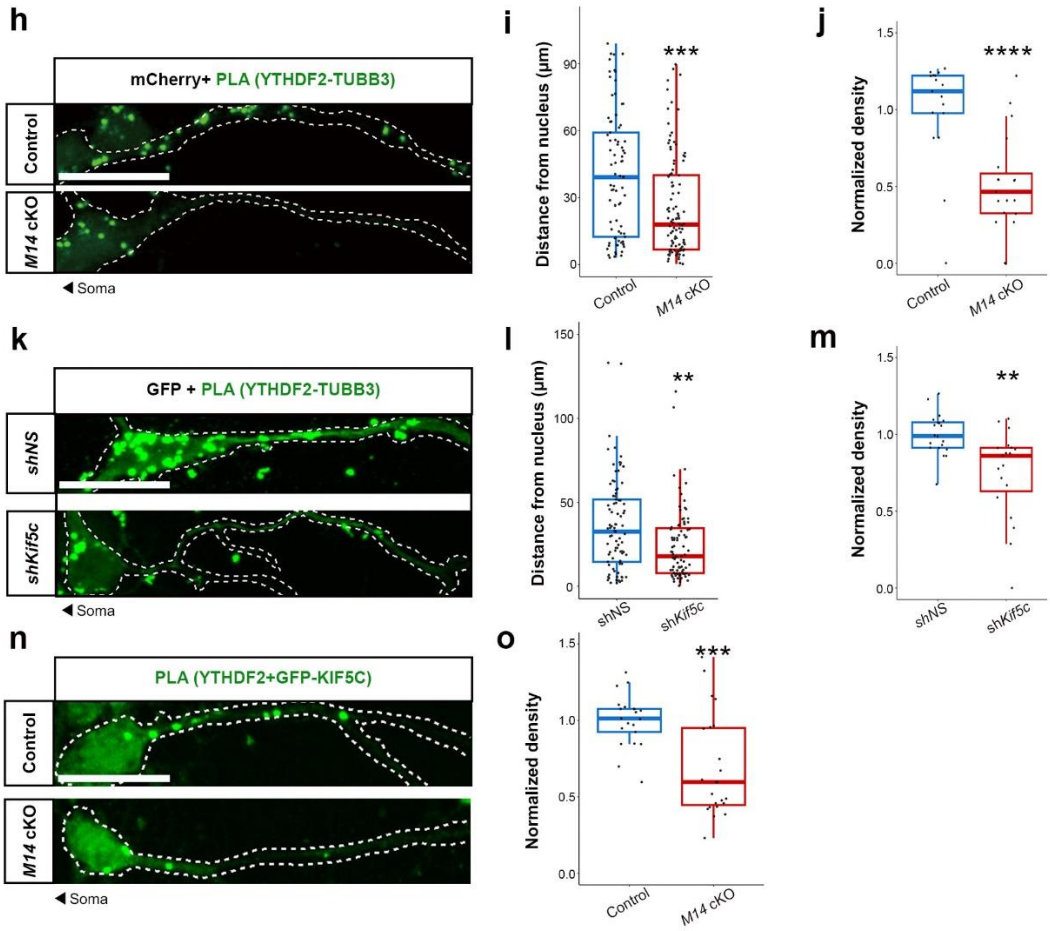

Revised Fig. 5. YTHDF2 interacts with the transport machinery and neurite microtubules in an m^{6}A-dependent manner. **(h-j)** YTHDF2 localization to distal neurite decreased in *M14* cKO mouse primary neuron. Shown in (h) are representative PLA signals (Green) showing endogenous YTHDF2-TUBB3 association (Scale bar: 20μm). The distance from the nucleus was quantified in (i) (Control n=81, *M14* cKO n=108, *P*=0.0001524) and the relative density is quantified in (j) (Control n=17, *M14* cKO n=19, *P*=8.88e-05). **(k-m)** YTHDF2 localization to distal neurites decreased in mouse primary neuron upon *Kif5c* knockdown. Shown in (k) are representative PLA signals (green) indicating endogenous YTHDF2-TUBB3 association in control and *Kif5c* knockdown conditions (scale bar: 20μm). The distance from the nucleus was quantified in (l) (Control n=89, *shKif5c* n=91, *P*=0.001227) and the relative density is quantified in (m) (Control n=20, *shKif5c* n=19, *P*=0.001124).
(n-o) YTHDF2-KIF5C complex localization to distal neurites decreased in *M14* cKO mouse primary neuron. Shown in (n) are representative PLA signals (Green) showing YTHDF2+GFP-KIF5C association (Scale bar: 20μm). The relative density is quantified in (o) (Control n=21, *M14* cKO n=23, *P*=0.0003697). Significance was evaluated using two-tailed unpaired Student's t-tests (i, j, l, m, and o). ns, not significant, $^{**}P < 0.01$, $^{***}P<0.001$, $^{****}P<0.0001$

Changes in the text:

(Line 367-370)

Lastly, we also performed YTHDF2-KIF5C PLA in WT and *M14* cKO neurons, observed reduced interactions between YTHDF2 and KIF5C in axons (Fig. 5i-j). These results suggest that the neuron-specific motor protein KIF5C connects YTHDF2 with microtubules to promote mRNA transport in a m^{6}A-dependent manner.

14) Line 320-325. The m6A-dependent interaction between YTHDF2 and microtubule-related proteins suggest that their association is through the modified mRNAs. Thus the data do not prove a more active role of YTHDF2 than piggybacking the mRNAs being transported. Live-cell imaging of mRNA in YTHDF2 cKO cells is critical.

As described above, we performed live-cell mRNA imaging using the Actb 3′UTR–MS2 reporter system in WT and *Ythdf2* cKO neurons. The anterograde transport of RNA granules was markedly reduced in Ythdf2 cKO neurons compared with WT controls (Revised Fig. 4l, m, Extended Movie 11, 12). Moreover, the total motile time of mRNA reporter granules drastically decreased in *Mettl14* cKO conditions. (Revised Fig. 4n) These results directly demonstrate the active role of YTHDF2 in the transport of *Actb* mRNA and further strengthen our overall conclusion.

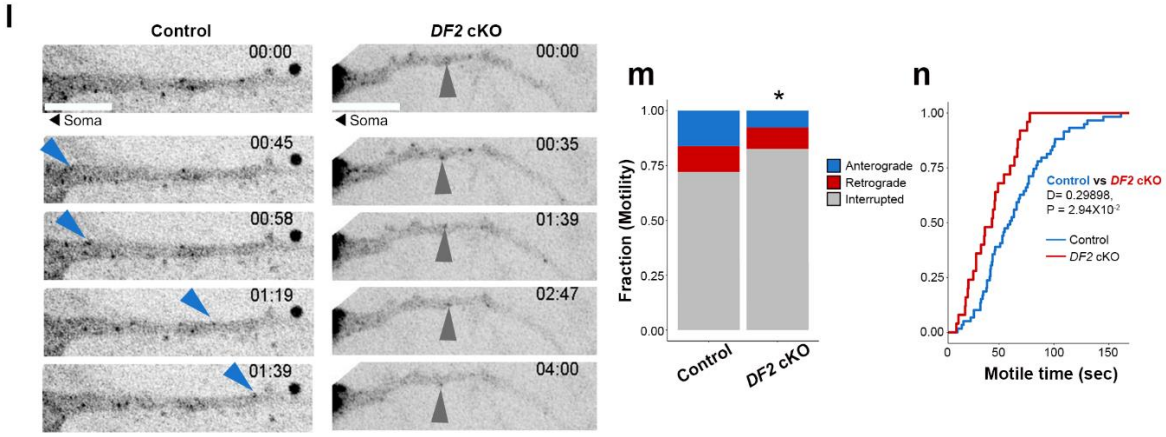

Revised Fig. 4. *Ythdf2* deletion reduces axonal projection and neurite length and impairs growth cone dynamics in *DF2* cKO. (l-n) *DF2* cKO primary cultured neurons show depleted anterograde RNA localization. Shown in (l) anterograde (blue arrowheads) and interrupted (grey arrowheads) RNA reporter are indicated (scale bars: 10 μm). The RNA reporter dynamics were quantified in (m) (Control n=211, *DF2* cKO n=143, *P*=0.04263). The total motile time of RNA reporter were compared with each condition in (n) (Control n=59, *DF2* cKO n=25). The significance was evaluated using two-tailed unpaired Student's t-tests (c, e, f, g, j and k). The significance of RFP intensity across the midline was evaluated using two-way ANOVA (b). The significance of two gene sets and total RNA motility time sets was evaluated using the Kolmogorov-Smirnov test (g and n). The distribution difference of RNA motility between two groups was evaluated using the chi-square test (m) ns, not significant, **P* < 0.05, ***P* < 0.01, ****P*<0.001, *****P* < 0.0001.

Changes in the text:

(Line 323-329)

Next, we used HA-tdMCP-GFP and BFP–actin–3′UTR–24×MS2 reporters described above to visualize the RNA transport (Fig. 3h). The dynamics of reporter RNA granules were monitored in control and *DF2* cKO neurons using a spinning-disk microscope. As result, anterograde RNA movement was significantly reduced under *DF2* cKO conditions (Fig. 4l-n, Extended Movie 11,12). Moreover, the total motile time of RNA granules was also reduced under *DF2* cKO conditions (Fig. 4n), consistent with previous results in the m6A depletion condition and the m^{6}A mutant reporter (Fig. 3k, n).

(Line 330-334)

Collectively, the YTHDF2 cKO model shows significant neurodevelopmental defects at the *in vivo* and *in vitro* levels. m^{6}A-modified mRNAs show decreased stability in the absence of YTHDF2, and YTHDF2 promotes the anterograde localization of its target mRNAs to the distal neurite. Therefore, YTHDF2 is a key reader protein that selectively protects m^{6}A-modified transcripts and localizes them to distal neurites.

15) Fig 6. PLA FMRP/Tubb3 or YTHDF2/Tubb3 offers less specificity of microtubule association and RNA transport than PLA Kif5c. Additional live-cell imaging to monitor co-movement DF2/Kif5c and FMRP/Kif5c will better support the conclusions that YTHDF2 cooperates with FMRP to transport mRNAs into axons through Kif5c along the microtubule. The role of FMRP in YTHDF2/Tubb3 association or axonal mRNA transport is unclear.

We appreciate the reviewer's suggestion. In our trials, direct live imaging of YTHDF2 and KIF5C in primary neurons proved technically challenging. Instead, we performed PLA experiments between YTHDF2 and KIF5C following FMRP knockdown. We observed a reduction in YTHDF2–KIF5C interactions under FMRP knockdown conditions, suggesting that FMRP facilitates the association of YTHDF2 with motor proteins in axons. These new results have been added to the text and incorporated into the (Revised Fig. 6m–n).

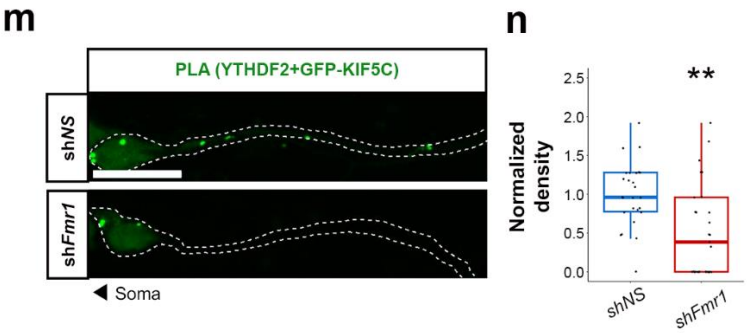

Revised Fig. 6. FMRP interacts with YTHDF2 to assist m^{6}A-tagged mRNA transport to distal neurites of developing neurons. (m-n) YTHDF2-KIF5C complex localization to distal neurites decreased in *Fmr1* KD mouse primary neuron. Shown in (m) are representative PLA signals (Green) showing YTHDF2+GFP-KIF5C association (Scale bar: 20μm). The relative density is quantified in (n) (Control n=26, *Fmr1* KD n=29, *P*=0.001066). Significance was evaluated using two-tailed unpaired Student's t-tests (n). $^{**}P < 0.01$.

Changes in the text:
(Line 404-408)
In addition, the YTHDF2–KIF5C PLA signal was reduced in *shFmr1*-treated neurons, indicating that FMRP facilitates the association of YTHDF2 with motor proteins in axons (Fig. 6m–n). Collectively, these findings suggest a cooperative interaction between YTHDF2 and FMRP that links m^{6}A-tagged mRNAs to microtubules and motor proteins within neurites.

16) Is FMRP responsible for axonal mRNA transport as an independent reader protein?

We appreciate this reviewer's concern. Previous researches suggest the role of FMRP as an independent m^{6}A reader protein that regulates RNA decay and nucleus export [13,14]. To address this, we compare our mouse brain m^{6}A-SAC-seq identified 10304 m^{6}A sites with the mouse brain FMRP CLIP-seq database[15] (Reviewer fig. 5). We compare 262 m^{6}A sites in Q2 transcripts, the group we focus on in this study, and 403 FMRP binding peaks. As a result, only a single m^{6}A site on the CDS of *Txnip* was overlapped with FMRP peaks. Although FMRP might regulate the RNA lifecycle through different mechanisms, we conclude that FMRP does not regulate mRNA transport as an independent m^{6}A reader protein in our context.

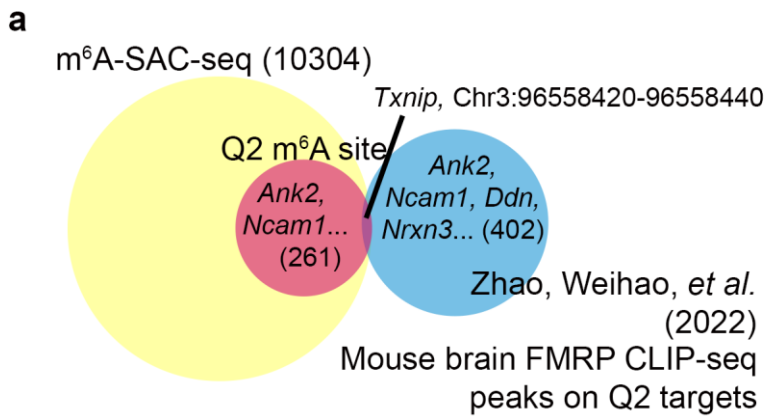

Reviewer Fig. 5. FMRP binding sites do not overlap with the m^{6}A site
(a) Venn diagram comparing the m^{6}A-SAC-seq site and FMRP CLIP-seq peaks.

Minor concerns:
17) Line 53. It is unclear what "context" refers to in "context-guiding interactor". Please be more explicit.

We apologize that the previous text was not sufficiently clear. Following the reviewer's suggestion, we have revised the sentence as follows:

Changes in the text:

(Line 46-48) Notably, we found that FMRP serves as a context-guiding interactor that reshapes the YTHDF2 complex by recruiting specific cofactors and motor proteins, thereby promoting transport rather than degradation of m⁶A-tagged transcripts.

18) Line 106. The sentence suggests interaction between YTHDF2 to m6A sites in the 3'UTR. Is the evidence shown in this paper or previous reports?

We appreciate this reviewer's suggestion. To examine this, we tested the *Actb* 3′UTR reporter, which normally contains a single 3'UTR m⁶A site identified by m⁶A-SAC-seq (Fig. 2), for RNA live imaging. Upon depletion of m⁶A in *Mettl14* cKO neurons, the anterograde movement of *Actb* RNA granules was markedly reduced (Revised Fig. 3i–k; Extended Movie 3, 4). In addition, we tested a mutant reporter construct in which the single m⁶A site was disrupted, and this also showed reduced anterograde movement of RNA granules (Revised Fig. 3l–n; Extended Movie 5, 6). Finally, we performed the same RNA live imaging in *Ythdf2* cKO neurons and observed similar results (Revised Fig. 4l–n; Extended Movie 11, 12). Together, these findings support the conclusion that YTHDF2 promotes anterograde RNA granule transport through m⁶A tagging in the 3′UTR of target transcripts.

19) Line 170. Replace "high" with "higher".

Thanks for catching the error. We have made the correction:

Changes in the text:

(Line 164-165) Interestingly, the average m⁶A stoichiometry in 3'UTR is higher than in the CDS and the 5'UTR (Fig. 2d). This higher methylation stoichiometry in 3'UTR

20) Please check the figure citations in the text. Misplaced citations were found. Where is Fig 2h cited? In line 159, is Fig 2h a typo? Did the authors mean to cite Extended Fig 2a?

We apologize for the misplaced figure citations in the text. This sentence was intended to provide a brief summary of all experiments shown in Fig. 2 and Extended Data Fig. 3. Therefore, we have removed the figure citations from this sentence.

Changes in the text:

(Line 192-193) which are dysregulated in the *M14* cKO neurons by increased mRNA stability ~~(Fig. 2h, Extended Data Fig. 3e).~~

21) Fig 2. Adding a frequency distribution plot of m6A stoichiometry and the cutoff for separating

m6A RNAs vs non m6A-RNAs can help the audience understand the overall m6A modification landscape.

We appreciate the reviewer's suggestion, as reviewer #3 raised the same concern. We demonstrate the schematics and quality validation of m^{6}A-SAC-seq on Revised Extended Data Fig. 2a-b.

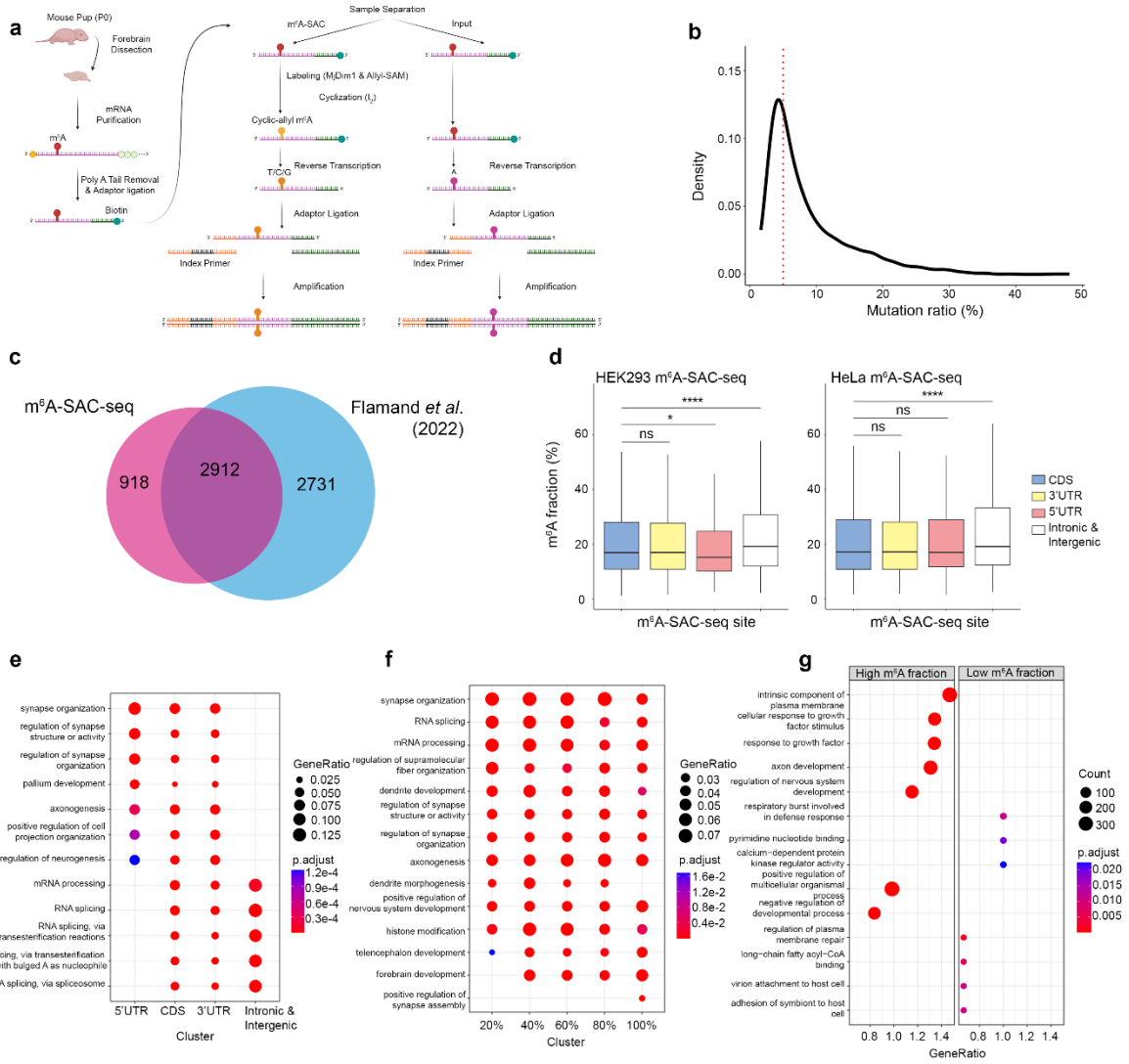

Revised Extended Data Fig. 2. Unique characteristics of single base-pair resolution m6A map in the developing brain through m^{6}A-SAC-seq. (a) Schematic of m^{6}A-SAC-seq performed on P0 mouse forebrain samples from WT and Nestin-Cre Mettl14 cKO mice. (b) Density plot showing the distribution of mutation ratios based on m^{6}A-SAC-seq. (c) Venn diagram comparing the m6A-SAC-seq and DART-seq results. (d) The m6A stoichiometry in different RNA regions, including the 3'UTR, CDS, 5'UTR, intronic, and intergenic regions. The boxplot represents differences compared with the CDS. (HEK293 CDS n=5911, 3'UTR n=4710, 5'UTR n= 328, Intronic & Intergenic n=717; HEK293 CDS compared with: 3'UTR P = 0.8894, 5'UTR P = 0.04083, Intronic & Intergenic P = 4.65e-06) (HeLa CDS n=4933, 3'UTR n=4731, 5'UTR n= 200, Intronic & Intergenic n=547; HeLa CDS compared with: 3'UTR P = 0.6093, 5'UTR P = 0.7014, Intronic & Intergenic P = 8.13e-07). (e) Gene Ontology analysis of RNA depending on the position

of m6A modifications. (f) Gene Ontology analysis of RNA depending on m6A stoichiometry. (g) Gene set enrichment analysis (GSEA) summary dot plot for the position in the m6A fraction ranked genes. Significance was evaluated using two-tailed unpaired Student's t-tests (d). ns, not significant; *P < 0.05, **P < 0.01, ****P < 0.0001.

22) Line 194-195: "transcripts with high m6A stoichiometry were less stabilized than transcripts with low m6A stoichiometry in the M14 cKO neurons". This observation is interesting and anti-intuitive. The authors stated in lines 202-203 "This suggests the presence of additional functions of m6A-tagging beyond mRNA degradation in the brain". However the statement does not address the phenomenon. Additional discussions on potential regulatory mechanisms would be appreciated.

Thank you for this insightful comment. We agree that this is an intriguing and somewhat counterintuitive finding—that transcripts with high m^{6}A stoichiometry appear more stable than those with low stoichiometry in *Mettl14* cKO neurons. We interpret this observation as follows:

1) As shown in Fig. 2c–e, m^{6}A stoichiometry is generally higher in the 3′UTRs of neurodevelopmental transcripts. Interestingly, high-stoichiometry transcripts are *less destabilized* in WT neurons (Fig. 2g; Extended Fig. 3d)

2) A stoichiometry of 60% does not imply that each transcript is 60% methylated, but rather that 60% of transcripts within a given population carry an m^{6}A modification. According to the classical model, m^{6}A-modified transcripts are typically more prone to degradation; thus, one would expect high-stoichiometry transcripts to be less stable.

3) The opposite trend observed in our data suggests that, in neurons, m^{6}A may exert additional functions beyond promoting mRNA degradation—potentially related to mRNA localization, translation efficiency, or RNP complex stabilization. Specifically, m^{6}A-tagged transcripts that primarily associate with the degradation-related YTHDF2 complex (lacking the transport-associated cofactors FMRP and KIF5C) are likely to undergo rapid decay, resulting in lower apparent m^{6}A stoichiometry. In contrast, transcripts incorporated into the YTHDF2–FMRP–KIF5C transport complex are protected from degradation and transported to distal axons. In this case, the m^{6}A-tagged transcripts are preserved and thus contribute to higher apparent m^{6}A stoichiometry. Consequently, these stabilized, transport-associated m^{6}A-tagged transcripts may exhibit higher m^{6}A stoichiometry compared with those primarily targeted for degradation.

We have revised the text to clarify this point and now include a brief discussion on possible regulatory mechanisms underlying this observation.

Changes in the text:

(Line 187-201) Interestingly, based on m^{6}A stoichiometry data, we found that transcripts with high m^{6}A stoichiometry were less stabilized than transcripts with low m^{6}A stoichiometry in the *M14* cKO neurons (Fig. 2g). This tendency became more evident when comparing the top 10% of m^{6}A stoichiometry transcripts to the bottom 10% (Extended Data Fig. 3d). Altogether, these results support that m^{6}A-tagged transcripts are directly related to neurodevelopmental processes and axon development in the postnatal brain, which are dysregulated in the *M14* cKO neurons by increased mRNA stability. Of note, the results of m^{6}A-SAC-seq and mRNA stability assay imply that high m^{6}A stoichiometry transcripts related to axon development (Fig. 2h, Extended Data Fig. 3e) are not solely regulated at the level of RNA stability as previously described [13]. One possible explanation is that m^{6}A-tagged transcripts are differentially associate with effector complexes—some promoting decay, others conferring stability—resulting in variable m^{6}A stoichiometry among transcript populations. This suggests that m^{6}A may exert additional functions beyond promoting mRNA degradation, potentially influencing mRNA localization, translation efficiency, or RNP complex stabilization in neurons.

23) Line 199. Which results suggest that “high m6A stoichiometry transcripts” are related to axon development? Please clarify.

For clarification, we changed the description as below:

Changes in the text:

(Line 193-196) Of note, the results of m^{6}A-SAC-seq and mRNA stability assay imply that high m^{6}A stoichiometry transcripts related to axon development (Fig. 2h, Extended Data Fig. 3e) are not solely regulated at the level of RNA stability as previously described [16].

24) The gene names analyzed for qPCR need to be given in Lines 211 and 212.

As suggested, we added gene names for qPCR analysis to the text.

Changes in the text:

(Line 209-210) The enrichment of previously reported axonally localized mRNAs, such as *Abce1*, *Gtpbp4*, and *Npm1*, [17] was confirmed by qPCR (Extended Data Fig. 4b).

25) Lines 257-259. Possibly the embryonic expression of the YTHDFs is not as important as the perinatal stage (P0-P5) when axons develop. The input data in m6A-SAC-seq data may provide better rationale for this argument.

Thank you for the thoughtful suggestion. In response, we examined their expression using the input data from our m^{6}A-SAC-seq and applied a standard bulk RNA-seq analysis workflow to quantify transcript abundance. The average TPM values for *Ythdf1*, *Ythdf2*, and *Ythdf3* in WT and *Mettl14* Nestin-Cre cKO samples are summarized below.

Sample	Ythdf1	Ythdf2	Ythdf3

WT	5052	3849	4112
cKO	7217	7416	5135

All three YTHDF family genes showed expression levels exceeding 3000 TPM, indicating sufficiently high expression during the perinatal stage of the mouse brain. Interestingly, the cKO samples exhibited higher expression of all three *Ythdf* genes than WT, which may reflect their regulation by m^{6}A, as *Ythdf* transcripts are known m^{6}A targets. Because the perinatal brain expresses substantial levels of all three *Ythdf* genes, we additionally performed knockdown experiments for *Ythdf1* and *Ythdf3*, which demonstrated that *Ythdf2* is primarily responsible for the growth cone phenotypes in differentiating neurons (Revised Extended Data Fig. 6b-e).

26) Line 301. “Select” should be added in front of “mRNA”.

27)Line 306. Again “Select” should be added in front of “mRNA” to avoid giving the audience the impression that this is a general phenomenon.

Thanks for the helpful suggestions. We agree with your points and have made the corrections in the text below:

Changes in the text:
(Line 313-315) Altogether, we hypothesize that YTHDF2 does not simply degrade RNAs in neuronal context and may protect and promote distal localization of selected mRNA.

(Line 320-322) These findings indicate that the loss of YTHDF2 function has a negative impact on selected mRNA localization in neurites, consistent with previous results observed in m6A depletion conditions (Fig. 3f-g).

28) Extended Fig. 1g: presenting the data as a percentage would be more meaningful. The exact N numbers should be kept in the figure legend or the text.

We appreciate the reviewer’s suggestion. We present the data as percentages and update the Extended Figure. 1h legend as below:

Changes in the text:

(Line 1103) The percentage of mCherry$^+$ cells was quantified in (h)

We appreciate the reviewer’s suggestion. We now present the data as percentages and have revised the Extended Data Fig. 1h legend as follows:

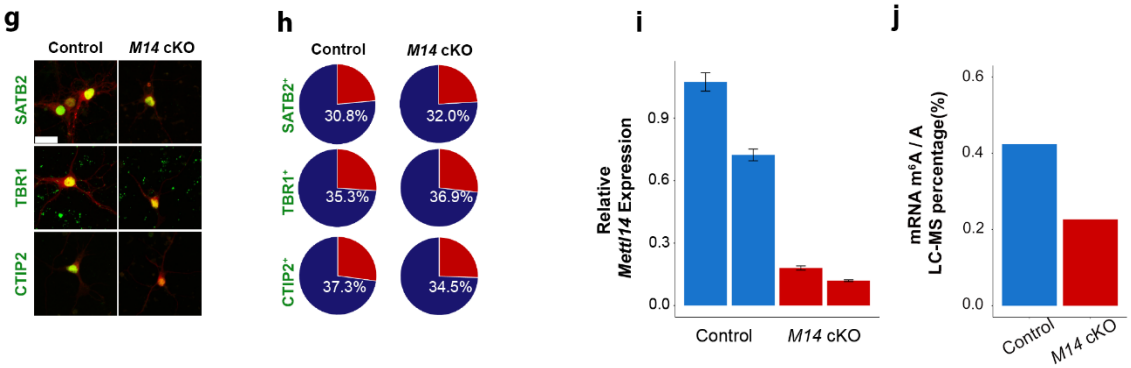

Revised Extended Data Fig.1. Loss of *Mettl14* leads to reduced contralateral axon projection, arborization, and neurite length. **(g)** Cortical markers SATB2, CTIP2, and TBR1 in *M14* cKO and control upper-layer neurons after AAV-mCherry-IRES-Cre virus infection at DIV1 and fixation at DIV6. The percentage of mCherry$^+$ cells was quantified in (h). **(i)** Validation of *M14* cKO in cortical neurons at DIV6 by qPCR. Values represent mean ± SEM after being normalized by GAPDH expression. **(j)** Validation of m^{6}A depletion in cortical neurons at DIV6 by LC-MS analysis.

29) Does each dot in Fig.3f, h, 4i, 5f, h, 6 e,g,i represent a single RNA puncta? How many neurons have contributed to the analysis?

Yes, each dot represents a single punctum. About 15-40 neurons were analyzed, and the exact number is indicated in the figure legend of each corresponding density plot (Revised Figs. 3f, 3h, 4i, 5f, 5h, 6g, and 6i).

30) In line 288, the authors suggested that YTHDF2 affects axon branching, however, no experiment/quantification in the manuscript supports this claim. The claim can be removed or additional analysis can be provided.

We appreciate the reviewer's comments. As shown in Supplementary Movies 3 and 4, *Ythdf2* cKO neurons exhibit abnormal branching and transient protrusions during axon projection. To further address this, we quantified the frequency of transient protrusions along the axonal shaft in *Mettl14* cKO and *Ythdf2* cKO neurons compared with controls (Revised Fig. 1h, Fig. 4f).

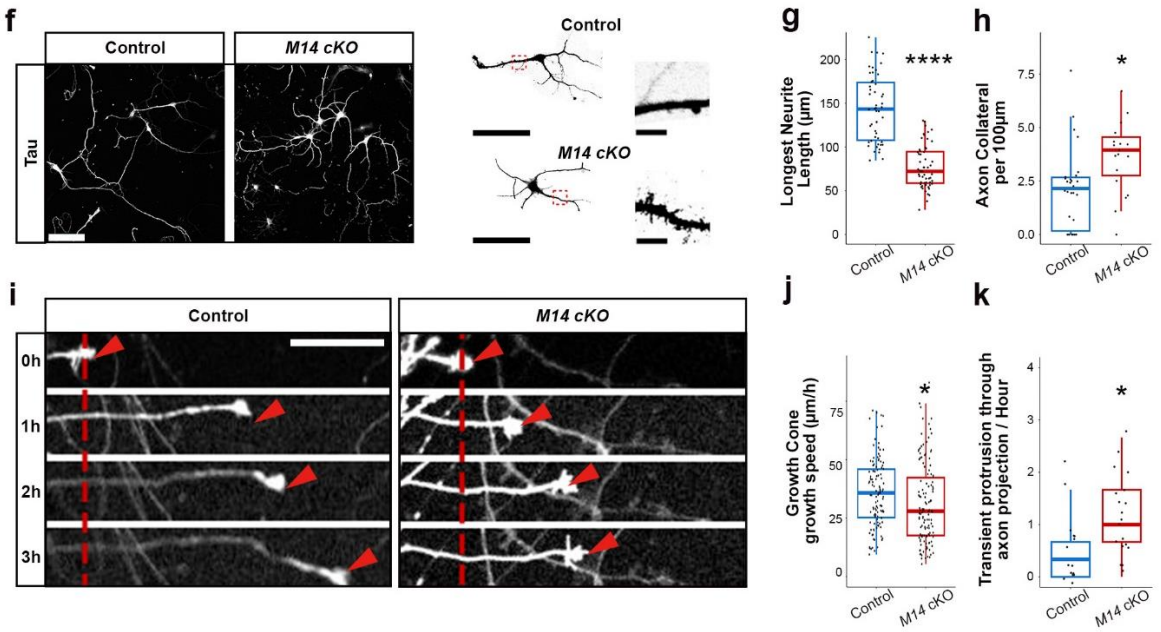

Revised Fig. 1. *Mettl14* deletion during corticogenesis leads to reduced axon projection, shorter neurite length, increased axon collaterals, and slower growth cone dynamics. (f-j) *M14* cKO primary neuron exhibited abnormal neurite growth at DIV6. Shown in **(f)** are representative confocal images and skeletal images (scale bars: 100 μm). The right panels show an enlarged view of squared regions (scale bars: 10 μm). Neurite length and collateral branching frequency were quantified in **(g)** (Control n=50, *M14* cKO n=56; $P < 2.2e\text{-}16$) and **(h)** (Control n=30, *M14* cKO n=19; $P=0.03536$). **(i)** Live imaging of growth cones in control and *M14* cKO neurons over 3 hours at DIV6. Red arrowheads indicate the locations of growth cones (scale bar: 20 μm). Shown in **(j)** is the quantification of total growth length divided by tracking time. (Control n=114, *M14* cKO n=134; $P=0.02441$). **(k)** The quantification of the transient protrusion. (Control n=15, M14 cKO n=19, $P=0.01692$). Significance was evaluated using two-tailed unpaired Student's t-tests (c, d, g, h, and j). The significance of RFP intensity across the midline was evaluated using two-way ANOVA (b). $*P < 0.05$, $**P < 0.01$, $****P < 0.0001$.

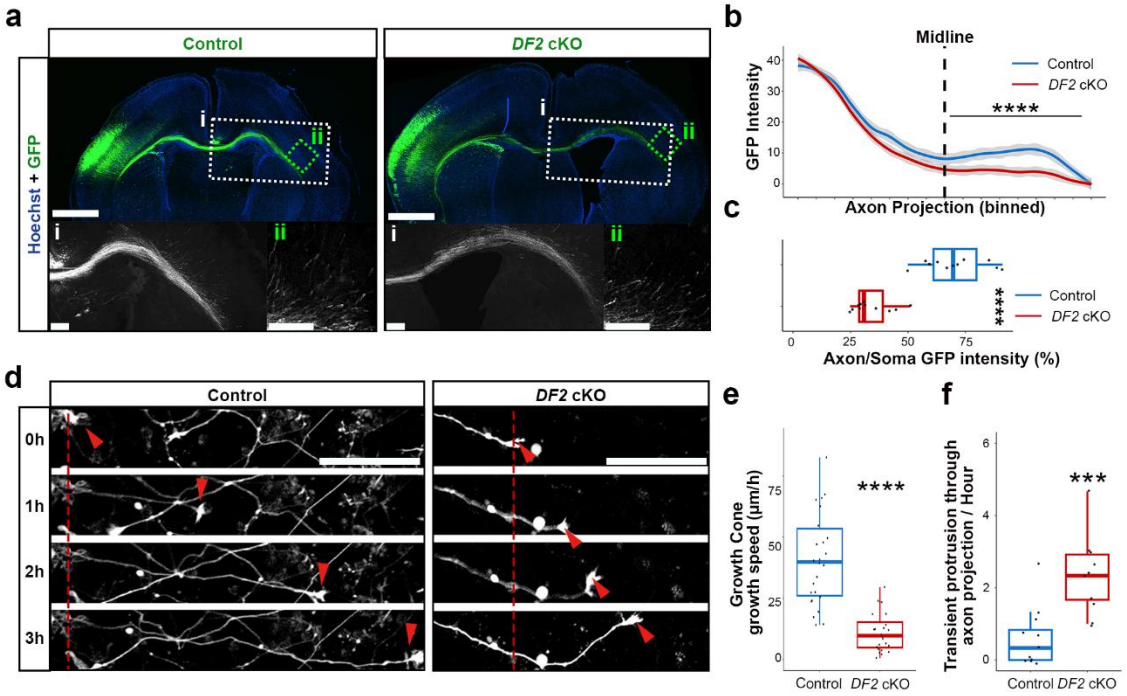

Revised Fig. 4. *Ythdf2* deletion reduces axonal projection and neurite length and impairs growth cone dynamics in *DF2* cKO. (a-c) Corpus callosal axon projections in control and *DF2* cKO P5 brains, examined by *in utero* electroporation. **(a)** The upper panel shows ipsilateral to contralateral axon projections crossing via the white matter and the corpus callosum area in coronal sections. The lower panels (i, ii) are selected and magnified to represent the corpus callosum and projected neurons from the S1 region layer 2/3 neurons (scale bars: 1000 μm; i, ii scale bars: 200 μm). **(b)** The frequency distribution plot represents GFP intensity during the axon projections from ipsilateral to contralateral positions (n=3 for each, confidence level=0.99, *P*<2e-16). **(c)** The integrated density of the GFP signal of axons per soma was quantified (n=11 for each; *P*=2.09E-07). **(d)** Neurite projections within 3 hours were tracked under a confocal microscope at DIV6 (scale bars: 20 μm). Shown in **(e)** is the quantification of total growth length divided by tracking time (Control n=26, *DF2* cKO n=24, *P*=1.51E-07), and **(f)** is the quantification of the transient protrusion (Control n=11, DF2 cKO n=10, *P*= 0.0006217).

Changes in the text:

(Line 140-143)

Last, we also examined the dynamics of growth cones by live imaging, which revealed that *Mettl14* deletion significantly reduced the velocity of growth cone advance and increased transient protrusion formation compared to the control at DIV6 (Fig. 1i-k, Extended Movie 1, 2).

(Line 298-301)

We performed live imaging experiments to investigate growth cone mobility and dynamics, and found that *Ythdf2* deletion notably reduced growth cone dynamics and increased transient protrusion formation compared to the control at DIV6 (Fig. 4d-f, Extended Movie 9, 10).

31) Extended Fig. 4b: beta-actin may not be the best loading control here given that its expression might be affected in the DF2 KO model.

We appreciate the reviewer's comments. We performed western blot again with GAPDH as a loading control which are not target of DF2 KO model. (Extended Fig. 6g)

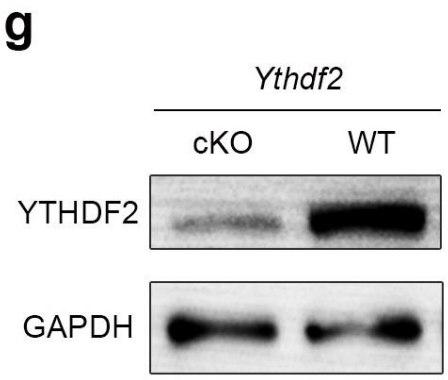

Extended Data Fig. 6. Loss of *Ythdf2* leads to a reduced survival rate, lower body weight, motor impairments, and disrupted neuron projection
(g) Validation of *DF2* cKO in the mouse cortex through western blotting control with GAPDH.

32) Extended Fig. 5: Negative controls using combinations of IgG with the other target protein antibody should be performed to validate the puncta.

We appreciate the reviewer's suggestion, as Reviewer #3 raised a similar request regarding the PLA negative control. To address this, we performed PLA assays for DF2–IgG, FMRP–IgG, and IgG–KIF5C in WT mouse primary neurons at DIV6 (Revised Extended Data Fig. 7c). As a result, only minimal background PLA signals were detected, which can be considered negligible.

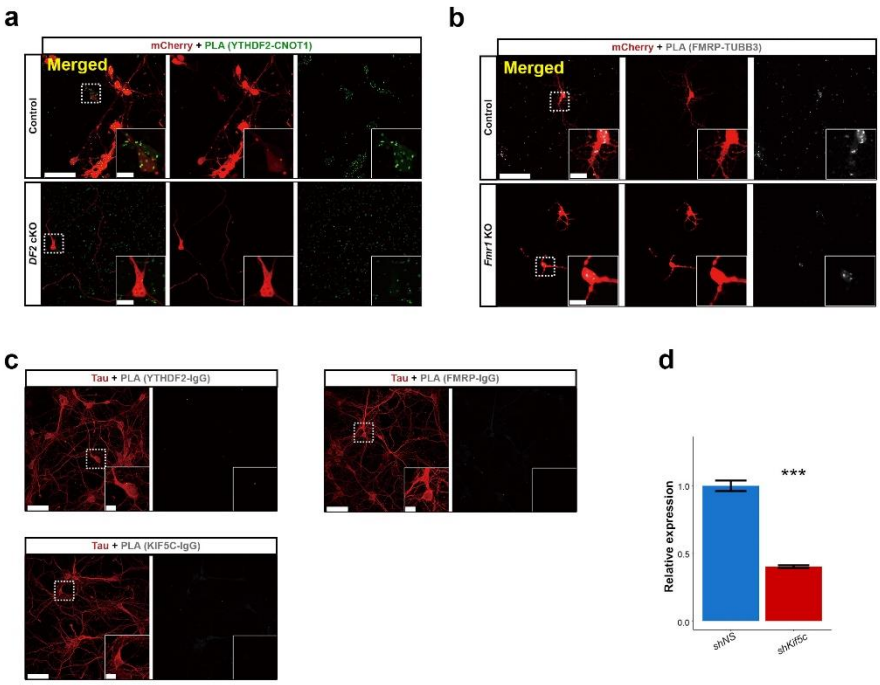

Extended Data Fig. 7. Validation of PLA experiments and *shKif5c*.
(a-c) Validation of Proximity Ligation Assay (PLA) experiments with negative control. YTHDF2-CNOT1 PLA signal significantly reduced in *DF2* cKO represented on **(a)** (scale bar: 50μm, lower panel scale bar: 10μm). FMRP-TUBB3 PLA signal significantly reduced in *Fmr1* KO represented on **(b)** (scale bar: 50μm, lower panel scale bar: 10μm). Signals appearing in mCherry-negative areas are presumed to originate from cells that were not infected by AAV-mCherry-IRES-Cre viruses. **(c)** YTHDF2, FMRP, and KIF5C PLA with IgG control. PLA signal significantly reduced with IgG represented on (c) (scale bar: 50μm, lower panel scale bar: 10μm). **(d)** Validation of *Kif5c* KD in N2A by qPCR. Values represent mean ± SEM after being normalized by GAPDH expression

33) Lines 345-346. Fig 6a. The motifs of FXR2 and FMRP are similar to the m6A motif in m6A-SAC-seq. Given that both proteins have been identified as reader proteins of m6A in a previous report (https://doi.org/10.1038/nsmb.3462), these two proteins may be directly recruited to m6A-mRNAs independently of YTHDF2 binding.

We thank the reviewer for raising this important issue, which was also noted by Reviewer #3. To ensure that the m^{6}A DRACH motif does not interfere with the motif enrichment analysis, we reanalyzed the sequences within the 3′UTRs of Q2 mRNAs. Specifically, we performed motif enrichment analysis using AME on the ±50 bp regions surrounding the DRACH motifs of m^{6}A sites in Q2 mRNAs.

As a result, we confirmed that the FMRP-binding motif was significantly enriched near the m^{6}A sites ($p = 7.25 \times 10^{-3}$) (Revised Fig. 6a), whereas FXR1 and FXR2 showed only weak enrichment ($p = 2.84 \times 10^{-1}$ and 2.17×10^{-1}, respectively). These findings suggest that potential FMRP-binding sites are positioned within ~50 bp of m^{6}A sites, rather than directly overlapping them, which may facilitate enhanced mRNA–DF2–FMRP interactions.

Revised Fig. 6. FMRP interacts with YTHDF2 to assist m^{6}A-tagged mRNA transport to distal neurites of developing neurons.
(a) Motif enrichment analysis of the Q2 3'UTR m^{6}A proximal sequence (±50 bp).

Changes in the text:
(Line 376-383) Next, we hypothesized that YTHDF2 associates with other RBPs and selectively localizes mRNA to the distal axon depending on target RNA characteristics, including m^{6}A and 3'UTR sequence. When we examined m^{6}A stoichiometry across different RBP target mRNAs, FMRP target mRNAs exhibited significantly higher m^{6}A stoichiometry than non-target mRNAs (Extended Data Fig. 8a). To further evaluate our model, we performed motif enrichment analysis on sequences proximal to m^{6}A sites within the 3′UTRs of the Q2 and Q1 groups (Fig. 3b) [18]. As a result, we found FMRP binding motifs were enriched in Q2 3'UTR sequences, particularly near m6A sites, compared with Q1 3′UTR sequences (Fig. 6a, Extended Data Fig. 8b).

34) Fig. 6f: Better representative images matching the quantification results are required.

We appreciate the reviewer's comment. We have updated the representative images in Figures 5 and 6, and additionally included Tau immunocytochemistry data to clarify that the PLA signals overlap with axonal regions.

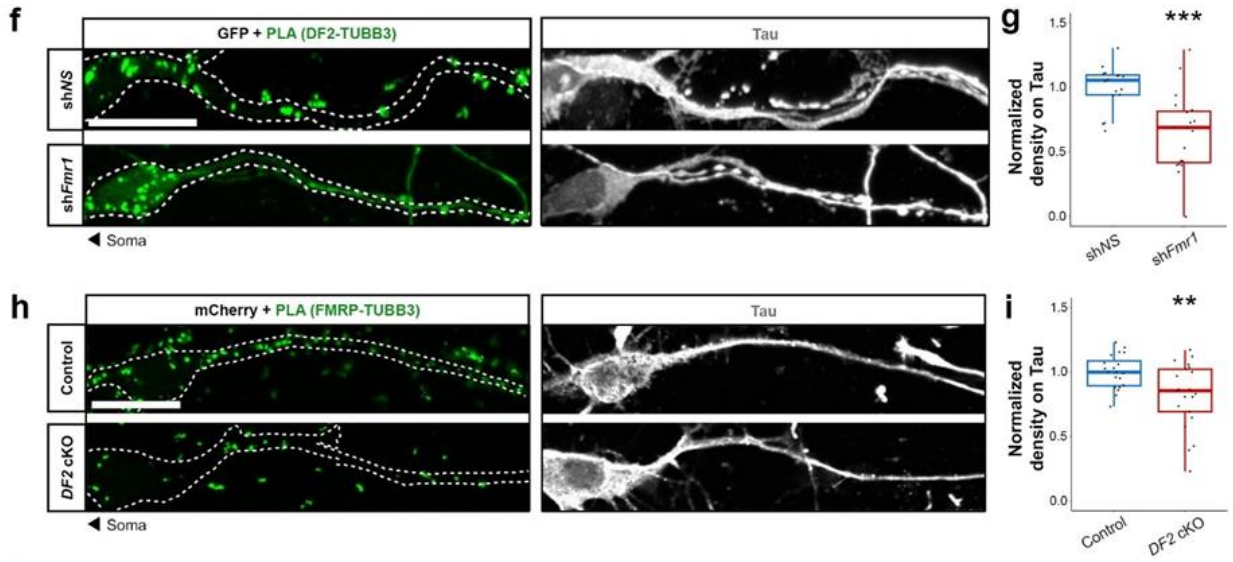

Revised Fig. 6. FMRP interacts with YTHDF2 to assist m^{6}A-tagged mRNA transport to distal neurites of developing neurons.

(f-g) YTHDF2 localization to neurites decreased in *Fmr1* KD mouse primary neurons. Shown in (f) are representative PLA signals (green) and Tau indicating endogenous YTHDF2-TUBB3 associations in control and *Fmr1* KD mouse primary neurons (Scale bar: 20μm). The relative density on tau is quantified in (g) (Control n=16, *Fmr1* KD n=19, *P*= 0.0002645). **(h-i)** FMRP localization to neurites decreased in *DF2* cKO mouse primary neurons. Shown in (h) are representative PLA signals (green) and Tau indicating endogenous FMRP-TUBB3 associations in control and *DF2* cKO mouse primary neurons (Scale bar: 20μm). The relative density on tau is quantified in (i) (Control n=20, *DF2* cKO n=21, *P*= 0.006918).

35) Lines 420-421, the authors concluded that "YTHDF2 along the axon significantly decreases under m6A depletion condition (Fig. 5g-h)". However, Fig 5g-h represents initial dendrites/neurites.

As described above, we performed co-staining with the axonal marker Tau in the PLA experiments to clearly identify and confirm that the PLA signals were localized within axons.

Reviewer #2 (Remarks to the Author):

Reviewer comments

This study investigates the role of m6A mRNA modifications in the regulation of neural development, particularly focusing on mRNA transport in developing neurons. This study demonstrates that knockout of Mettl14 in postmitotic neurons leads to impaired axonal projection, with RNA-seq and single-molecule in situ hybridization showing mislocalization of mRNAs in the neurites of neurons with m6A loss-of-function. Furthermore, the research identifies YTHDF2 as a key m6A reader protein that facilitates the distal transport of m6A-tagged mRNAs in callosal projection axons by interacting with FMRP, guiding the YTHDF2 complex to promote the efficient

transport of m6A-tagged mRNA rather than its degradation. Although the topic is timely and has significant implications for advancing our understanding of mRNA regulation in neurons, the study has several limitations that affect its overall rigor and impact. The findings on YTHDF2's role in mRNA transport and its interaction with FMRP are intriguing, but the lack of robust methodological detail weakens their support. This limited clarity and depth ultimately reduce the study's potential impact on the field.

We appreciate the reviewer's thorough summary and constructive critiques. Below, we provide detailed responses to each of the reviewer's comments.

Major comments:

1) The interaction between FMRP and YTHDF2, as proposed in the study, is an intriguing finding. However, the authors fail to provide a clear explanation of how FMRP modulates YTHDF2's function in the context of mRNA transport. Is FMRP acting as a direct modulator of YTHDF2's mRNA binding activity, or is it facilitating the transport process through indirect interactions? This lack of clarification leaves the reader uncertain about the specific mechanism by which FMRP influences mRNA transport. More detailed mechanistic insights, ideally supported by functional experiments, are needed to fully substantiate the proposed model.

We agree with the reviewer's important suggestion to further strengthen the YTHDF2–FMRP interaction model. We examined the YTHDF2–TUBB3 interaction under FMRP-depleted conditions using PLA experiments. Indeed, YTHDF2 localization to neurite microtubules was significantly reduced upon *Fmr1* knockdown (Revised Fig. 6f–g). We next assessed the YTHDF2–KIF5C interaction under FMRP-depleted conditions by PLA and found that YTHDF2 interaction with KIF5C was also significantly reduced following *Fmr1* knockdown (Revised Fig. 6m–n). Together, these results indicate that FMRP facilitates YTHDF2 interactions with motor proteins and neurite microtubules, thereby promoting distal localization of m^{6}A target mRNAs.

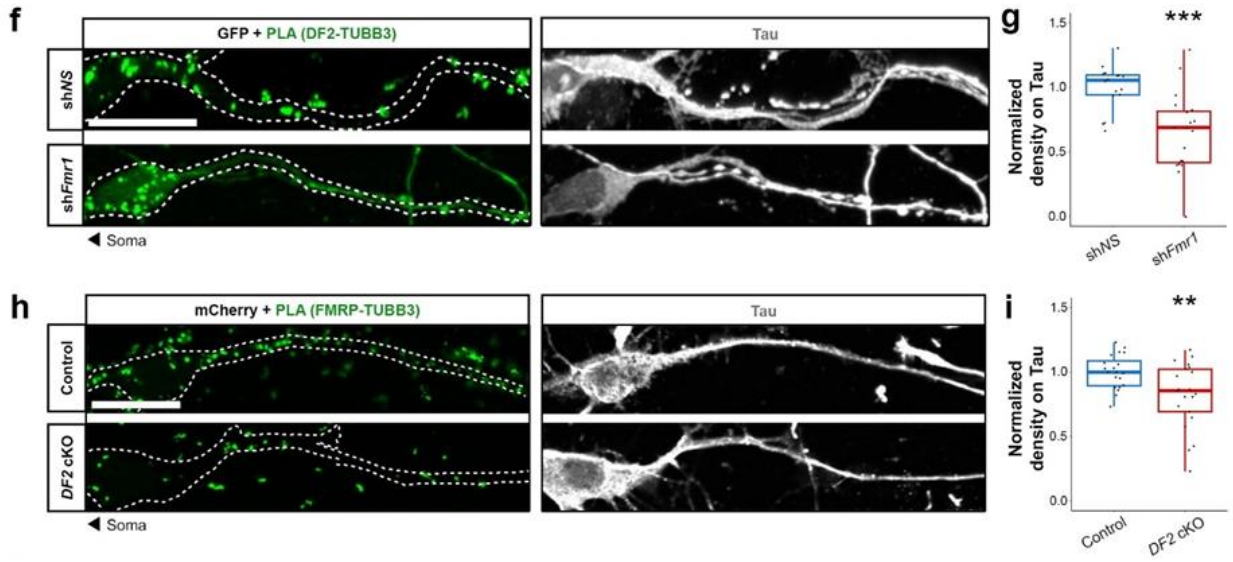

Revised Fig. 6. FMRP interacts with YTHDF2 to assist m^{6}A-tagged mRNA transport to distal neurites of developing neurons.

(f-g) YTHDF2 localization to neurites is decreased in *Fmr1* KD condition. Shown in (f) are representative PLA signals (green) and Tau staining indicating endogenous YTHDF2-TUBB3 associations in control and *Fmr1* KD mouse primary neurons (Scale bar: 20μm). Quantification of the relative PLA signal density along Tau-positive neurites is shown in (g) (Control n=16, *Fmr1* KD n=19, *P*= 0.0002645). **(h-i)** FMRP localization to neurites decreased in *DF2* cKO mouse primary neurons. Shown in (h) are representative PLA signals (green) and Tau staining indicating endogenous FMRP-TUBB3 associations in control and *DF2* cKO mouse primary neurons (Scale bar: 20μm). Quantification of the relative PLA signal density along Tau-positive neurites is shown in (i) (Control n=20, *DF2* cKO n=21, *P*= 0.006918).

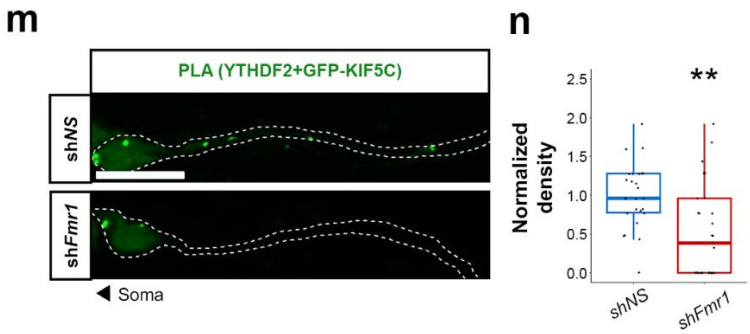

Revised Fig. 6. FMRP interacts with YTHDF2 to assist m^{6}A-tagged mRNA transport to distal neurites of developing neurons.

(m-n) YTHDF2-KIF5C complex localization to distal neurites decreased in *Fmr1* KD mouse primary neuron. Shown in (m) are representative PLA signals (Green) showing YTHDF2+GFP-KIF5C association (Scale bar: 20μm). The relative density is quantified in (n) (Control n=26, *Fmr1* KD n=29, *P*=0.001066). Significance was evaluated using two-tailed unpaired Student's t-tests (n). $^{**}P < 0.01$.

In addition, knockdown of *Fmr1* significantly increased the interaction between YTHDF2 and CNOT1, indicating that FMRP competitively inhibits the association of m^{6}A-tagged mRNAs/YTHDF2 with the mRNA degradation machinery (Revised Fig. 6d–e). These findings further support the model that FMRP facilitates axonal localization of a subset of m^{6}A-tagged mRNAs by promoting YTHDF2 interactions with motor proteins and microtubules, while simultaneously inhibiting target mRNA degradation through competitive interaction with YTHDF2 against the RNA degradation machinery. We added these new data to the revised text and discussion.

(Line 397-408) To evaluate the functional significance of FMRP in the association of YTHDF2 with microtubules, we conducted a PLA experiment between YTHDF2 and TUBB3 in *shNS* and sh*Fmr1*-treated mouse primary neurons. The results revealed a significant decrease in YTHDF2-TUBB3 PLA signals in the neurites of *Fmr1* knockdown neurons compared to those in control neurons (Fig. 6f-g, Extended Data Fig. 8d-e), suggesting that FMRP facilitates the microtubule association of YTHDF2. Conversely, FMRP-TUBB3 PLA signals were markedly reduced in the neurites of *Ythdf2* knockout neurons compared to those in control neurons (Fig. 6h-l, Extended Data Fig. 8f-g). In addition, the YTHDF2–KIF5C PLA signal was reduced in *shFmr1*-treated neurons, indicating that FMRP facilitates the association of YTHDF2 with

motor proteins in axons (Fig. 6m–n). Collectively, these findings suggest a cooperative interaction between YTHDF2 and FMRP that links m⁶A-tagged mRNAs to microtubules and motor proteins within neurites.

(Line 453-465) Furthermore, FMRP inhibits the interaction of YTHDF2 with the RNA degradation machinery (Fig. 6d-e). These results suggest that m^{6}A-tagged mRNAs are selectively recognized either by the degradation or the transport complex, with FMRP playing a pivotal role in regulating the degradation and transport of m^{6}A-tagged mRNAs. Specifically, FMRP protects a subset of m⁶A-tagged mRNAs from degradation by inhibiting the interaction between YTHDF2 and the RNA degradation machinery, while simultaneously promoting their transport by enhancing the association of YTHDF2 with microtubules and motor proteins (Fig. 6f-g and Fig. 6m-n). Indeed, known FMRP target mRNAs have higher m^{6}A stoichiometry compared to FMRP non-target mRNAs (Extended Data Fig. 8a), and high m^{6}A stoichiometric mRNAs are less affected in their stability compared to low m^{6}A stoichiometric mRNAs upon Mettl14 depletion (Fig. 2g). Consistently, *Drosophila* YTHDF directly interacts with FMRP to cooperatively inhibit the translation of mRNAs involved in axonal growth regulation [19].

2) The study would greatly benefit from the inclusion of live imaging experiments to directly observe the co-transport of RNA-binding proteins (RBPs) and their associated mRNAs within the axons of developing neurons. While the manuscript suggests that YTHDF2 mediates mRNA transport, it remains unclear how the RBP interacts with the mRNA in real-time and how these dynamics unfold within the complex environment of the axon.

We thank the reviewer for this valuable suggestion, which was also raised by Reviewer #1. To address this, we performed live-cell mRNA imaging using the MS2 reporter system. Specifically, we used a BFP-Actb-3′UTR-MS2x24 reporter construct that retains the endogenous 3′UTR m⁶A motif (the 1217th position, 5nt after the STOP codon) identified by m^{6}A-SAC-seq. The reporter was co-transfected into primary neurons together with MCP-GFP-HA, which binds to the reporter RNA and enables visualization via GFP fluorescence. (Revised Fig. 3h) As a result, we detected RNA granules in neurites of DIV6 primary neurons under both control and *Mettl14* cKO conditions. Notably, anterograde transport of RNA granules was markedly reduced in *Mettl14* cKO neurons (Revised Fig. 3i-j, Extended Movie 3, 4). Moreover, the total motile time of mRNA reporter drastically decreased in *Mettl14* cKO conditions. (Revised Fig. 3k)

It is well established that neurons are polarized cells with axonal microtubules oriented in a plus-end–out configuration [9]. Consistent with this, our LC–MS/MS data revealed that YTHDF2 interacts with kinesins, including KIF5C, in an m⁶A-dependent manner (Revised Fig. 5b-c). Moreover, we demonstrated direct interactions between YTHDF2, TUBB3, and KIF5C using PLA and co-immunoprecipitation assays (Revised Fig. 5, 6). Together, these findings suggest that m⁶A-modified RNAs are transported to distal axons via anterograde movement mediated by the YTHDF2–kinesin complex.

Next, to examine the direct impact of m⁶A tagging on RNA localization, we generated a point-mutant reporter (BFP-Actb-3′UTRΔm⁶A-MS2x24) lacking the single m⁶A site. The mutant reporter

showed reduced anterograde transport of RNA granules and decreased total motile time compared with the wild-type construct (Revised Fig. 3i-n, Extended Movie 5, 6). These new results strongly support our original conclusion and further expand the mechanistic scope and impact of our study.

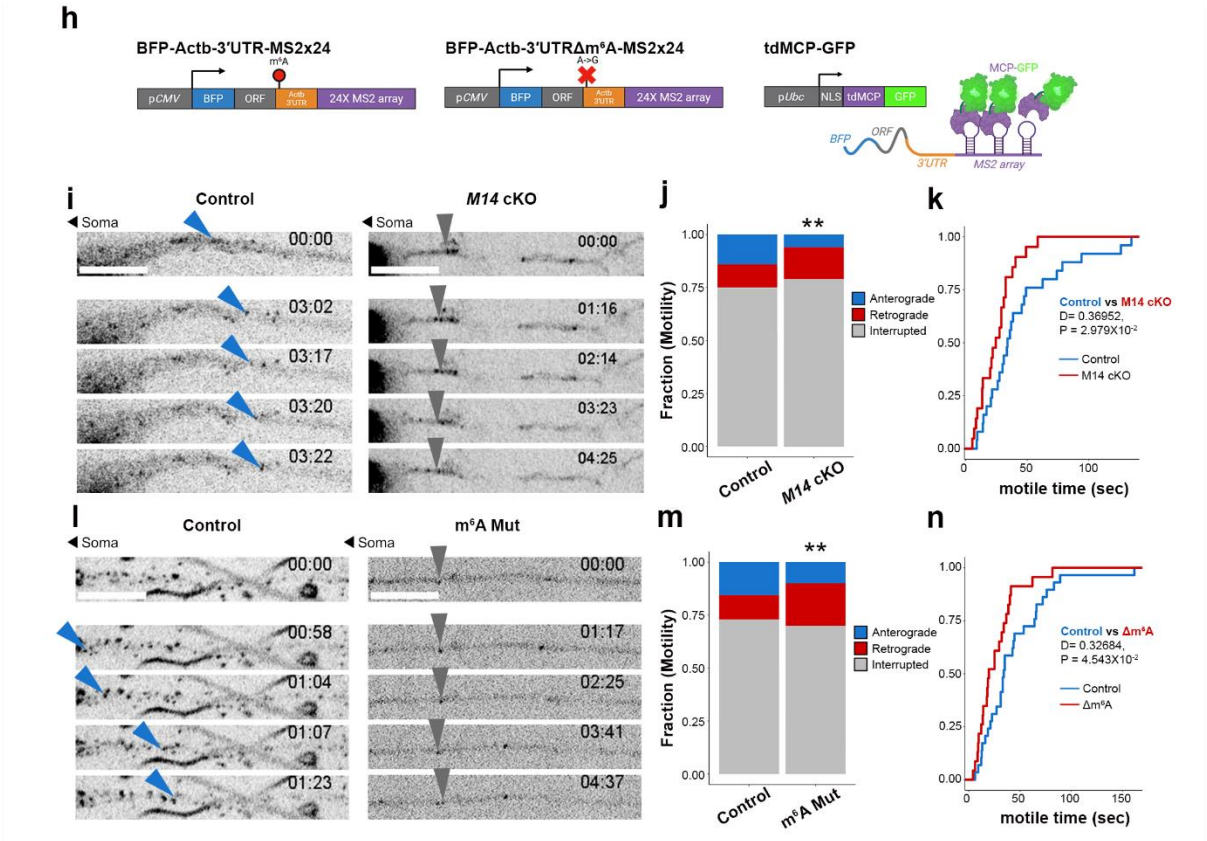

Revised Fig. 3. m^{6}A modification is crucial for the distal translocation of cytoskeletal mRNAs in differentiating neurons.

(h) The schematic diagram of RNA live imaging MS2 system. **(i-k)** *M14* cKO primary cultured neurons show depleted anterograde RNA localization. Shown in (i) anterograde (blue arrowheads) and interrupted (grey arrowheads) RNA reporter are indicated (scale bars: 10 μm). The RNA reporter dynamics were quantified in (j) (Control n=173, *M14* cKO n=181, *P*=0.007019). The total motile time of RNA granules was compared with each condition in (k) (Control n=25, M14 cKO n=21) (l-n). The m6A point-mutated reporter showed depleted anterograde RNA localization. Shown in (l) anterograde (blue arrowheads) and interrupted (grey arrowheads) RNA reporter are indicated (scale bars: 10 μm). The RNA reporter dynamics were quantified in (j) (Control n=148, Δm^{6}A n=130, *P*=0.007464). The total motile time of RNA granules was compared with each condition in (k) (Control n=29, *M14* cKO n=23) Significance was evaluated using two-tailed unpaired Student's t-tests (f, and g). The distribution difference of RNA motility between two groups was evaluated using the chi-square test (j, and k). The significance of two RNA motility time sets was evaluated using the Kolmogorov-Smirnov test (k, n). ns, not significant, *$P < 0.05$, **$P < 0.01$, ***$P<0.001$, ****$P < 0.0001$.

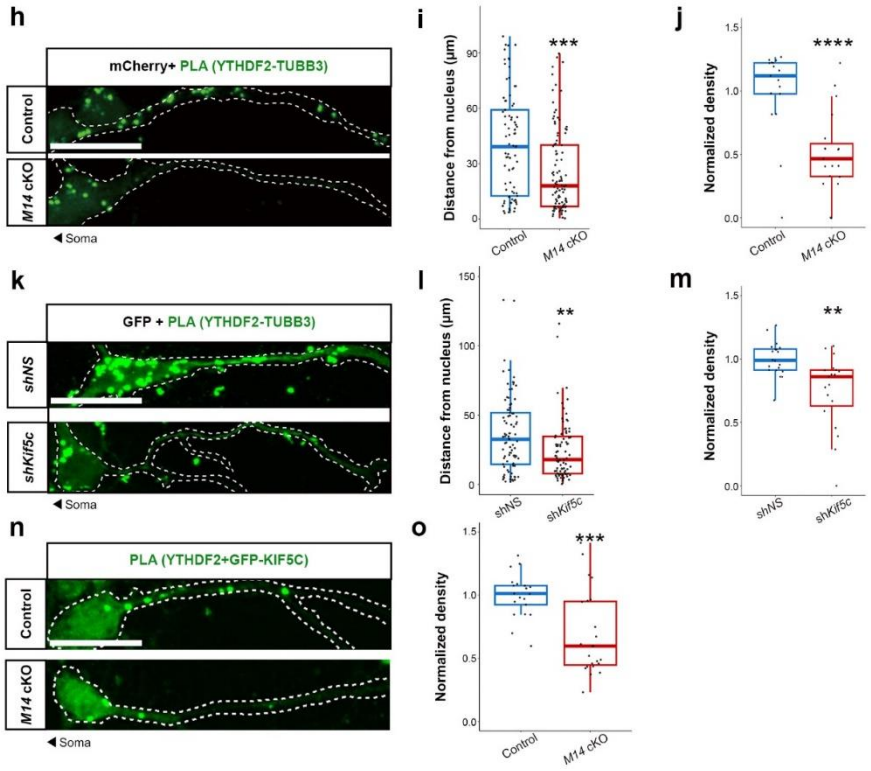

Revised Fig. 5. YTHDF2 interacts with the transport machinery and neurite microtubules in an m^{6}A-dependent manner. (h-j) YTHDF2 localization to distal neurite decreased in *M14* cKO mouse primary neuron. Shown in (h) are representative PLA signals (Green) showing endogenous YTHDF2-TUBB3 association (Scale bar: 20μm). The distance from the nucleus was quantified in (i) (Control n=81, *M14* cKO n=108, *P*=0.0001524) and the relative density is quantified in (j) (Control n=17, *M14* cKO n=19, *P*=8.88e-05). **(k-m)** YTHDF2 localization to distal neurites decreased in mouse primary neuron upon *Kif5c* knockdown. Shown in (k) are representative PLA signals (green) indicating endogenous YTHDF2-TUBB3 association in control and *Kif5c* knockdown conditions (scale bar: 20μm). The distance from the nucleus was quantified in (l) (Control n=89, *shKif5c* n=91, *P*=0.001227) and the relative density is quantified in (m) (Control n=20, *shKif5c* n=19, *P*=0.001124).
(n-o) YTHDF2-KIF5C complex localization to distal neurites decreased in *M14* cKO mouse primary neuron. Shown in (n) are representative PLA signals (Green) showing YTHDF2+GFP-KIF5C association (Scale bar: 20μm). The relative density is quantified in (o) (Control n=21, *M14* cKO n=23, *P*=0.0003697). Significance was evaluated using two-tailed unpaired Student's t-tests (i, j, l, m, and o). ns, not significant, $^{**}P < 0.01$, $^{***}P<0.001$, $^{****}P<0.0001$

In addition, we repeat the lysosome live imaging with higher resolution and an enlarged scale. As a result, lysosome motility did not change in the M14 cKO condition. (Revised extended figure. 5e-h) Not only speed and total displacement, but the direction of total displacement also did not change in the M14 cKO condition. (Revised Extended Data Fig. 5e-h) These data indicate that the general transport machinery was unaffected by m6A depletion.

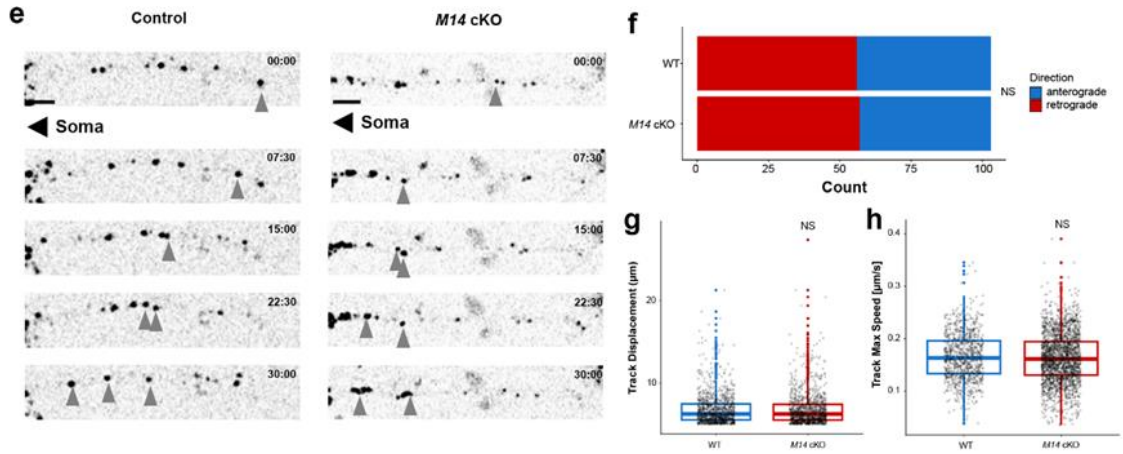

Extended Data Fig. 5. Loss of *Mettl14* leads to a reduced neuronal gene expression and localization in axons. **(e-h)** Live imaging of lysosomes in *M14* cKO and control cortical neurons at DIV6. Shown in (e) is a time-lapse image representing lysosome dynamics over 30 minutes (scale bars: 10 μm). Direction of lysosome movement is counted in two categories, anterograde and retrograde, and validated in (f) (Control n=103, *M14* cKO n=103, *P*=0.1573). Lysosome track displacement length is quantified in (g) (Control n=1130, *M14* cKO n=1195, *P*=0.5133), and lysosome track max speed is quantified in (h) (Control n=1130, *M14* cKO n=1195, *P*=0.1509).
Significance was evaluated using two-tailed unpaired Student's t-tests (b, d, g, h), and Pearson's Chi-squared test (f). ns, not significant; $*P < 0.05$, $**P < 0.01$.

Changes in the text:

(Line 240-253) To directly visualize RNA transport through neurites, we employed the MS2 system[10]. We used HA-tdMCP-GFP and BFP–actin–3′UTR–24×MS2 reporters containing a conserved m⁶A site in the 3′UTR (at the 1217th position, located xx nt downstream of the stop codon) (Fig. 3h). RNA dynamics were monitored in control and *Mettl14* cKO neurons using a spinning-disk microscope. Interestingly, anterograde RNA movement was significantly reduced under *M14* cKO conditions (Fig. 3i-j, Extended Movie 3,4). Moreover, the total motile time of RNA was also reduced under *M14* cKO conditions (Fig. 3k). To examine the direct role of m⁶A modification in RNA transport, we generated a mutant reporter, BFP–actin–3′UTRΔm⁶A–24×MS2, by introducing an A→G substitution at position 1217 to prevent m⁶A modification. RNA granule movement was then compared between the wild-type and Δm⁶A reporters in mouse primary neurons. As a result, anterograde RNA movement was markedly reduced in the Δm⁶A reporter (Fig. 3l-n, Extended Movie 5,6). These findings demonstrate that a single m⁶A modification within the 3′UTR is critical for efficient anterograde transport of *Actb* mRNAs in developing neurons.

(Line 367-370) Lastly, we also performed YTHDF2-KIF5C PLA in WT and *M14* cKO neurons, observed reduced interactions between YTHDF2 and KIF5C in axons (Fig. 5i-j). These results suggest that the neuron-specific motor protein KIF5C connects YTHDF2 with microtubules to promote mRNA transport in a m⁶A-dependent manner.

(Line 524-529) For the RNA live imaging, we used phage-ubc-nls-ha-tdMCP-gfp (Addgene #30649), and pcDNA-puro-TagBFP-β-ACTIN-3′UTR-24xMS2 (Addgene #205161). For the point-mutant reporter (BFP-Actb-3′UTRΔm^{6}A-MS2x24) we used Site-directed Mutagenesis kit (Enzynomics, EZ004S) according to the manufacturer's instructions. In brief, reporter plasmid was amplified with a pair of primers substituting the conserved m6A site with a cytosine residue. Next, PCR product ligated and transformed in to E. coli for the selection and amplification.

(Line 609-615) For the RNA live imaging, we co-electroporated phage-ubc-nls-ha-tdMCP-gfp, with pcDNA-puro-TagBFP-β-ACTIN-3′UTR-24xMS2 reporters which retains the endogenous 3′UTR m^{6}A motif (the 1217th position, 5nt after the STOP codon) to cortical neurons on a confocal glass-bottom dish and culture to the DIV5~6. Live images were acquired with a Nikon Eclipse Ti inverted microscope equipped with a CSU-10 spinning disk (Yokogawa, Tokyo, Japan), an EMCCD camera, and a 100× oil immersion objective (NA 1.49) for 5minutes with 500ms intervals.

(Line 829-833) For RNA live images, RNA molecules observed > 60 frames were selected for the consistency. Anterograde and retrograde movement were counted to calculate the fraction of transport and motile time. Movements longer than 2 μm were categorized to antero or retro group and less than 2 μm were categorized as interrupted group[11].

Next, we performed live-cell mRNA imaging using the *Actb* 3′UTR–MS2 reporter system in WT and *Ythdf2* cKO neurons. The anterograde transport of RNA granules was markedly reduced in *Ythdf2* cKO neurons compared with WT controls (Revised Fig. 4l, m, Extended Movie 11, 12). Moreover, the total motile time of mRNA reporter drastically decreased in *Mettl14* cKO conditions. (Revised Fig. 4n) These results directly demonstrate the active role of YTHDF2 in the transport of *Actb* mRNA and further strengthen our overall conclusion.

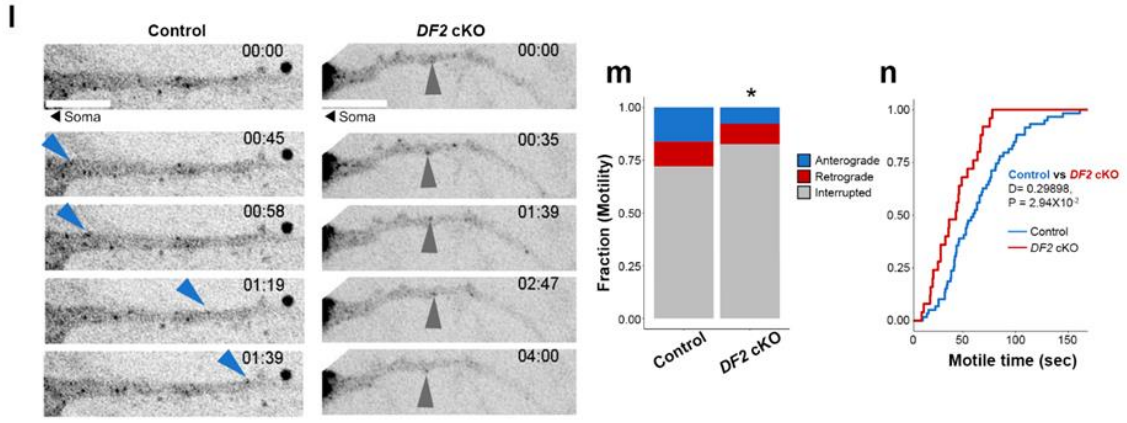

Revised Fig. 4. *Ythdf2* deletion reduces axonal projection and neurite length and impairs growth cone dynamics in *DF2* cKO. (l-n) *DF2* cKO primary cultured neurons show depleted anterograde RNA localization. Shown in (l) anterograde (blue arrowheads) and interrupted (grey arrowheads) RNA reporter are indicated (scale bars: 10 μm). The RNA reporter dynamics were quantified in (m) (Control n=211, *DF2* cKO n=143, *P*=0.04263). The

motile time of RNA reporter were compared with each condition in (n) (Control n=59, *DF2* cKO n=25). The significance of two gene sets and RNA motility time sets was evaluated using the Kolmogorov-Smirnov test (f and n). The distribution difference of RNA motility between two groups was evaluated using the chi-square test (m) $*P < 0.05$,

Changes in the text:

(Line 323-329) Next, we used HA-tdMCP-GFP and BFP–actin–3′UTR–24×MS2 reporters described above to visualize the RNA transport (Fig. 3h). The dynamics of reporter RNA granules were monitored in control and *DF2* cKO neurons using a spinning-disk microscope. As result, anterograde RNA movement was significantly reduced under *DF2* cKO conditions (Fig. 4l-n, Extended Movie 11,12). Moreover, the total motile time of RNA granules was also reduced under *DF2* cKO conditions (Fig. 4n), consistent with previous results in the m6A depletion condition and the m^{6}A mutant reporter (Fig. 3k, n).

(Line 330-334) Collectively, the YTHDF2 cKO model shows significant neurodevelopmental defects at the *in vivo* and *in vitro* levels. m^{6}A-modified mRNAs show decreased stability in the absence of YTHDF2, and YTHDF2 promotes the anterograde localization of its target mRNAs to the distal neurite. Therefore, YTHDF2 is a key reader protein that selectively protects m^{6}A-modified transcripts and localizes them to distal neurites.

3) The authors should provide a clear and comprehensive definition of the specific role of YTHDF2 in regulating mRNA, particularly distinguishing whether it primarily facilitates the degradation or transport of mRNA. Additionally, it is crucial to explain how these processes influence mRNA translation in neurons and, ultimately, how they impact neuronal function. Specifically, they should address whether YTHDF2's action is associated with enhancing mRNA localization to axons for local translation or whether it leads to mRNA degradation, resulting in reduced protein synthesis. By clarifying these mechanisms, the authors can establish a more direct link between mRNA regulation by YTHDF2 and the functional outcomes on neuronal processes such as axon guidance, synaptic plasticity, and neurodevelopment.

We appreciate the reviewer's important suggestion. According to our hypothesis, YTHDF2 recognizes m^{6}A-modified mRNAs and recruits them either to the degradation machinery or to the transport machinery, depending on the subcellular compartment. For example, YTHDF2 interacts with CNOT1, a component of the RNA degradation pathway, exclusively in the soma. In contrast, the YTHDF–FMRP interaction is prominently observed in neurites, suggesting that m^{6}A-tagged mRNAs in neurites are more likely associated with transport machinery and/or translational suppressor complexes (Revised Fig. 6b).

When comparing the proximal 50 bp regions surrounding m^{6}A sites, the major differential motif between the Q1 mRNA subset (m^{6}A-tagged mRNAs with increased stability and increased axonal localization in *M14* cKO) and the Q2 subset (m^{6}A-tagged mRNAs with increased stability but decreased axonal localization in *M14* cKO) is the FMRP-binding motif (Revised Fig. 6a). This finding suggests that FMRP binding near m^{6}A sites may switch the regulatory outcome from degradation to transport by recruiting transport machinery instead of degradation complexes. Consistent with this idea, knockdown of *Fmr1* significantly increased the interaction between

YTHDF2 and CNOT1, indicating that FMRP competitively inhibits the association of m⁶A-tagged mRNA/YTHDF2 with the degradation machinery (Revised Fig. 6d–e). In addition, immunocytochemistry analysis of growth cones revealed that the relative protein levels of ANK2, NCAM1, and ACTB were reduced upon Mettl14 depletion, whereas GAP43 showed no significant change (Extended Data Fig. 5a–b). These findings further support the idea that YTHDF2 promotes axonal mRNA localization for local translation when acting together with FMRP and other components of the transport machinery.

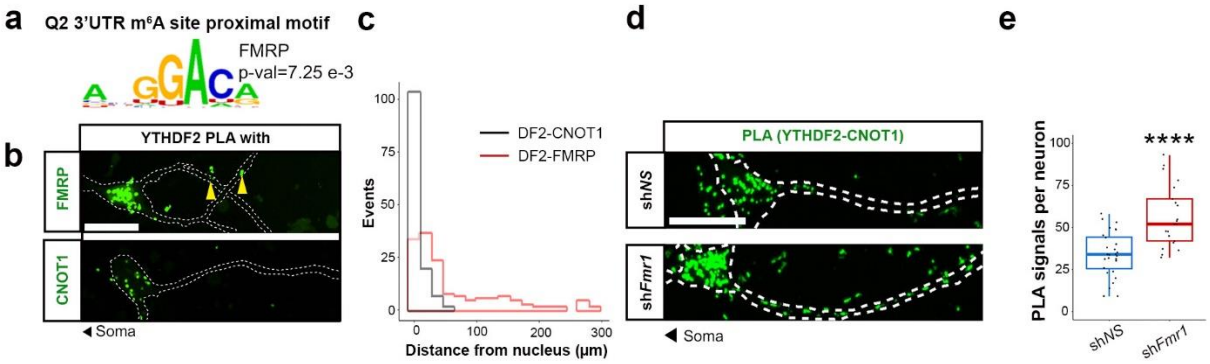

Revised Fig. 6. FMRP interacts with YTHDF2 to facilitate transport of m⁶A-tagged mRNAs to distal neurites in developing neurons.

(a) Motif enrichment analysis of the Q2 3'UTR m⁶A proximal sequence (±50 bp). **(b-c)** YTHDF2 is associated with functional cofactors in different subcellular locations. Shown in (b) are representative PLA signals (green), representing endogenous YTHDF2-CNOT1 and YTHDF2-FMRP associations (Scale bar: 20μm). The yellow arrowheads indicate PLA signals in the distal neurites. The distribution of PLA signals in neurites is quantified in (c). **(d-e)** YTHDF2-CNOT1 associations decreased in *Fmr1* KD mouse primary neurons. Shown in (d) are representative PLA signals (green) indicating endogenous YTHDF2-CNOT1 associations in control and *Fmr1* KD mouse primary neurons (Scale bar: 20μm). The number of PLA signals per neuron was quantified in (e) (Control: n = 28, *Fmr1* KD: n = 21, *P* = 9.43e-06).

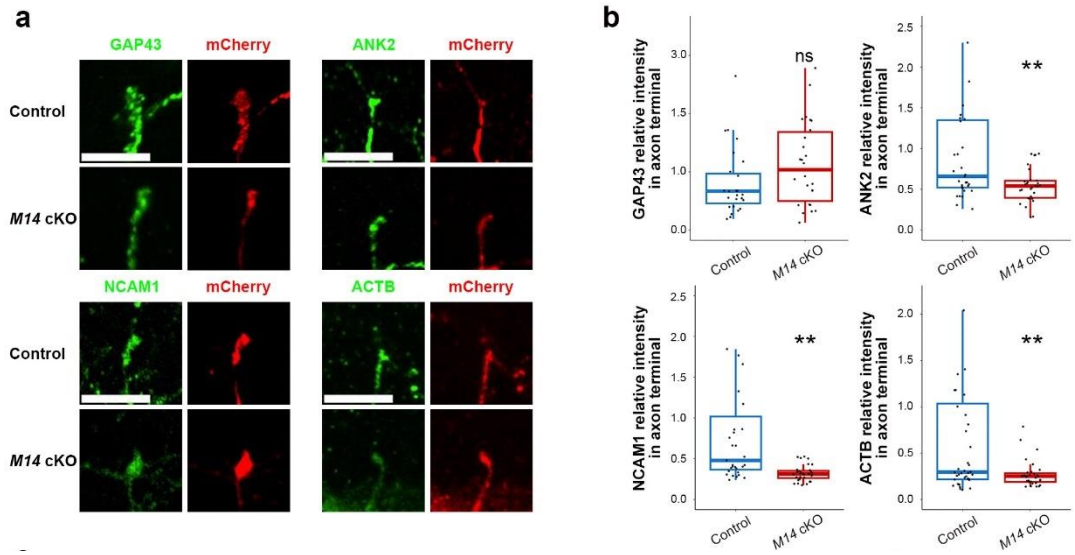

Revised Extended Data Fig. 5. Loss of *Mettl14* leads to a reduced neuronal gene expression and localization in axons. (a-b) *Mettl14* cKO reduce expression of target protein in axon terminal. Shown in (a) the target protein and mCherry ICC image (Scale bar: 10μm) and the quantification of the relative intensity was shown in (b) (GAP43: Control n=27, *Mettl14* cKO n=26, *P*=0.06521; NCAM1: Control n=31, *Mettl14* cKO n=32, *P*=0.002766; ANK2: Control n=31, *Mettl14* cKO n=30, *P*=0.004337; ACTB: Control n=40, *Mettl14* cKO n=31, *P*=0.01434).

We have already discussed this issue extensively in the second paragraph of the Discussion and have also incorporated new data into the main text, along with further explanation in the Discussion section.

Changes in the text:

(Line 237-239) Consequently, the axonal protein levels of NCAM1, ANK2, and ACTB were relatively reduced at growth cones, indicating that m^{6}A-mediated mRNA transport is essential for proper axonal expression of these target proteins (Extended Data Fig. 5 a-b).

(Line 390-396) Intriguingly, PLA signals for YTHDF2-FMRP were observed in both the soma and distal neurites, whereas signals for YTHDF2-CNOT1 were exclusively detected in the perinuclear soma (Fig. 6b-c). In addition, knockdown of Fmr1 significantly increased the interaction between YTHDF2 and CNOT1 (Fig. 6d–e). These results indicate the presence of two distinct YTHDF2-containing complexes: an RNA transport complex with FMRP and an RNA degradation complex with CNOT1, with FMRP competitively inhibiting the association of m^{6}A-tagged mRNA/YTHDF2 with the degradation machinery.

(Line 451-465) Indeed, YTHDF2 interacts both with the mRNA degradation complex, including CNOT1, and with the mRNA transport complex, including FMRP and kinesins, but in distinct subcellular compartments (Fig. 5b and Fig. 6a-c). Furthermore, FMRP inhibits the interaction of YTHDF2 with the degradation machinery (Fig. 6d-e). These results suggest that m^{6}A-tagged mRNAs are selectively recognized either by the degradation or the transport complex, with FMRP playing a pivotal role in regulating the degradation and

transport of m^{6}A-tagged mRNAs. Specifically, FMRP protects a subset of m^{6}A-tagged mRNAs from degradation by inhibiting the interaction between YTHDF2 and the degradation machinery, while simultaneously promoting their transport by enhancing the association of YTHDF2 with microtubules (Fig. 6c-d). Indeed, known FMRP target mRNAs have higher m^{6}A stoichiometry compared to FMRP non-target mRNAs (Extended Data Fig. 6a), and high m^{6}A stoichiometric mRNAs are less affected in their stability compared to low m^{6}A stoichiometric mRNAs upon Mettl14 depletion (Fig. 2g). Consistently, *Drosophila* YTHDF directly interacts with FMRP to cooperatively inhibit the translation of mRNAs involved in axonal growth regulation.

(4) The PLA (Proximity Ligation Assay) experiment, while useful for indicating proximity between YTHDF2 and its interacting proteins, does not provide sufficient evidence to confirm their co-localization or direct interaction. To strengthen the validation of these interactions, the authors should incorporate immunostaining experiments to visualize the precise subcellular localization of YTHDF2 and its interacting partners within neurons. This would provide clearer evidence of whether these proteins are truly co-localized in regions critical for mRNA transport, such as axons or growth cones. Additionally, co-immunoprecipitation (Co-IP) experiments are essential for confirming physical interactions between YTHDF2 and its binding partners at the molecular level. Co-IP would enable the authors to directly demonstrate that these proteins form a stable complex, supporting the proposed mechanism involving YTHDF2's role in mRNA transport.

We thank the reviewer for pointing out this issue, as Reviewer #1 raised a similar concern. To address this, we performed immunocytochemistry (ICC) with YTHDF2 and its interacting protein FMRP in human neurons, which revealed a clear co-localization pattern of these proteins (Reviewer Fig. 6a-b).

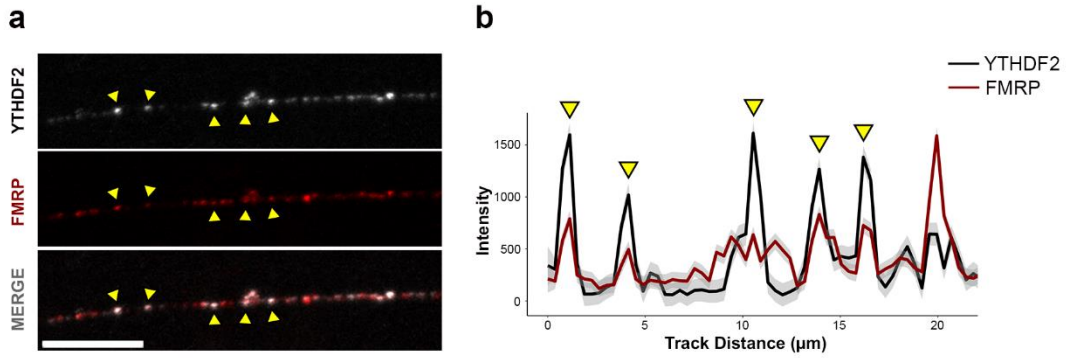

Reviewer Fig. 6. YTHDF2 colocalized with FMRP in human neuron. (a-b) YTHDF2 and FMRP granule co-localized in human neuron (yellow arrowhead). Shown in (a) the YTHDF2 and FMRP ICC image (Scale bar: 10μm) and the intensity distribution was shown in (b).

In addition, we conducted co-immunoprecipitation (Co-IP) experiments to examine the interaction between YTHDF2 and TUBB3 in P0 forebrain (Revised Fig. 5e). This experiment showed that YTHDF2 interact with TUBB3 in m^{6}A dependent manner in vivo. Add to this, to examine the transport machinery complex (YTHDF2–FMRP–KIF5C) in HEK293T and Neuro2A cells (Revised Fig. 5f, g). These experiments demonstrated direct interactions between YTHDF2 and FMRP, as

well as between YTHDF2 and KIF5C, supporting the role of YTHDF2 as a key component of the m^{6}A-tagged RNA transport machinery.

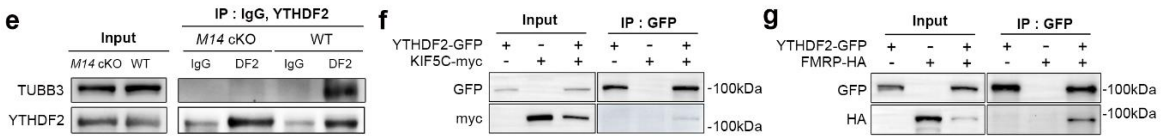

Revised Fig. 5. YTHDF2 interacts with the transport machinery and neurite microtubules in an m^{6}A-dependent manner. **(e–g)** Western blot analysis validating the LC–MS/MS results for YTHDF2 interactions. Shown in **(e)** is the interaction between TUBB3 and YTHDF2, validated by co-immunoprecipitation using an anti-YTHDF2 antibody in P0 forebrain tissue from *Mettl14* WT and cKO mice. Shown in **(f)** is the interaction between KIF5C and YTHDF2, validated by co-immunoprecipitation using an anti-GFP antibody in Neuro2A cells transfected with KIF5C-myc and YTHDF2-GFP. Shown in **(g)** is the interaction between FMRP and YTHDF2, validated by co-immunoprecipitation using an anti-GFP antibody in HEK293T cells transfected with FMRP-HA and YTHDF2-GFP.

Changes in the text:

(Line 348-357) To validate our LC-MS/MS results, we performed co-immunoprecipitation with YTHDF2, and examined the pull-down affinity of associated proteins, TUBB3, KIF5C, and FMRP (Fig 5.e-g). We performed Co-IP with anti-YTHDF2 antibody in P0 forebrain lysate of *Mettl14* WT and cKO to validate the interaction with TUBB3 (Fig. 5e). We found that TUBB3 interact with YTHDF2 with the presence of m^{6}A specifically. Also, we performed Co-IP with anti-GFP antibody to pulldown GFP fused with YTHDF2 after co-transfection with KIFC-myc and FMRP-HA in Neuro2A cells and HEK293T cells respectively (Fig 5.f-g). These experiments showed that both KIF5C and FMRP are interacting with YTHDF2 clearly. With these results, we validated that our LC-MS/MS data (Fig. 5.a-d) is well representing the interactome of YTHDF2 with m^{6}A.

5) The differential role of YTHDF2 in axon growth requires further discussion. Previous research by Zhuang et al. (Molecular Psychiatry, 2023) found that Ythdf2 ablation led to mossy fiber overgrowth, while the present study reports that Ythdf2 knockout causes axonal growth defects. This discrepancy suggests that YTHDF2 may function differently across various neuronal subtypes or brain regions, potentially due to distinct mRNA targets, protein interactions, or local signaling contexts. It would greatly strengthen the manuscript if the authors could address these contrasting findings in their discussion, exploring possible mechanisms such as cell type-specific roles, developmental timing, or differential mRNA regulatory requirements. Clarifying these aspects will help readers better understand the complex, context-dependent functions of YTHDF2 in axonal growth regulation and could guide future research on m6A modification in neural development.

We thank the reviewer for raising this important issue.

The contrasting roles of YTHDF2 in axon growth likely reflect context-dependent m^{6}A regulation across neuronal subtypes and developmental stages. Whereas Zhuang et al. (2023) reported

mossy fiber overgrowth in hippocampal neurons lacking Ythdf2, we observed impaired axonal growth in layer 2/3 cortico-cortical projection neurons.

This discrepancy may arise from differences in axonal projection length. Long-range projection neurons, such as layer 2/3 cortical neurons, require extensive mRNA transport to support growth cone navigation. In contrast, mossy fibers originating from dentate gyrus granule cells extend over much shorter distances and therefore may not rely on long-range mRNA transport.

Consistently, in *M14* cKO and *DF2* cKO primary cortical neurons, we observed increased proximal axon collaterals and transient protrusions (Fig. 1h, 1k, 4f), accompanied by reduced longest-neurite length and slower growth cone navigation (Fig. 1f–g, 1j, 4d–e). These findings suggest that YTHDF2 plays a greater role in coordinating mRNA transport and translational repression in long-range projection neurons, thereby supporting efficient growth cone progression while limiting proximal side branching. Conversely, in short-range projection neurons, YTHDF2 may function predominantly within the RNA degradation pathway, where its depletion could enhance axonal outgrowth by increasing mRNA abundance or protein synthesis in proximal neurites.

These opposing phenotypes may reflect differences in mRNA targets, cofactors, or local signaling environments that shift YTHDF2's function between promoting mRNA transport and facilitating degradation. Thus, YTHDF2 likely exerts cell-type- and stage-specific control over axonal development. Further investigation will be required to fully elucidate the molecular mechanisms underlying these differences across neuronal subtypes.

We have incorporated these explanations into the Discussion section.

Changes in the text:
(Line 466-480) Whereas the previous report showed mossy fiber overgrowth in hippocampal neurons lacking Ythdf2 [20], we observed impaired axonal growth in layer 2/3 cortico-cortical projection neurons. This discrepancy may arise from differences in axonal projection length, as long-range projection neurons require extensive mRNA transport to support growth cone navigation, whereas short mossy fibers may not depend on long-distance mRNA trafficking. Consistently, in *M14* cKO and *DF2* cKO cortical neurons, we observed increased proximal axon collaterals and transient protrusions, but reduced longest-neurite length and slower growth cone navigation (Fig. 1 and Fig. 4). These findings suggest that YTHDF2 plays a predominant role in coordinating mRNA transport and translational repression in long-range projection neurons, thereby promoting efficient growth cone advance while limiting proximal branching. In contrast, YTHDF2 may function more prominently in RNA degradation pathways in short-range projection neurons, where its loss could increase axonal growth by elevating mRNA abundance or protein synthesis in proximal neurites. Together, these observations indicate that YTHDF2 exerts cell-type-specific control over axonal development, warranting further investigation into the molecular mechanisms underlying such diversity.

(6) The title could be refined to better reflect the focus of the study. As the primary emphasis is on how the m6A reader protein, specifically YTHDF2, mediates mRNA transport and influences axon outgrowth, it would be more accurate for the title to highlight the m6A reader protein's active

role. The m6A modification serves as a marker rather than directly facilitating transport; thus, specifying YTHDF2's function would give readers a clearer understanding of the study's main findings. Adjusting the title accordingly would improve precision and help readers immediately grasp the study's central focus.

Thank you for the thoughtful suggestion. To better reflect the active role of YTHDF2, we have revised the title as follows:

The m^{6}A reader YTHDF2 cooperates with FMRP to regulate distal mRNA transport and axon outgrowth in developing neurons

This change emphasizes the functional contribution of YTHDF2 while maintaining the overall focus of the study.

Minor comments:
1) In Line 157, the statement "We identified 10,304 m6A sites in 3,830 genes (Fig. 2h, Extended Data Fig. 2j)" lacks alignment with Figure 2h, as no relevant information appears in this figure panel.

We apologize for the misplaced figure citations in the text. We have removed the incorrect reference and placed it in the appropriate position as follows:

Changes in the text:
(Line 191-195) Altogether, these results support that m^{6}A-tagged transcripts are directly related to neurodevelopmental processes and axon development in the postnatal brain, which are dysregulated in the *M14* cKO neurons by increased mRNA stability. Of note, the results of m^{6}A-SAC-seq and mRNA stability assay imply that high m^{6}A stoichiometry transcripts related to axon development (Fig. 2h, Extended Data Fig. 3e)

2) In Figure 1f, the method used to define neuron morphology is unclear. The high density of neurons in the image makes it difficult to clearly trace the entire morphology of individual neurons. This could lead to ambiguity in interpreting the results.

We appreciate the reviewer's suggestion, which was also raised by Reviewer #1. We agree that tracing the complete morphology of individual neurons can be challenging under high-density culture conditions. However, reducing seeding density (0.1x10^6 / per 24 well) in primary neuronal cultures may alter neuronal morphology, growth rate, and maturation. Therefore, we maintained the culture conditions described in the Methods section to ensure reproducibility across experiments.

We confirm that only neurites with clearly identifiable somatic origins and termini were measured. All neurite tracing was performed using the NeuronJ plugin in ImageJ software. To improve clarity, we have revised the Methods section as follows:

Changes in the text:

(Line 821-823) For tracking in vitro primary neuron samples, the Fiji plugin NeuronJ was used. The neurite length was measured by as the distance between a clearly identifiable neurite tip and the center of the nucleus along axonal tracks labeled with Tau.

Furthermore, we have replaced the previous Fig. 1f with a Tau immunocytochemistry image to better represent axonal structures, as suggested by Reviewer #1. The corresponding quantification has been re-evaluated using Tau staining data (Revised Fig. 1f-j).

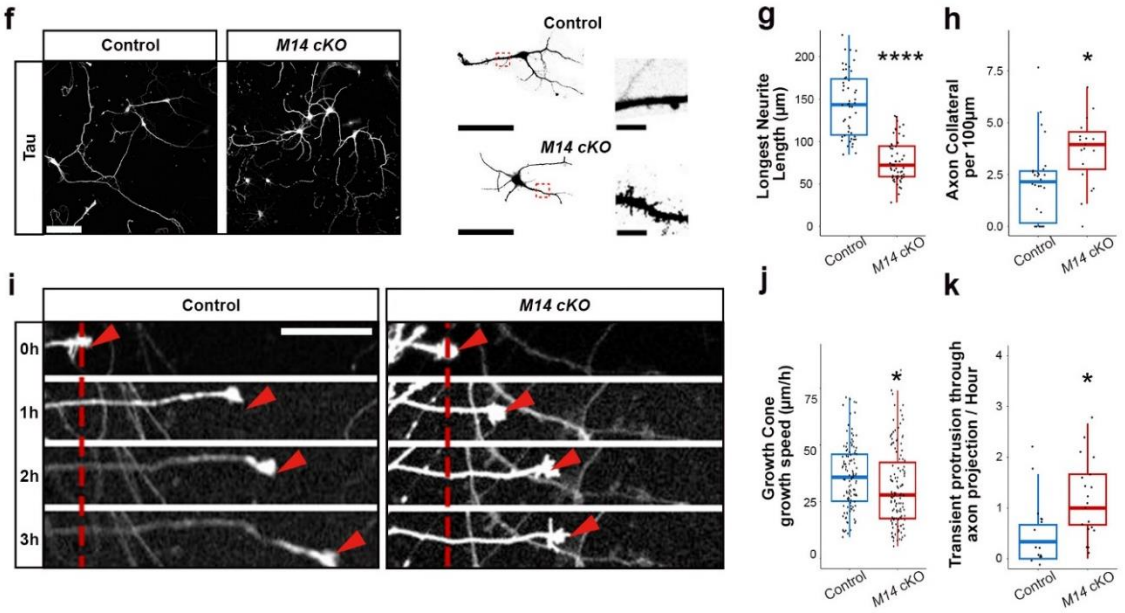

Revised Fig. 1. *Mettl14* deletion during corticogenesis leads to reduced axon projection, shorter neurite length, increased axon collaterals, and slower growth cone dynamics. **(f-j)** M14 cKO primary neuron exhibited abnormal neurite growth at DIV6. Shown in **(f)** are representative confocal images and skeletal images (scale bars: 100 μm). The right panels show enlarged area of squared skeletal images (scale bars: 10um). Neurite length and collateral branching frequency were quantified in **(g)** (Control n=50, M14 cKO n=56; P < 2.2e-16) and **(h)** (Control n= 30, M14 cKO n=19; P=0.03536). Values represent mean ± SEM. **(i)** Live imaging of growth cones in control and M14 cKO neurons over 3 hours at DIV6. Red arrowheads indicate the locations of growth cones (scale bar: 20 μm). Shown in **(j)** is the quantification of total growth length divided by tracking time. Values represent mean ± SEM (Control n=114, M14 cKO n=134; P=0.02441) and **(k)** is the quantification of the transient protrusion (Control n=15, *M14* cKO n=19, *P*=0.01692) Significance was evaluated using two-tailed unpaired Student's t-tests (c, d, g, h, and j). The significance of RFP intensity across the midline was evaluated using two-way ANOVA (b). *P < 0.05, **P < 0.01, ****P < 0.0001.

3) In Figure 1g, the text describes the "total length of neurites," but the panel itself shows the "longest neurite." This discrepancy should be addressed for consistency.

We appreciate the reviewer's suggestion. As recommended, we performed immunocytochemistry using the axonal marker Tau and measured the longest axon (Fig. 1f, g). We have incorporated

the following correction in the revised manuscript:

Changes in the text:

(Line 137-139) We observed a significant reduction in the longest neurite length of M14 cKO neurons and an increase in axon collateral branching compared to that of control neurons at DIV6 (Fig. 1f-h)

(4) In Figure 3e, the position of the soma should be clearly marked to provide context for the measurements and observations related to neurite outgrowth. This is important for understanding the spatial distribution of neurites and the directionality of growth. The same clarification should be applied to the other figures where soma position is relevant but not explicitly indicated.

We appreciate the reviewer's suggestion. We have marked the "soma direction" with a triangle symbol in the smFISH (Revised Fig. 3e, 4i, 6j, Revised Extended Data Fig. 5c, 6l), PLA (Revised Fig. 5h, k, n, 6b, d, f, h, m, Revised Extended Data Fig 8d, f), and RNA live images (Fig. 3i, l, 4l).

(5) In Figure 3g, the live imaging of lysosomes would benefit from labeling the direction of the soma and the distal axon.

We appreciate the reviewer's suggestion, which was also raised by Reviewer #1. We have updated our lysosome live-imaging data to include the "soma direction" marker (Extended Revised Data Fig. 5e-h)

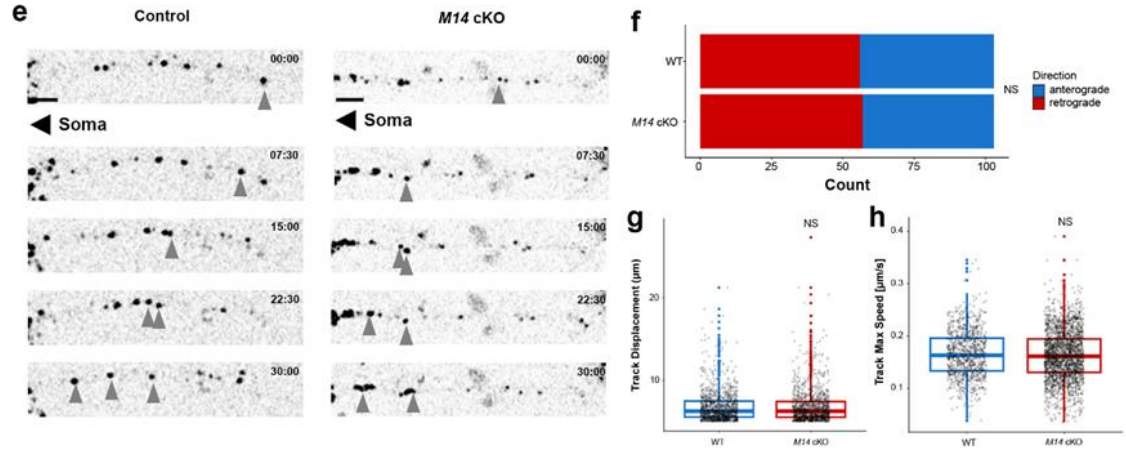

Extended Data Fig. 5. Loss of *Mettl14* leads to a reduced neuronal gene expression and localization in axons.

(**e-h**) Live imaging of lysosomes in *M14* cKO and control cortical neurons at DIV6. Shown in (e) is a time-lapse image representing lysosome dynamics over 30 minutes (scale bars: 10 μm). Direction of lysosome movement is counted in two categories, anterograde and retrograde, and validated in (f) (Control n=103, *M14* cKO n=103, *P*=0.1573). Lysosome track displacement length is quantified in (g) (Control n=1130, *M14* cKO n=1195, *P*=0.5133), and lysosome track max speed is quantified in (h) (Control n=1130, *M14* cKO n=1195, *P*=0.1509). Significance was evaluated using two-tailed unpaired Student's t-tests (b, d, g, h), and Pearson's Chi-squared test (f). ns, not significant; **P* < 0.05, ***P* < 0.01.

(6) In Figure 5b, the interaction between YTHDF2 and its associated proteins should be validated through additional biochemical experiments, such as co-immunoprecipitation (Co-IP), particularly for FMR1 and TUBB3.

As described above, we performed co-immunoprecipitation (Co-IP) of FMRP and KIF5C to confirm their physical interactions with YTHDF2 (Revised Fig. 5f, g). In addition, as the reviewer suggested, the interaction between YTHDF2 and TUBB3 was further confirmed in the mouse P0 forebrain (revised Fig. 5e).

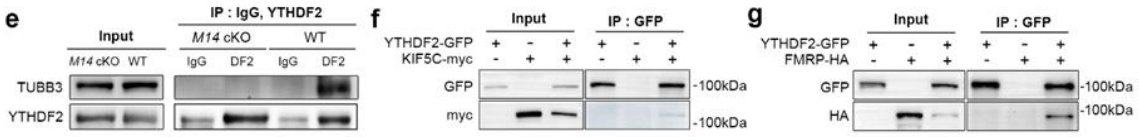

Revised Fig. 5. YTHDF2 cooperates with the transport machinery in an m^{6}A-dependent manner while still interacting with the RNA degradation machinery.
(e-g) Western blot analysis for validation of LC-MS/MS result with YTHDF2. Shown in (e) is interaction between TUBB3 and YTHDF2 validated with co-immunoprecipitation with anti-YTHDF2 antibody in P0 forebrain in *Mettl14* WT and cKO. Shown in (f) is interaction between KIF5C and YTHDF2 validated with co-immunoprecipitation with anti-GFP antibody in Neuro2A cells transfected with KIF5C-myc and YTHDF2-GFP. Shown in (g) is interaction between FMRP and YTDHF2 validated with co-immunoprecipitation with anti-GFP antibody in HEK293T cells transfected with FMRP-HA and YTHDF2-GFP.

Changes in the text:
(Line 348-357) To validate our LC-MS/MS results, we performed co-immunoprecipitation with YTHDF2, and examined the pull-down affinity of associated proteins, TUBB3, KIF5C, and FMRP (Fig 5.e-g). We performed Co-IP with anti-YTHDF2 antibody in P0 forebrain lysate of *Mettl14* WT and cKO to validate the interaction with TUBB3 (Fig. 5e). We found that TUBB3 interact with YTHDF2 with the presence of m^{6}A specifically. Also, we performed Co-IP with anti-GFP antibody to pulldown GFP fused with YTHDF2 after co-transfection with KIFC-myc and FMRP-HA in Neuro2A cells and HEK293T cells respectively (Fig 5.f-g). These experiments showed that both KIF5C and FMRP are interacting with YTHDF2 clearly. With these results, we validated that our LC-MS/MS data (Fig. 5.a-d) is well representing the interactome of YTHDF2 with m^{6}A.

(7) The study suggests that the knockout of YTHDF2 leads to decreased mRNA transport; however, this finding should be further validated using quantitative PCR (qPCR) from compartmentalized neuron cultures by analyzing mRNA levels in distinct neuronal compartments, such as the soma and axons.

We appreciate the reviewer's suggestion. To address this, we performed CC-seq in *Ythdf2* cKO mice. The Ythdf2 CC-seq data revealed a transcriptional profile comparable to that observed in the Mettl14 cKO CC-seq (Reviewer Fig. 1a). We identified 565 m^{6}A-modified genes enriched among the downregulated genes, while 237 m^{6}A-modified genes were enriched among the upregulated genes. This data indicates that YTHDF2 depletion reduces the localization of m^{6}A-modified mRNAs to distal axons.

Furthermore, GO and GSEA analyses showed that downregulated genes were significantly associated with synapse organization and axonogenesis, whereas upregulated genes were linked to housekeeping processes such as cell division and chromosome organization (Reviewer Fig. 1b-d). These results confirm our original conclusion that YTHDF2 acts as the key m^{6}A reader responsible for transporting m^{6}A-tagged transcripts to axons.

We respectfully request that we intend to use the CC-seq dataset from *Ythdf2* cKO mice in a separate ongoing study. Therefore, we prepared this figure exclusively for reviewer evaluation to address the current question, but have not included it in the revised manuscript.

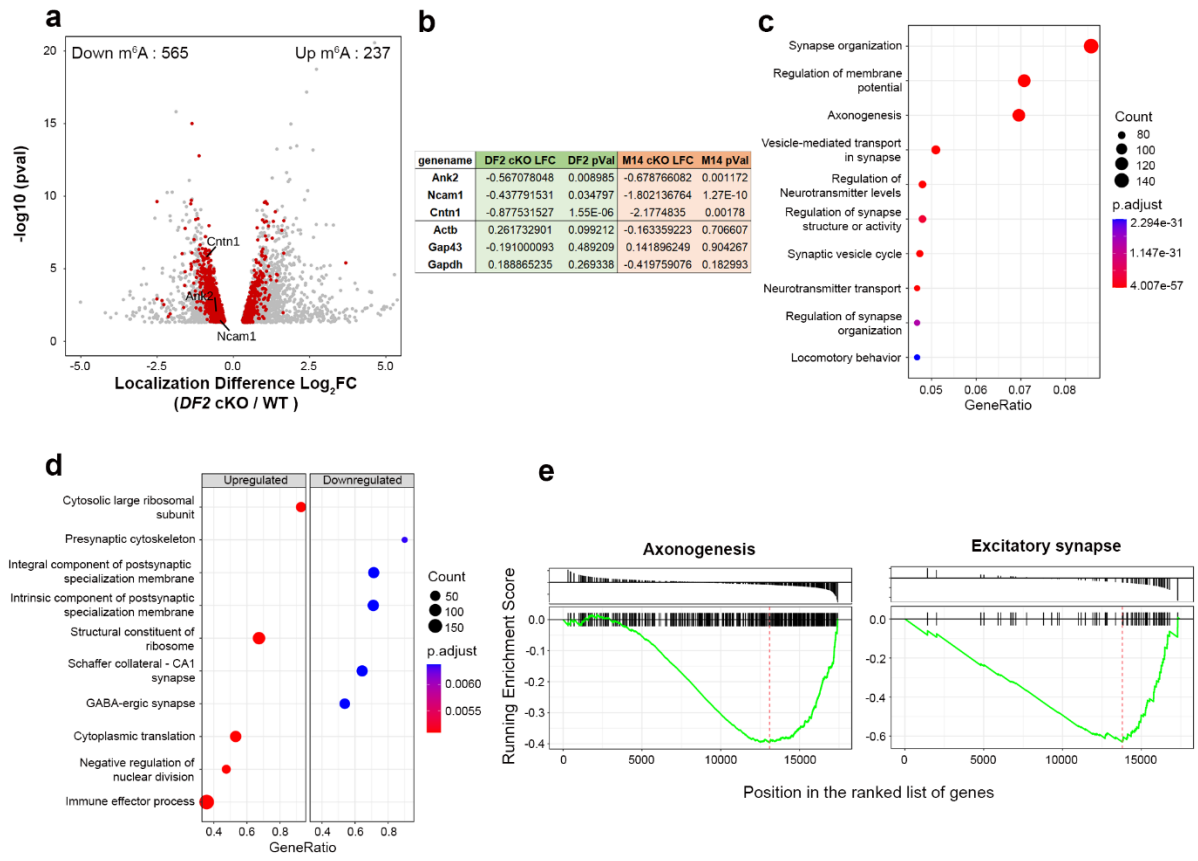

Reviewer Fig. 1. The *DF2* cKO CC-seq data revealed a transcriptional profile comparable to that observed in the *M14* cKO CC-seq

(a) The volcano plot shows genes that are depleted and enriched in the corpus callosum of P4 *DF2* cKO mice. Red indicates m^{6}A-modified genes and targets of interest are highlighted. **(b)** The table summary of *DF2* cKO CCseq and *Mettl14* cKO CCseq result of the target RNAs. **(c)** Gene Ontology analysis of downregulated DEGs. **(d-e)** Gene Set Enrichment Analysis (GSEA) for the position in the DEG fraction ranked genes. The summary dot plot for the position in the DEG ranked genes were represent on (d) and specific term were represented on (e).

Reviewer #3 (Remarks to the Author):

In this manuscript, Koo and colleagues explore the roles of m6A RNA methylation and the YTHDF2 proteins in axonogenesis and brain development. They make several claims, most of which are well substantiated by their date. They first use a Mettl14 KO paradigm to show that loss of M14 leads to a reduction in the number of axon projections and arborization in vivo and to reduce growth cones dynamics in vitro. To gain further insights in the role of m6A in these processes, m6A-SAC-seq is then used to map and quantify m6A in the forebrain of mice pups. This analysis reveals that that m6A is enriched in 3'UTRs of mRNAs coding for proteins with known localization and functions in axons and dendrites. Surprisingly, high m6A stoichiometry RNAs are less stabilized than low stoichiometry RNA in M14 cKO. Through the sequencing of RNAs extracted from the corpus callosum (CC-seq), RNAs dependent on m6A for their localization are identified and validated using FISH in primary neurons. The authors then repeat some of these experiments using YTHDF2 cKO mice, finding similar effects on axon growth and guidance. Overall, these finding convincingly shows that m6A and YTHDF2 may have functions beyond the control of mRNA stability in neurons (localization), corroborating evidence found in other neuronal systems. The authors next performed an IP-MS experiments to explore the mechanisms by which YTHDF2 and m6A contribute to axonogenesis. They identify 283 proteins with reduced interactions in M14 cKO mice, notably KIF5C, TUBB2B, TUBB3, MAP2, in addition to RBPs FXR1, FMR1 and FUS. Some of these interactions are then confirmed using proximity ligation assays in cultured neurons. Overall, I find that the last two figures are weaker than the first 4. Nonetheless, the data presented are novel and addresses an interesting and important topic that remains debated in the field. As such I think that a large audience would show interest in this paper. However, I have some minor comments that should be addressed before publication in order to improve the quality of the manuscript:

We appreciate the reviewer's thoughtful summary and constructive feedback. Below, we address all comments in detail.

Minor points

1) m6A-SAC-seq: m6A-SAC-seq is a recently developed method for the profiling of m6A. The data is interesting and the overlap with other existing datasets is reassuring. However, I found that the details provided in method sections were lacking. The authors should specify the number of biological replicates (This was only found in the GEO dataset). Moreover, it is unclear how replicable this approach is. Are all identified sites found in both biological replicates? Overall, more details would help the readers to understand and replicate these experiments if needed.

We appreciate the reviewer's suggestion, which was also raised by Reviewer #1. In response, we have added the number of replicates in the Results section (Lines 150–153). We used two biological replicates for each WT and M14 cKO. In addition, we have clarified the criteria used to define final m^{6}A peaks in the Methods section (see below). Specifically, we revised several sentences for clarity and included a GitHub link for easier understanding of the analysis workflow.

Furthermore, we have added a demonstration of m^{6}A-SAC-seq scheme and quality validation in the Revised Extended Data Fig. 2a-b.

(Line 150-153) To identify METTL14-dependent m^{6}A sites, we filtered out peaks according to the previous protocol [20], using m^{6}A-SAC-seq data from WT forebrain and *M14* cKO forebrain with 2 biological replicates for each (Extended Data Fig. 2b).

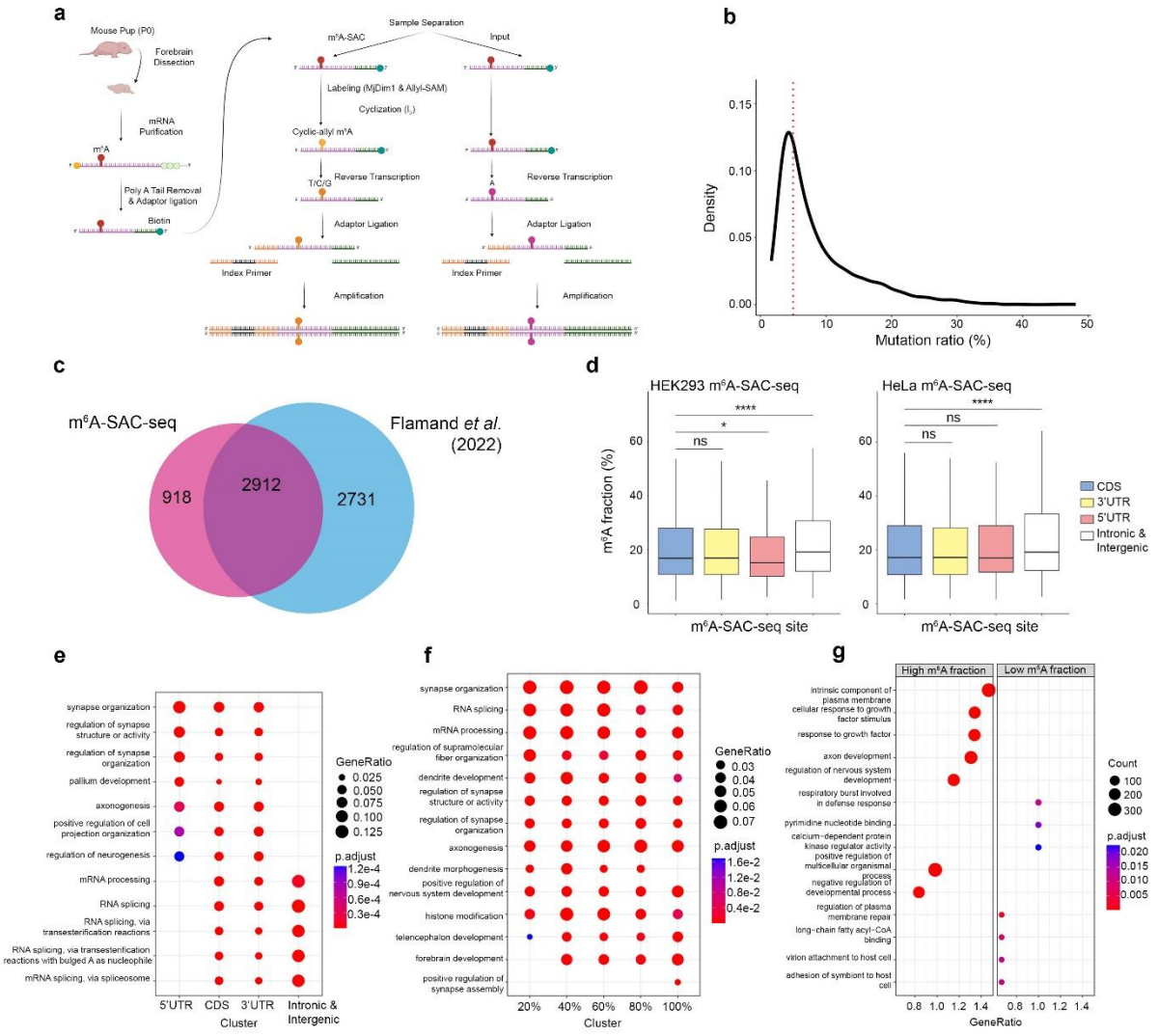

Revised Extended Data Fig. 2. Unique characteristics of single base-pair resolution m^{6}A map in the developing brain through m^{6}A-SAC-seq. **(a)** Schematic of m^{6}A-SAC-seq performed on P0 mouse forebrain samples from WT and Nestin-Cre Mettl14 cKO mice. **(b)** Density plot showing the distribution of mutation ratios based on m^{6}A-SAC-seq. **(c)** Venn diagram comparing the m^{6}A-SAC-seq and DART-seq results. **(d)** The m^{6}A stoichiometry in different RNA regions, including the 3'UTR, CDS, 5'UTR, intronic, and intergenic regions. The boxplot represents differences compared with the CDS. (HEK293 CDS n=5911, 3'UTR n=4710, 5'UTR n= 328, Intronic & Intergenic n=717; HEK293 CDS compared with: 3'UTR *P* = 0.8894, 5'UTR *P* = 0.04083, Intronic & Intergenic *P* = 4.65e-06) (HeLa CDS n=4933, 3'UTR n=4731, 5'UTR n= 200, Intronic & Intergenic n=547; HeLa CDS compared with: 3'UTR *P* = 0.6093, 5'UTR *P* = 0.7014, Intronic & Intergenic *P* = 8.13e-07). **(e)** Gene Ontology analysis of RNA depending on the position of m^{6}A modifications. **(f)** Gene Ontology analysis of RNA depending on m^{6}A stoichiometry. **(g)** Gene set enrichment analysis (GSEA) summary dot plot for the position in the m^{6}A fraction ranked genes. Significance was evaluated using two-tailed

unpaired Student's t-tests (d). ns, not significant; *$P < 0.05$, **$P < 0.01$, ****$P < 0.0001$.

Changes in the text:
(Line 806-810) Following criteria is applied to identify appropriate site; Average mutation ratio of the untreated input libraries should be less then 2.5% or the maximum number of mutations is 1, average mutation ratio of the treated libraries should be more than 5%, There should be 3 or more mutations in the treated libraries, The minimum sequencing depth of all the libraries should be more than 20.

2) At line 157, the authors indicate: "m6A peaks". I think this should be replaced with "sites" since m6A-SAC-seq has single-nucleotide resolution.

Thank you for catching this error. We have made the correction as follows:

Changes in the text:

(Line 150-152) To identify METTL14-dependent m^{6}A sites, we filtered out peaks according to the previous protocol

(Line 153-155) We identified 10,304 m^{6}A sites in 3,830 genes, which showed enrichment at the DRACH motif and a stop codon-proximal 3'UTR distribution, consistent with previous reports (Fig. 2a-b, Supplementary Table 1).

3) RNA stability assays: RNA stability cannot be determined using only two points on a curve as RNA decay is not linear. At line 185, the author could change calculate to estimate.

Thank you for your suggestion. We modified the text as suggested.

Also, we performed qPCR for RNA stability assays at 3 time points after Actinomycin treatment: 0 hours, 3 hours, and 6 hours. We calculated the half-lives of our target RNAs, and the results are as follows.

Gene	Genotype	k value	Estimated half life [Hour]
Ncam1	Control	-0.036	19.2540883
	M14cKO	-0.0126	55.011681
Ank2	Control	-0.0417	16.6222345
	M14cKO	-0.0209	33.1649369
c-jun	Control	-0.1353	5.12303903
	M14cKO	-0.1134	6.112409
Ubc	Control	-0.1465	4.73138007
	M14cKO	-0.1336	5.1882274

As shown in the table, our target *Ncam1* and *Ank2* showed increased half-lives when Mettl14 was depleted, as indicated by our RNA-seq-based RNA stability estimation data. Compared

to this, control targets such as *c-jun* and *Ubc* half-lives showed no significant effect on *Mettl14*. Through this, our RNA-seq-based RNA stability estimation data are validated against qPCR-based estimates at three time points.

Changes in the text:
(Line 177-179) As previously described, cultured primary cortical neurons from WT and *M14* cKO mice were treated with Actinomycin D, and RNA-seq was performed at 0 and 5 hours to estimate the RNA stability of each transcript.

(Line 841-844) Significantly localized transcripts were identified by Log2foldchange > |0.5|, and p-adjust value <0.05. On stability assay, relative stability difference was estimated by [5hr Log2foldchange – 0hr Log2foldchange]

4) Figures 3b, 3c and 3d are called before figure 3a in the text.

Thank you for catching this error. We have made the correction as below:

Changes in the text:
(Line 210-211) As a result, we identified 1,864 decreased transcripts and 1,761 increased transcripts in the CC of M14 cKO compared to that of WT (Fig. 3a, Supplementary Table 2).

5) CC-seq: Extracting the exact same regions in all 3 biological replicates may be challenging. Moreover, I expect that glial cells residing in the CC will also be extracted. What fraction of the RNAs extracted is expected to come from axons in these samples? A filtering step to remove RNAs abundant in glia would be useful. For example, see Cajigas et al., Neuron 2013, who did such an analysis for the hippocampal neuropil.

We appreciate the reviewer's suggestion. We performed a Pearson correlation analysis on our sequencing datasets using deepTools and confirmed that all three biological replicates show strong reproducibility across samples (Reviewer Fig. 7a).

We agree that glial cells in the corpus callosum could potentially interfere with the CC-seq results. We already applied a similar approach, as shown in (Fig. 4D), in combination with a recently published database to further refine our target list[21].

We also followed the filtering strategy described by Cajigas et al., *Neuron* (2013) to remove transcripts derived from glial cells, blood vessels, and mitochondria. While Gap43, Ank2, and Actb remained after filtering, our target Ncam1 and Cntn1 filtered out because of they are categorized as astrocyte/oligodendrocyte expressing transcripts.

Instead of using outdated microarray driven non-neuronal gene list, we applied the latest Single nucleus spatial transcriptomic atlas to filter out non-neuronal transcripts in CC[22]. We filter out our sequencing data using "Fibertract" categorized geneset which include oligodendrocyte, vascular cell, astrocyte, ventricular cell, and microglia (Reviewer Fig. 7b). Among the 3456 DEG, only 86 genes were overlapped. However, one of our target *Ncam1* expressed in olfactory bulb and filtered out in this strategy.

Finally, we isolate representative genes in cell nucleus spatial transcriptome T44~T74 section, the region that CC-seq RNA sampled. (Reviewer Fig. 7c) We identify 684 region specific non-neuronal genes and only 41 genes were overlapped with our CC-seq result.
Altogether, we conclude that our CC-seq has sufficient reproducibility within samples, and the filtering step to remove glial RNA does not affect to our result using previous selection step using neuronal genes (Fig. 4D).

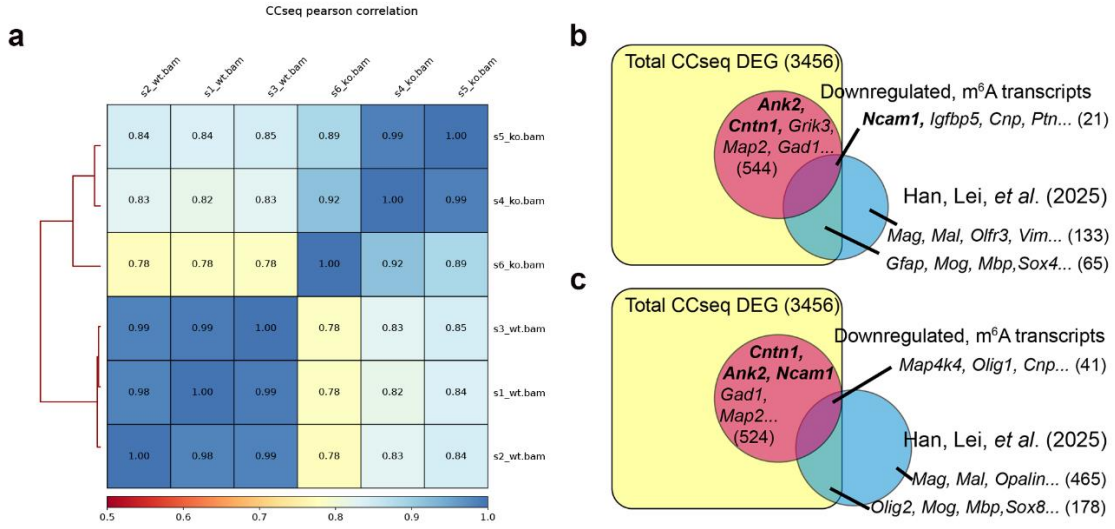

Reviewer Fig. 7. The quality check of CC-seq. (a) Pearson correlation plot of the CC-seq datasets. The WT and *M14* cKO samples cluster closely and shows high correlation. **(b)** Venn diagram comparing the CC-seq datasets and non-neuronal geneset. **(c)** Venn diagram comparing the CC-seq datasets and corpus callosum area (T44-T74) spatial transcriptome.

6) Mass spectrometry: How many biological replicates were performed? Is the data deposited? Additional details on these samples should be provided. Since the authors indicate enrichment and depletion of in M14 cKO, this information is important, and these experiments should be performed in multiple replicates. Otherwise, the results could be caused by changes in the negative IgG control.

For our main figures, we initially used one biological replicate (a lysate from three WT brains for LC–MS/MS analysis, and the corresponding data are included in the Supplementary Table. In addition, we have now performed new LC–MS/MS experiments using three independent biological replicates to validate our previous findings (Reviewer Figure 8. We found that most of our main targets, such as FMRP, IGF2BP1, and TUBB3, were consistently detected across the new datasets. However, due to the inherent variability of LC–MS/MS experiments, not all interaction results were fully conserved. We provide a reviewer-only figure summarizing these additional LC–MS/MS data. Furthermore, we confirmed LC-MS/MS results using co-immunoprecipitation followed by Western blotting (Co-IP–WB) to further confirm these interactions (Revised Fig. 5e-g).

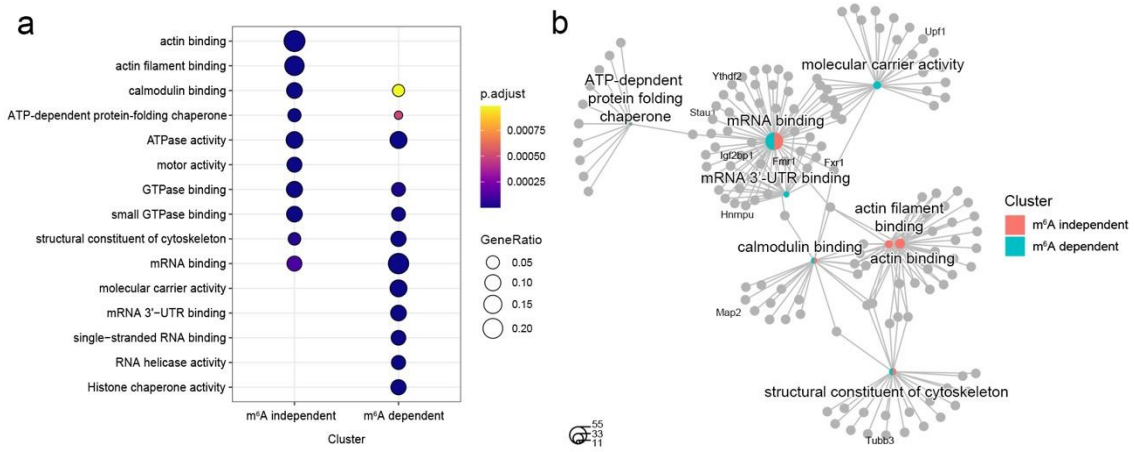

Reviewer Fig 8. Reconducted LC-MS/MS for YTHDF2 Co-IP LC-MS/MS in the P0 mouse forebrain for WT and *M14*cKO

(a) Gene ontology analysis for LC-MS/MS based YTHDF2 interactome with comparing m^{6}A presence with compareCluster analysis (b) Gene concept network analysis of for LC-MS/MS based YTHDF2 interactome with comparing m^{6}A presence

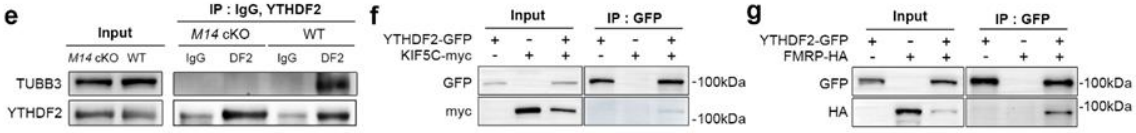

Revised Fig. 5. YTHDF2 cooperates with the transport machinery in an m^{6}A-dependent manner while still interacting with the RNA degradation machinery.

(e-g) Western blot analysis for validation of LC-MS/MS result with YTHDF2. Shown in (e) is interaction between TUBB3 and YTHDF2 validated with co-immunoprecipitation with anti-YTHDF2 antibody in P0 forebrain in *Mettl14* WT and cKO. Shown in (f) is interaction between KIF5C and YTHDF2 validated with co-immunoprecipitation with anti-GFP antibody in Neuro2A cells transfected with KIF5C-myc and YTHDF2-GFP. Shown in (g) is interaction between FMRP and YTDHF2 validated with co-immunoprecipitation with anti-GFP antibody in HEK293T cells transfected with FMRP-HA and YTHDF2-GFP.

Changes in the text:

(Line 348-357) To validate our LC-MS/MS results, we performed co-immunoprecipitation with YTHDF2, and examined the pull-down affinity of associated proteins, TUBB3, KIF5C, and FMRP (Fig 5.e-g). We performed Co-IP with anti-YTHDF2 antibody in P0 forebrain lysate of *Mettl14* WT and cKO to validate the interaction with TUBB3 (Fig. 5e). We found that TUBB3 interact with YTHDF2 with the presence of m^{6}A specifically. Also, we performed Co-IP with anti-GFP antibody to pulldown GFP fused with YTHDF2 after co-transfection with KIFC-myc and FMRP-HA in Neuro2A cells and HEK293T cells respectively (Fig 5.f-g). These experiments showed that both KIF5C and FMRP are interacting with YTHDF2 clearly. With these results, we validated that our LC-MS/MS data (Fig. 5.a-d) is well representing the interactome of YTHDF2 with m^{6}A.

7) smFISH: a linear map of targeted RNAs and their mapped m6A sites should be provided in

supplements. This would help the reader to assess the number of sites and the stoichiometry of m6A on targets which require m6A for their localization.

We appreciate the reviewer's suggestion. We have already demonstrated the m^{6}A sites and stoichiometry of the target RNAs within the 3′ UTR region in Fig. 2h. In addition, we have now included Gap43 and Camk2b in the revised Extended Data Fig. 2i. For clarity, we have added the relevant figure citation as follows:

Changes in the text:
(Line 230-233) To investigate whether m^{6}A tagging plays a role in the localization of our target transcripts during neuronal differentiation, we performed single-molecule *in situ* hybridization (smFISH) to visualize endogenous *Gap43*, *Camk2b*, *Ncam1*, *Cntn1*, *Ank2*, and *Actb* mRNAs (Fig. 2h and Extended Data Fig. 3e) in control and *M14* cKO conditions (Fig. 3e).

8) It is unclear what is being quantified in fig 4i, 5f, 5g, 6e, 6g, 6i. Are these observations for all mRNA/PLA signals across all cells in all biological replicate? It would be better to also present the data in individual experiments and cell to assess the variability between each cell.

We appreciate the reviewer's suggestion, which was also raised by Reviewer #1. We agree that measuring single mRNA or PLA signals across all cells is not sufficient to fully demonstrate RNA localization or protein interactions. To address this, we have added normalized density plots reflecting the ratio of smFISH signals in neurites versus total cells for each individual cell, thereby illustrating variability across individual axons (Revised Figs. 3f, 3h, 4i, 5f, 5h, 6g, and 6i). We also added a detailed description of how the normalized density plots were generated in the Methods section.

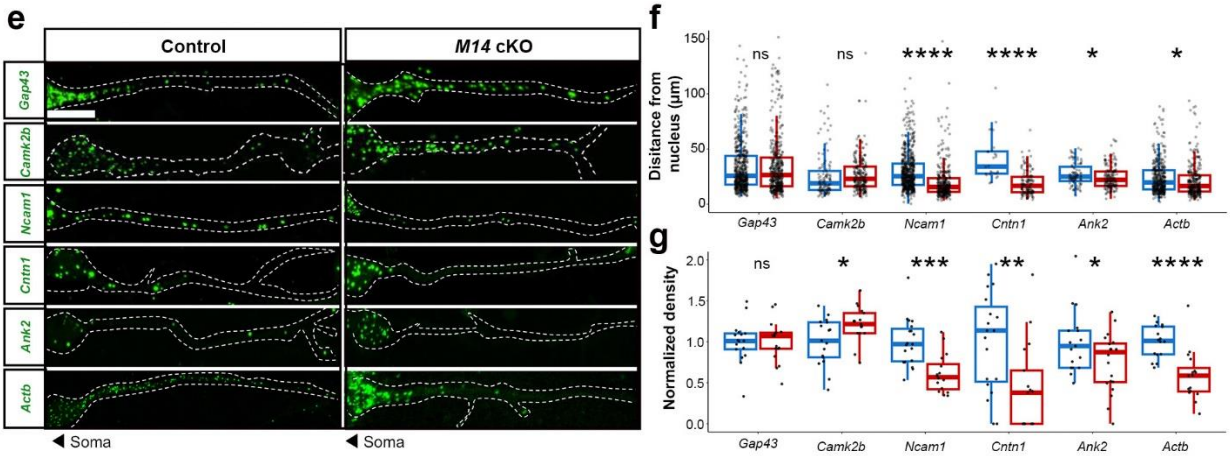

Revised Fig.3 m^{6}A modification is crucial for the distal translocation of cytoskeletal mRNAs in differentiating neurons. (e-g) *M14* cKO primary cultured neurons show depleted RNA localization. Shown in (e) are representative smFISH signals (green) representing endogenous *Gap43*, *Camk2b*, *Ncam1*, *Cntn1*, *Ank2*, and *Actb* (scale bars: 20 μm). The distance from the nucleus is quantified in (f) (*Gap43*: Control n=568, *M14* cKO n=460; *P*=0.6987, *Camk2b*: Control n=113, *M14* cKO n=238; *P*=0.6099, *Ncam1*: Control n=609, *M14* cKO n=343; *P* ≤ 2.2e-16, *Cntn1*: Control n=28, *M14* cKO n=137; *P*=1.46e-14, *Ank2*: Control n=90, *M14* cKO n=164; *P*=0.02853, *Actb*: Control n=397, *M14* cKO n=294; *P*=0.01343), and

the relative density of smFISH puncta in neurites compared to the total is quantified in (g) (*Gap43*: Control n=17, *M14* cKO n=17; *P*=0.9671, *Camk2b*: Control n=17, *M14* cKO n=17; *P*=0.01711, *Ncam1*: Control n=19, *M14* cKO n=16; *P*=0.0001537, *Cntn1*: Control n=19, *M14* cKO n=17; *P*=0.005298, *Ank2*: Control n=17, *M14* cKO n=20; *P*=0.04917, *Actb*: Control n=16, *M14* cKO n=16; *P*=9.801e-05).

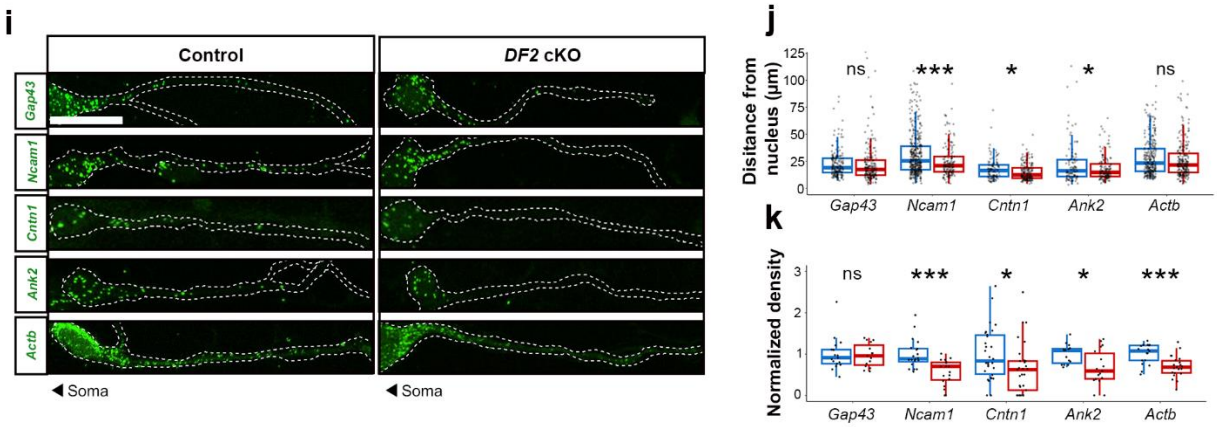

Revised Fig. 4. *Ythdf2* deletion reduces axonal projection and neurite length and impairs growth cone dynamics in *DF2* cKO.(i-k) *DF2* cKO primary cultured neuron showed reduced distal RNA localization. Shown in (i) are representative smFISH signals (Green) representing endogenous *Gap43, Ncam1, Cntn1, Ank2, Actb* (Scale bars: 20 μm). The distance from the nucleus was quantified in (j) (*Gap43* Control n=178, *DF2* cKO n=194; *P*=0.8605, *Ncam1*: Control n=383, *DF2* cKO n=157; *P*=0.0007246, *Cntn1*: Control n=106, *DF2* cKO n=165; *P*= 0.01605, *Ank2*: Control n=102, *DF2* cKO n=140; *P*= 0.02627, *Actb*: Control n=264, *DF2* cKO n= 231; *P*=0.1793) and the relative density of smFISH puncta in neurites compared to the total is quantified in (k) (*Gap43*: Control n=15, *DF2* cKO n=17; *P*= 0.8093, *Ncam1*: Control n=19, *DF2* cKO n=20; *P*=0.0002398, *Cntn1*: Control n=29, *DF2* cKO n=30; *P*=0.03339, *Ank2*: Control n=18, *DF2* cKO n=15; *P*=0.01088, *Actb*: Control n=22, *DF2* cKO n=17; *P*=0.0007279).

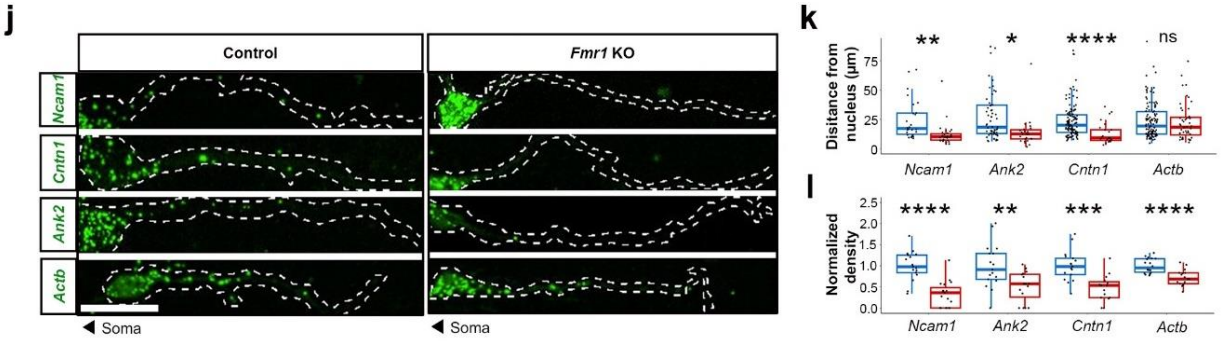

Revised Fig.6. FMRP interacts with YTHDF2 to assist m^{6}A-tagged mRNA transport to distal neurites of developing neurons. (j-l) RNA localization to neurites decreased in *Fmr1* KO mouse primary neurons. Shown in (j) are representative smFISH signals (green)

representing endogenous *Ncam1*, *Cntn1*, *Ank2*, and *Actb* in control and *Fmr1* KO conditions (Scale bar: 20μm). The distance from the nucleus was quantified in (k) (*Ncam1*: Control n = 26, *Fmr1* KO n = 33; *P* = 0.0005381. *Cntn1*: Control n = 62, *Fmr1* KO n = 27; *P* = 0.04902. *Ank2*: Control n = 125, *Fmr1* KO n = 25; *P* = 0.0005668. *Actb*: Control n = 123, *Fmr1* KO n = 48; *P* = 0.6665) and the relative density of smFISH puncta in neurites compared to the total is quantified in (l) (*Ncam1*: Control n=17, *FMRP* cKO n=19; *P*=, 4.408e-07 *Cntn1*: Control n=17, *FMRP* cKO n=16; *P*=0.003859, *Ank2*: Control n=17, *FMRP* cKO n=15; *P*=0.0001217, *Actb*: Control n=18, *FMRP* cKO n=17; *P*=5.784e-05).

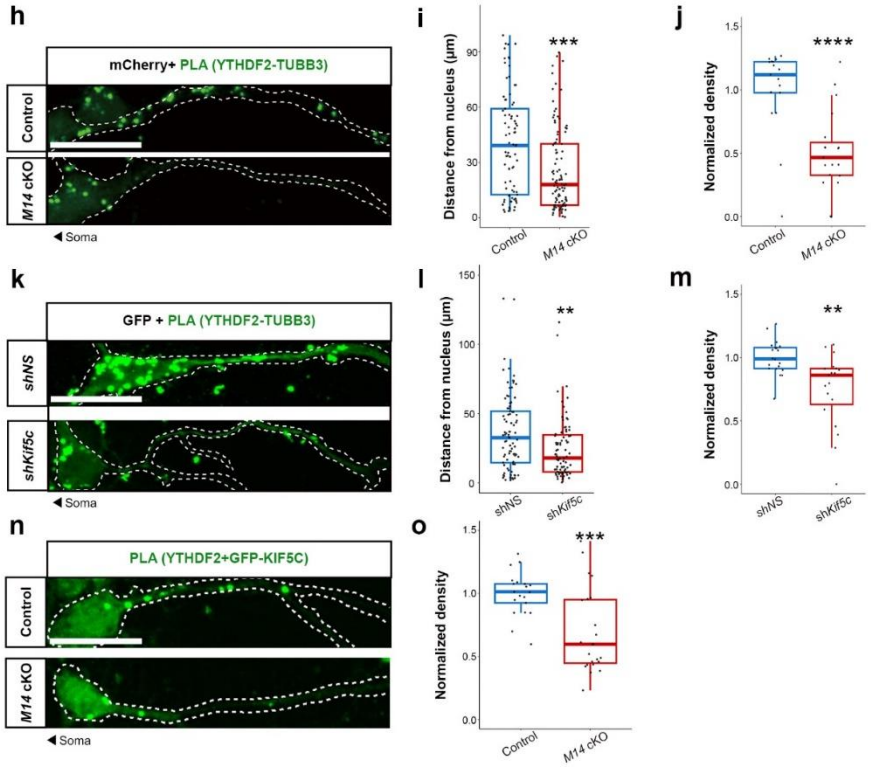

Revised Fig. 5. YTHDF2 interacts with the transport machinery and neurite microtubules in an m^{6}A-dependent manner. (h-j) YTHDF2 localization to distal neurite decreased in *M14* cKO mouse primary neuron. Shown in (h) are representative PLA signals (Green) showing endogenous YTHDF2-TUBB3 association (Scale bar: 20μm). The distance from the nucleus was quantified in (i) (Control n=81, *M14* cKO n=108, *P*=0.0001524) and the relative density is quantified in (j) (Control n=17, *M14* cKO n=19, *P*=8.88e-05). **(k-m)** YTHDF2 localization to distal neurites decreased in mouse primary neuron upon *Kif5c* knockdown. Shown in (k) are representative PLA signals (green) indicating endogenous YTHDF2-TUBB3 association in control and *Kif5c* knockdown conditions (scale bar: 20μm). The distance from the nucleus was quantified in (l) (Control n=89, *shKif5c* n=91, *P*=0.001227) and the relative density is quantified in (m) (Control n=20, *shKif5c* n=19, *P*=0.001124).
(n-o) YTHDF2-KIF5C complex localization to distal neurites decreased in *M14* cKO mouse primary neuron. Shown in (n) are representative PLA signals (Green) showing YTHDF2+GFP-KIF5C association (Scale bar: 20μm). The relative density is quantified in (o) (Control n=21, *M14* cKO n=23, *P*=0.0003697). Significance was evaluated using two-tailed unpaired Student's t-tests (i, j, l, m, and o). ns, not significant, ***P* < 0.01, ****P*<0.001, *****P*<0.0001

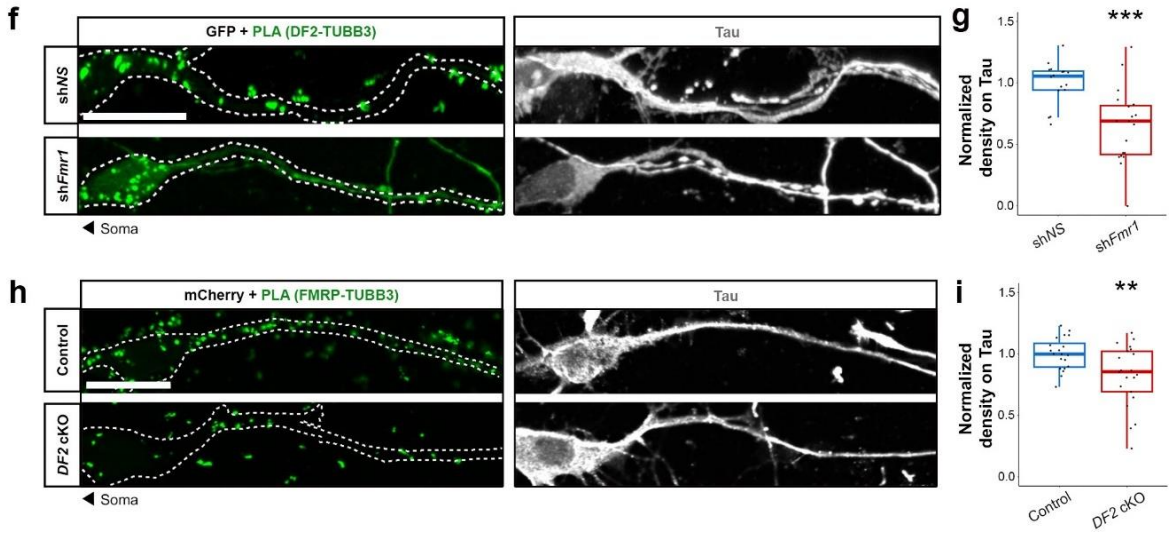

Revised Fig.6. FMRP interacts with YTHDF2 to facilitate transport of m⁶A-tagged mRNAs to distal neurites in developing neurons. **(f-g)** YTHDF2 localization to neurites decreased in *Fmr1* KD mouse primary neurons. Shown in (f) are representative PLA signals (green) and Tau indicating endogenous YTHDF2-TUBB3 associations in control and *Fmr1* KD mouse primary neurons (Scale bar: 20μm). The relative density on tau is quantified in (g) (Control n=16, *Fmr1* KD n=19, *P*= 0.0002645). **(h-i)** FMRP localization to neurites decreased in *DF2* cKO mouse primary neurons. Shown in (h) are representative PLA signals (green) and Tau indicating endogenous FMRP-TUBB3 associations in control and *DF2* cKO mouse primary neurons (Scale bar: 20μm). The relative density on tau is quantified in (i) (Control n=20, *DF2* cKO n=21, *P*= 0.006918).

Changes in the text:

(Line 663-665) Finally, Hoechst solution was added for 3 minutes after washing, and mounting media was applied to the slides to fix the coverslips for storage in the dark at 4°C. If required, immunocytochemistry was performed after the smFISH.

(Line 682-684) After two washes with TBS, mounting media was applied to the slides to fix the coverslips for storage in the dark at 4°C. If required, immunocytochemistry was performed after the PLA.

(Line 824-828) Quantification of smFISH single molecules and PLA analysis were conducted using NeuronJ by measuring the distance between a single RNA molecule and the center of the nucleus along axon tracks labeled with fluorescent proteins or Tau. The normalized density of smFISH and PLA was quantified by calculate the ratio of neurite signal per total signal and normalized it with control ratio.

9) Overall, I do not think that the data presented for Figure 6 is convincing.
o The identified motif (NGACNNN) for FXR2 and FMRP is very similar to the m6A motif, which could explain its enrichment. Is there an enrichment for the canonical DRACH m6A motif?

We thank the reviewer for raising this important issue, which was also noted by Reviewer #1. To ensure that the m⁶A DRACH motif did not interfere with the motif enrichment analysis, we

reanalyzed the sequence of Q2. Specifically, we performed motif enrichment analysis using AME on the ±50 bp regions surrounding the m⁶A sites' DRACH motifs in Q2 mRNAs[23].

As a result, we confirmed that the FMRP binding motif is significantly enriched near the m⁶A sites ($p = 7.25 \times 10^{-3}$) (Revised Fig. 6a), whereas FXR1 and FXR2 showed only weak enrichment ($p = 2.84 \times 10^{-1}$ and 2.17×10^{-1}, respectively). These findings suggest that potential FMRP binding sites that do not overlap with m⁶A sites are located within ~50 bp of the m⁶A site, which may facilitate interactions among the mRNA, YTHDF2, and FMRP.

Revised Fig.6. FMRP interacts with YTHDF2 to facilitate transport of m⁶A-tagged mRNAs to distal neurites in developing neurons.
(a) Motif enrichment analysis of the Q2 3'UTR m⁶A proximal sequence (±50 bp).

Changes in the text:
(Line 376-383) Next, we hypothesized that YTHDF2 associates with other RBPs and selectively localizes mRNA to the distal axon depending on target RNA characteristics, including m⁶A and 3'UTR sequence. When we examined m⁶A stoichiometry across different RBP target mRNAs, FMRP target mRNAs exhibited significantly higher m⁶A stoichiometry than non-target mRNAs (Extended Data Fig. 8a). To further evaluate our model, we performed motif enrichment analysis on sequences proximal to m⁶A sites within the 3′UTRs of the Q2 and Q1 groups (Fig. 3b) [18]. As a result, we found FMRP binding motifs were enriched in Q2 3'UTR sequences, particularly near m6A sites, compared with Q1 3′UTR sequences (Fig. 6a, Extended Data Fig. 8b).

We also compare our mouse brain m⁶A-SAC-seq identified 10304 m⁶A sites with the mouse brain FMRP CLIP-seq database [15](Reviewer fig. 5). We compare 262 m⁶A sites in q2 transcripts, the group we focus on in this study, and 403 FMRP binding peaks. As a result, only a single m⁶A site on the CDS of *Txnip* was overlapped with FMRP peaks. Altogether, we conclude that FMRP binding sites are enriched in the m⁶A proximal Q2 3'UTR sequence, but are mutually exclusive with the m⁶A sites.

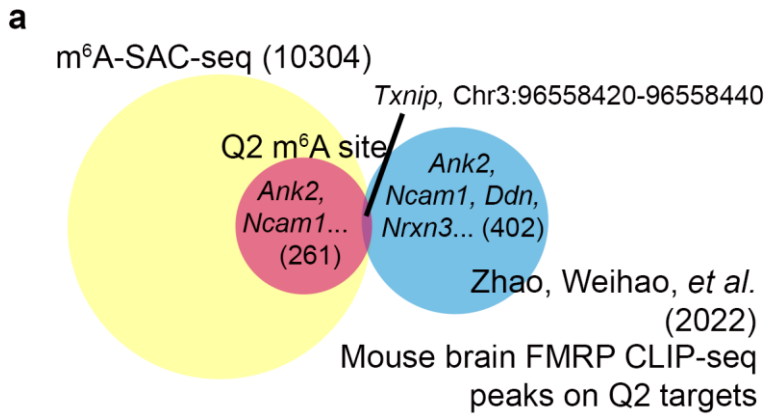

Reviewer Fig. 5. FMRP binding sites do not overlap with the m^{6}A site
(a) Venn diagram comparing the m^{6}A-SAC-seq site and FMRP CLIP-seq peaks.

10) Additional images for YTHDF2 PLA with FMRP should be provided (as is presented in figure S5 for DF2-CNOT1).

We appreciate the reviewer's suggestion, which was also raised by Reviewer #1 regarding the PLA negative control. We performed PLA assays for DF2–IgG, FMRP–IgG, and IgG–KIF5C in WT primary mouse neurons at DIV6 (Revised Extended Data Fig. 7c). As a result, only minimal background IgG PLA signals were detected, which can be considered negligible.

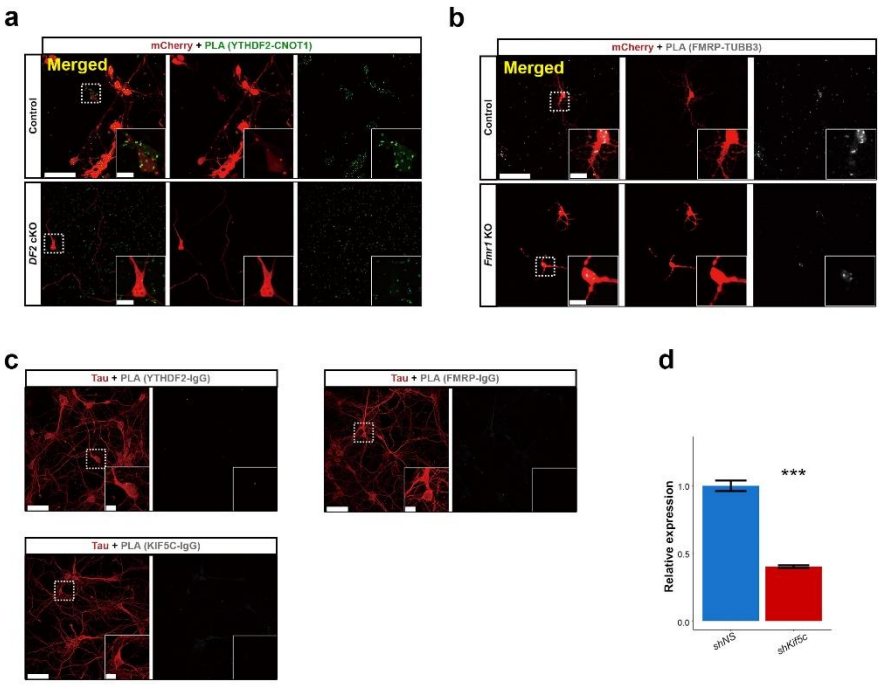

Revised Extended Data Fig. 7. Validation of PLA experiments and *shKif5c*.
(a-c) Validation of Proximity Ligation Assay (PLA) experiments with negative control. YTHDF2-CNOT1 PLA signal significantly reduced in *DF2* cKO represented on **(a)** (scale bar: 50μm, lower panel scale bar: 10μm). FMRP-TUBB3 PLA signal significantly reduced in *Fmr1* KO represented on **(b)** (scale bar: 50μm, lower panel scale bar: 10μm). Signals appearing in mCherry-negative areas are presumed to originate from cells that were not infected by AAV-mCherry-IRES-Cre viruses. **(c)** YTHDF2, FMRP, and KIF5C PLA with IgG control. PLA signal significantly reduced with IgG represented on (c) (scale bar: 50μm, lower panel scale bar: 10μm). **(d)** Validation of *Kif5c* KD in N2A by qPCR. Values represent mean ± SEM after being normalized by GAPDH expression

11) The signal intensity in the images presented in fig. 6d is drastically different. Are the observed effects caused by differences in expression or of cell-to-cell variability? This signal is not represented in the quantification in figure 6e. Indeed, I would expect many interactions near the nucleus in control cells.

We appreciate the reviewer's comment. We have updated the representative images in Figures 5 and 6 for better representation in the quantification, and additionally included Tau immunocytochemistry data to clarify that the PLA signals overlap with axonal regions.

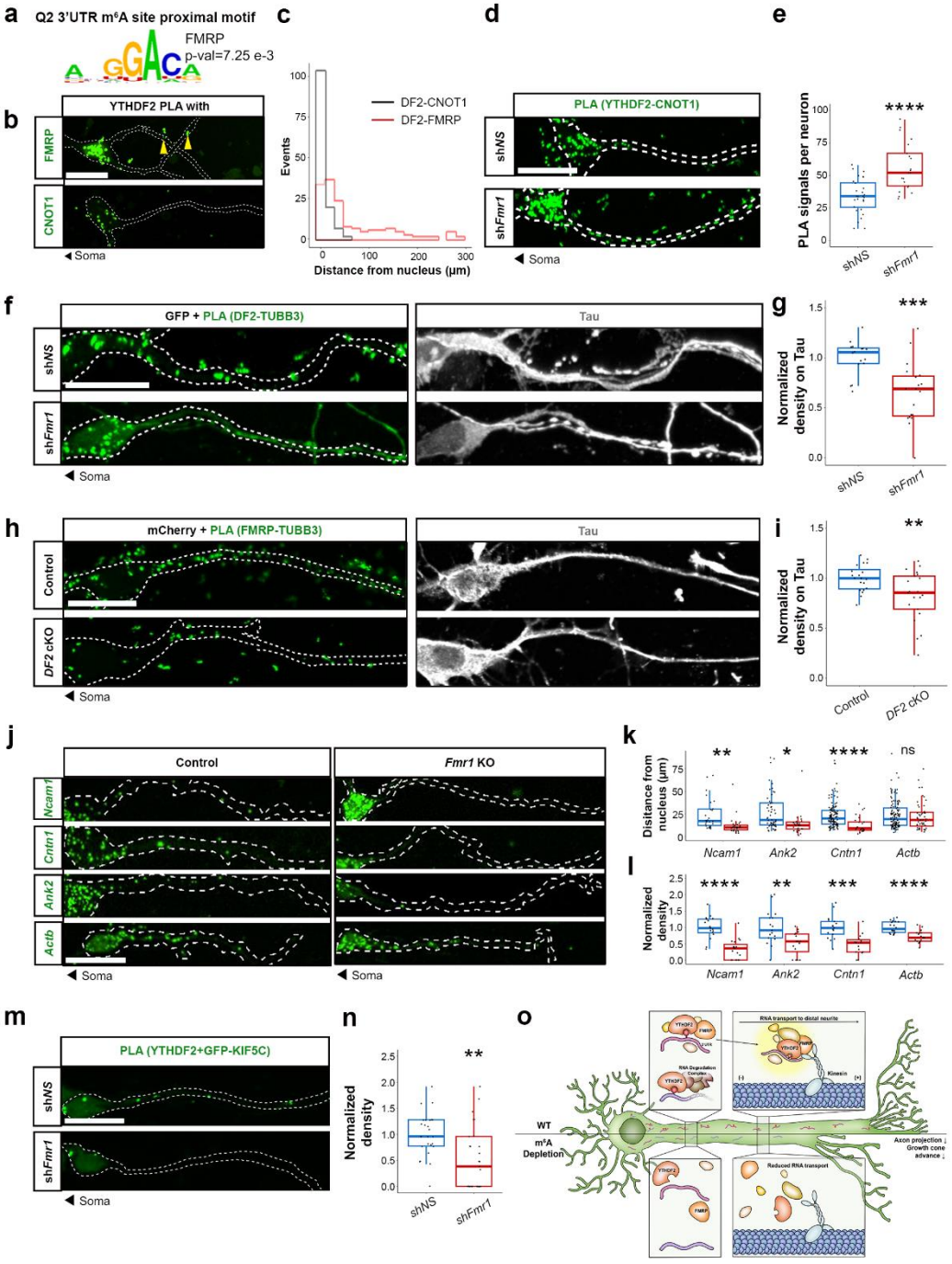

Revised Fig.6. FMRP interacts with YTHDF2 to facilitate transport of m⁶A-tagged mRNAs to distal neurites in developing neurons. **(a)** Motif enrichment analysis of the Q2 3'UTR m⁶A proximal sequence (±50 bp). **(b-c)** YTHDF2 is associated with functional cofactors in different subcellular locations. Shown in (b) are representative PLA signals (green), representing endogenous YTHDF2-CNOT1 and YTHDF2-FMRP associations (Scale bar: 20μm). The yellow arrowheads indicate PLA signals in the distal neurites. The distribution of PLA signals in neurites is quantified in (c). **(d-e)** YTHDF2-CNOT1 associations decreased in *Fmr1* KD mouse primary neurons. Shown in (d) are representative PLA signals (green) indicating endogenous YTHDF2-CNOT1 associations in control and *Fmr1* KD mouse primary neurons (Scale bar: 20μm). The number of PLA signals per neuron was quantified in (e)

(Control: n = 28, *Fmr1* KD: n = 21, *P* = 9.43e-06). **(f-g)** YTHDF2 localization to neurites decreased in *Fmr1* KD mouse primary neurons. Shown in (f) are representative PLA signals (green) and Tau indicating endogenous YTHDF2-TUBB3 associations in control and *Fmr1* KD mouse primary neurons (Scale bar: 20μm). The relative density on tau is quantified in (g) (Control n=16, *Fmr1* KD n=19, *P*= 0.0002645). **(h-i)** FMRP localization to neurites decreased in *DF2* cKO mouse primary neurons. Shown in (h) are representative PLA signals (green) and Tau indicating endogenous FMRP-TUBB3 associations in control and *DF2* cKO mouse primary neurons (Scale bar: 20μm). The relative density on tau is quantified in (i) (Control n=20, *DF2* cKO n=21, *P*= 0.006918). **(j-l)** RNA localization to neurites decreased in *Fmr1* KO mouse primary neurons. Shown in (j) are representative smFISH signals (green) representing endogenous *Ncam1*, *Cntn1*, *Ank2*, and *Actb* in control and *Fmr1* KO conditions (Scale bar: 20μm). The distance from the nucleus was quantified in (k) (*Ncam1*: Control n = 26, *Fmr1* KO n = 33; *P* = 0.0005381. *Cntn1*: Control n = 62, *Fmr1* KO n = 27; *P* = 0.04902. *Ank2*: Control n = 125, *Fmr1* KO n = 25; *P* = 0.0005668. *Actb*: Control n = 123, *Fmr1* KO n = 48; *P* = 0.6665) and the relative density of smFISH puncta in neurites compared to the total is quantified in (l) (*Ncam1*: Control n=17, *FMRP* cKO n=19; *P*=, 4.408e-07 *Cntn1*: Control n=17, *FMRP* cKO n=16; *P*=0.003859, *Ank2*: Control n=17, *FMRP* cKO n=15; *P*=0.0001217, *Actb*: Control n=18, *FMRP* cKO n=17; *P*=5.784e-05). **(m-n)** YTHDF2-KIF5C complex localization to distal neurites decreased in *Fmr1* KD mouse primary neuron. Shown in (m) are representative PLA signals (Green) showing YTHDF2+GFP-KIF5C association (Scale bar: 20μm). The relative density is quantified in (n) (Control n=26, *Fmr1* KD n=29, *P*=0.001066).

(j) Model for the role of m^{6}A and YTHDF2 in regulating RNA localization to neurites. YTHDF2 recognizes m^{6}A-modified transcripts. The m^{6}A modifications on mRNA may recruit different complexes, either transport or degradation complexes. A subset of m^{6}A-tagged transcripts bound by YTHDF2 with transport complex proteins like FMRP is localized to distal neurites. In contrast, another subset of m^{6}A-tagged transcripts bound by YTHDF2 recruits the RNA degradation machinery for rapid decay. Upon m^{6}A depletion, a subset of mRNAs is unable to localize to distal neurites despite their stabilization. Significance was evaluated using two-tailed unpaired Student's t-tests (e, g, i, k, l, and n). ns, not significant; *$P < 0.05$, **$P < 0.01$, ***$P < 0.001$, ****$P < 0.0001$.

12) FMRP controls the localization of many RNAs without YTHDF2. Is the reduction in localization in fig. 6i dependent on YTHDF2? Does a double KD/KO potentiate this effect?

We appreciate the reviewer's suggestion, which was also raised by Reviewer #1 regarding the role of FMRP as an independent m^{6}A reader protein. We performed smFISH on DIV6 mouse primary neurons under WT/DF2 cKO and shNS/sh*Fmr1* knockdown conditions. Consistent with our previous smFISH experiments, both *DF2* cKO and *Fmr1* KD conditions showed reduced Ncam1 mRNA localization to neurites compared with controls. Notably, the double-depletion condition (*DF2* cKO + *Fmr1* KD) exhibited a far more pronounced reduction in mRNA neurite localization than either single-depletion or control conditions (Reviewer Fig. 9a-b). FMRP is known to have multiple roles, including regulating RNA nuclear export, stability, and translation. Therefore, although the YTHDF2–FMRP–KIF5C complex has a specific function in transporting m^{6}A-modified RNAs to distal neurites, additional functions of FMRP may further contribute to the observed reduction in RNA localization upon its depletion. We have incorporated this discussion

into the Result section.

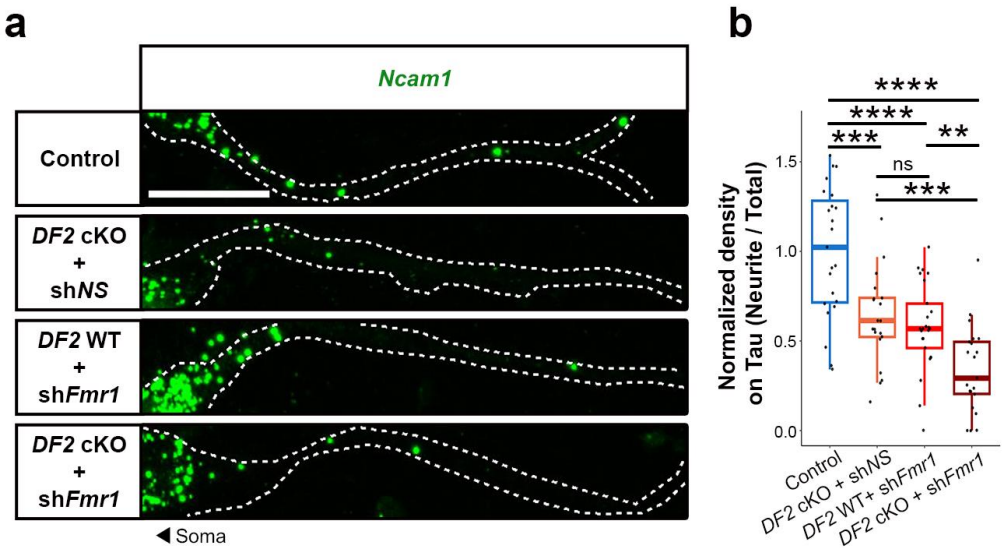

Reviewer Fig. 9. RNA localization was reduced in *Ythdf2* and *Fmr1* knockdown conditions. **(a-b)** RNA localization to neurites decreased in YTHDF2; FMRP double depleted mouse primary neurons. Shown in (o) are representative smFISH signals (green) representing endogenous Ncam1 in experimental conditions (Scale bar: 20μm). The relative density is quantified in (p) (Control n=23, DF2 cKO n=21, FMRP KD n=25, double cKO/KD n=21; Control-DF2 cKO P=0.0009254, Control-FMRP KD P=2.175e-05, Control-double cKO/KD P=1.525e-08, DF2 cKO-FMRP KD P=0.4068, DF2 cKO-double cKO/KD P=0.0005956, FMRP KD-double cKO/KD P=0.00172)

Changes in the text:

(Line 413-415) We note that we do not exclude the possibility that FMRP partially regulates the localization of these mRNAs in a YTHDF2-independent manner, as FMRP is well known to participate in multiple RNA regulatory processes in the neuron[18,24–28].

o Overall, I think that more/better quality images and their deposition in a repository would increase the confidence in this data.

General comments:
I find the finding on the RNA stability in M14 cKO and DF2 cKO cells very interesting. It seems that most changes in stability occur on RNAs that do not contain m6A. Rather than seeing a shift of the ECDF curve to the right, we see a change in its shape: the most stabilized and destabilized transcripts do not contain m6A sites. To me, this suggests that in mature neurons, the main function of m6A might not be RNA decay, but rather other functions such as trafficking or translational control. Since this study uses both in vivo samples (subjected to potential differentiation effects) and cultured neurons, it would be interesting to discuss potential differences between m6A/DF function in dividing cells and post-mitotic neurons.

References

1. Chesler, A. T. *et al.* Selective Gene Expression by Postnatal Electroporation during Olfactory Interneuron Neurogenesis. *PLoS One* 3, e1517- (2008).
2. Saito, T. & Nakatsuji, N. Efficient gene transfer into the embryonic mouse brain using in vivo electroporation. *Dev Biol* 240, 237–246 (2001).
3. Kawasaki, H., Iwai, L. & Tanno, K. Rapid and efficient genetic manipulation of gyrencephalic carnivores using in utero electroporation. *Mol Brain* 5, 24 (2012).
4. Zhu, J. *et al.* Conditional deletion of Gata3 shows its essential function in TH1-TH2 responses. *Nat Immunol* 5, 1157–1165 (2004).
5. Franco, S. J., Martinez-Garay, I., Gil-Sanz, C., Harkins-Perry, S. R. & Müller, U. Reelin Regulates Cadherin Function via Dab1/Rap1 to Control Neuronal Migration and Lamination in the Neocortex. *Neuron* 69, 482–497 (2011).
6. Kang, E. *et al.* Interaction between FEZ1 and DISC1 in Regulation of Neuronal Development and Risk for Schizophrenia. *Neuron* 72, 559–571 (2011).
7. Schindelin, J. *et al.* Fiji: an open-source platform for biological-image analysis. *Nat Methods* 9, 676–682 (2012).
8. Poulopoulos, A. *et al.* Subcellular transcriptomes and proteomes of developing axon projections in the cerebral cortex. *Nature* 565, 356–360 (2019).
9. van Beuningen, S. F. B. & Hoogenraad, C. C. Neuronal polarity: remodeling microtubule organization. *Curr Opin Neurobiol* 39, 1–7 (2016).
10. Bertrand, E. *et al.* Localization of ASH1 mRNA particles in living yeast. *Mol Cell* 2, 437–445 (1998).
11. Li, M. *et al.* Ythdf2-mediated m6A mRNA clearance modulates neural development in mice. *Genome Biol* 19, 69 (2018).
12. Edens, B. M. *et al.* FMRP Modulates Neural Differentiation through m6A-Dependent mRNA Nuclear Export. *Cell Rep* 28, 845-854.e5 (2019).
13. Zhang, G. *et al.* Dynamic FMR1 granule phase switch instructed by m6A modification contributes to maternal RNA decay. *Nat Commun* 13, 859 (2022).
14. Zhao, W. *et al.* POSTAR3: an updated platform for exploring post-transcriptional regulation coordinated by RNA-binding proteins. *Nucleic Acids Res* 50, D287–D294 (2022).
15. Loedige, I. *et al.* mRNA stability and m6A are major determinants of subcellular mRNA localization in neurons. *Mol Cell* 83, 2709–2725 (2023).
16. Shigeoka, T. *et al.* On-Site Ribosome Remodeling by Locally Synthesized Ribosomal Proteins in Axons. *Cell Rep* 29, 3605-3619.e10 (2019).
17. Worpenberg, L. *et al.* Ythdf is a N6-methyladenosine reader that modulates Fmr1 target mRNA selection and restricts axonal growth in Drosophila . *EMBO J* 40, (2021).
18. Soldano, A. *et al.* The m6A reader Ythdf restricts axonal growth in Drosophila through target

selection modulation of the Fragile X mental retardation protein. https://doi.org/10.1101/2020.03.04.976886 doi:10.1101/2020.03.04.976886.

19. Bauer, K. E. *et al.* Live cell imaging reveals 3′-UTR dependent mRNA sorting to synapses. *Nat Commun* 10, 3178 (2019).
20. Zhuang, M. *et al.* YTHDF2 in dentate gyrus is the m6A reader mediating m6A modification in hippocampus-dependent learning and memory. *Mol Psychiatry* 28, 1679–1691 (2023).
21. Jung, J. *et al.* mRNA transport, translation, and decay in adult mammalian central nervous system axons. *Neuron* 111, 650-668.e4 (2023).
22. Han, L. *et al.* Single-cell spatial transcriptomic atlas of the whole mouse brain. *Neuron* 113, 2141-2160.e9 (2025).
23. McLeay, R. C. & Bailey, T. L. Motif Enrichment Analysis: a unified framework and an evaluation on ChIP data. *BMC Bioinformatics* 11, 1–11 (2010).
24. Yu, J. *et al.* The m6A Readers YTHDF1 and YTHDF2 Synergistically Control Cerebellar Parallel Fiber Growth by Regulating Local Translation of the Key Wnt5a Signaling Components in Axons. *Advanced Science* 8, (2021).
25. Jung, J. *et al.* mRNA transport, translation, and decay in adult mammalian central nervous system axons. *Neuron* 111, 650-668.e4 (2023).
26. Pilaz, L. J., Lennox, A. L., Rouanet, J. P. & Silver, D. L. Dynamic mRNA Transport and Local Translation in Radial Glial Progenitors of the Developing Brain. *Current Biology* 26, 3383–3392 (2016).
27. Dictenberg, J. B., Swanger, S. A., Antar, L. N., Singer, R. H. & Bassell, G. J. A Direct Role for FMRP in Activity-Dependent Dendritic mRNA Transport Links Filopodial-Spine Morphogenesis to Fragile X Syndrome. *Dev Cell* 14, 926–939 (2008).
28. Zou, Z. *et al.* FMRP phosphorylation modulates neuronal translation through YTHDF1. *Mol Cell* https://doi.org/10.1016/j.molcel.2023.10.028 (2023) doi:10.1016/j.molcel.2023.10.028.

EDITOR COMMENTS

You will see that, while the reviewers find that your revisions improved the manuscript, some important points remain to be addressed. We agree with Reviewer #1 that the mechanism by which YTHDF2 promotes axonal mRNA transport remains unclear. Specifically, please remove the claims regarding FMRP in the title and the abstract, and move the model (fig. 6o) to the Supplementary information. Please revise your manuscript, addressing all the remaining issues raised by the reviewers.

We thank the editor for these constructive suggestions and for the careful evaluation of our revised manuscript. We have moved the model figure (Fig. 6o) to Revised Extended Data Fig. 10, as requested. In this revision, we have also performed additional experiments that further clarify the mechanism by which YTHDF2 promotes axonal mRNA transport.

We fully appreciate the editor's concern regarding the strength of the mechanistic conclusions. At the same time, we believe that our finding—that FMRP plays a pivotal role in switching the function of YTHDF2 on m^{6}A-tagged mRNAs from degradation to transport—represents a central and novel contribution of this study (please also refer to our response to Reviewer 1, comment 4).

In light of these new data and their significance, we respectfully request that the title and abstract be retained in their current form, as they reflect the key conceptual advance and may enhance the visibility and impact of the work within the RNA biology field. However, we are of course willing to revise them further if the editor feels it is necessary.

We also sincerely thank Reviewer 1 for recognizing the overall improvement in the manuscript and for providing insightful comments. This letter provides point-by-point responses to all reviewer comments, along with descriptions of additional experiments supporting our central model. The original reviewers' comments are shown in black, followed by our responses in blue. Revisions to the text and figures appears in yellow within the red highlights, and paragraph line numbers in the revised manuscript are indicated in cyan. To address the reviewers' comments, we have also revised the figure numbering.

REVIEWER COMMENTS

Reviewer #1 (Remarks to the Author):

In the revised manuscript, the authors have performed new experiments and analysis, and improved the overall quality of the manuscript. However, evidence to fully support some of the authors' major claims remains insufficient.

1. A general concern in the manuscript is that primary dendrites are examined in the analyses instead of axons and the authors call them "distal neurites". This is seen in the PLA, immunostaining, morphological analysis, live-cell MS2 tracking experiments, etc. I highly recommend the authors to use consistent nomenclatures.

We thank the reviewer for this important comment regarding the nomenclature of neuronal processes. As also noted in Reviewer 1's previous comments, the distinction between dendrites and axons is critical for interpreting our conclusions on axonal mRNA transport.

Previous reviewer comment 1-1: In particular, the function of YTHDF2 in axonal mRNA transport is unclear. No functional experiments on axonal mRNA localization related to YTHDF2 cKO were presented in the manuscript. Additional CC-seq in DF2-cKO mice and Tau (or other axonal marker) co-staining in cultured neurons can provide required evidence for the authors' claims; previous reviewer comment 1-6: Fig 3e - Fig4h - Fig 5e, g - Fig 6 b,d,f,h : Primary neurites/dendrites are being analyzed instead of axons in these figures. This causes a major problem to the authors' claim on the role of m6A and DF2 in axonal mRNA transport and development. Co-staining with an axonal marker such as Tau is required for identifying the correct subcellular compartment.

In response, we have made significant efforts to perform additional experiments incorporating co-staining with the axonal marker Tau, as the reviewer suggested. Based on these analyses, we have carefully reassessed the relevant datasets and updated the corresponding figures (revised Figs. 3–6 and Extended Data Figs. 5–8).

We believe these revisions address the reviewer's concern and improve the accuracy and clarity of our study.

Changes in the text:

(Line 354~358) The results revealed a significant reduction in PLA signals in the axons of *M14* cKO neurons compared to those in the axons of WT neurons. This observation suggests that m^{6}A modification is crucial for the interaction between YTHDF2 and microtubules in the axons (Fig. 5h-j, Extended Data Fig. 8a-g).

(Line 397~399)

The results revealed a significant decrease in YTHDF2-TUBB3 PLA signals in the axons of *Fmr1* knockdown neurons compared to those in control neurons (Fig. 6f-g, Extended Data Fig. 9d-e), suggesting that FMRP facilitates the microtubule association of YTHDF2. Conversely, FMRP-TUBB3 PLA signals were markedly reduced in the axons of *Ythdf2* knockout neurons compared to those in control neurons (Fig. 6h-l, Extended Data Fig. 9f-g).

(Line 1053, 1056)

(f-g) YTHDF2 localization to axons decreased in *Fmr1* KD mouse primary neurons.

(h-i) FMRP localization to axons decreased in *DF2* cKO mouse primary neurons.

2. Another concern is the lack of evidence to claim a specific role of YTHDF2 in promoting distal mRNA transport. Expression levels of the three YTHDF cytoplasmic reader proteins were similar at the developmental stage of the study based on TPM measurement. A previous report has revealed the role of YTHDF1 in controlling APC expression and APC-mediated axonal mRNA transport in hippocampal neurons and cortical neurons (PMID: 40402742; this publication should be cited given its direct relevance to the current work).

We thank the reviewer for raising this important point. We apologize for inadvertently missing the elegant study by L. Broix et al. (PMID: 40402742)[1], which was published during the revision process. We have now incorporated and cited this work in the revised manuscript.

Regarding the potential redundancy of YTHDF proteins, we provide five lines of experimental evidence supporting a YTHDF2-specific role in promoting distal mRNA transport in neurites.

First, we agree that the three cytoplasmic YTHDF readers show comparable expression levels in the postnatal brain. However, similar expression levels do not necessarily imply functional

redundancy. A key finding of our study is the subcellular compartment-specific role of YTHDF2, particularly its interaction with the transport machinery in neurites. As shown in Fig. 5h–o, YTHDF2 associates with neurite microtubules in an m^6A- and Kif5c-dependent manner.

In contrast, L. Broix et al. demonstrated that YTHDF1 regulates APC mRNA translation in the soma and thereby *indirectly* influences APC-mediated axonal mRNA transport. To determine whether YTHDF1 plays a similar direct role in cytoskeletal mRNA transport, we performed PLA assays to assess the association between YTHDF1 and neurite microtubules. However, we did not detect interaction between YTHDF1 and microtubules in Tau-positive axons, in contrast to YTHDF2 (Revised Extended Data Fig. 8a-b). These results suggest that YTHDF1 and YTHDF2 function within distinct protein complexes.

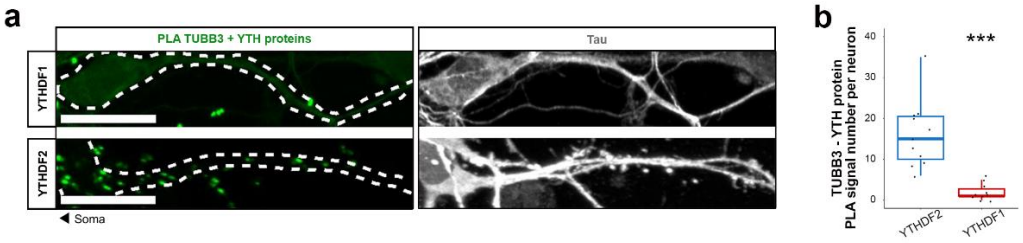

Revised Extended Data Fig. 8. Validation of PLA experiments and YTHDF1 interacting proteins.

(a-b) TUBB3 interacts with YTHDF2, not with YTHDF1. Shown in (a) are representative PLA signals (Green) showing endogenous YTH proteins-TUBB3 association (Scale bar: 20µm). The number of signals per neuron was quantified in (b).

Second, we reanalyzed YTHDF2-interacting proteins using our LC–MS/MS dataset (Supplementary Table 4). Notably, no peptides corresponding to YTHDF1, YTHDF3, and APC were detected, whereas FMRP and multiple microtubule-associated proteins were robustly enriched. This finding supports the notion that YTHDF2 forms a distinct protein complex in neurons that does not include YTHDF1, YTHDF3, or APC. Importantly, this exclusion of other YTHDF readers was consistently observed in an independent LC–MS/MS analysis performed for this revision (Reviewer Table 1).

	YTHDF1	YTHDF2	YTHDF3
LC/MS Abundances (Grouped): Control	NA	132.1	NA

Reviewer table. 1. LC-MS/MS result of DF proteins. YTHDF1 and YTHDF3 did not detected on YTHDF2-CoIP LC-MS/MS

Third, to directly test the specificity of YTHDF2 in regulating cytoskeletal mRNA transport, we performed smFISH analysis of *Ncam1* and *Ank2* mRNAs following knockdown of *Ythdf1* or *Ythdf3*.

In contrast to YTHDF2 depletion, neither Ythdf1 nor Ythdf3 knockdown resulted in significant changes in the subcellular localization of these transcripts (Revised Extended Data Fig. 7d-e).

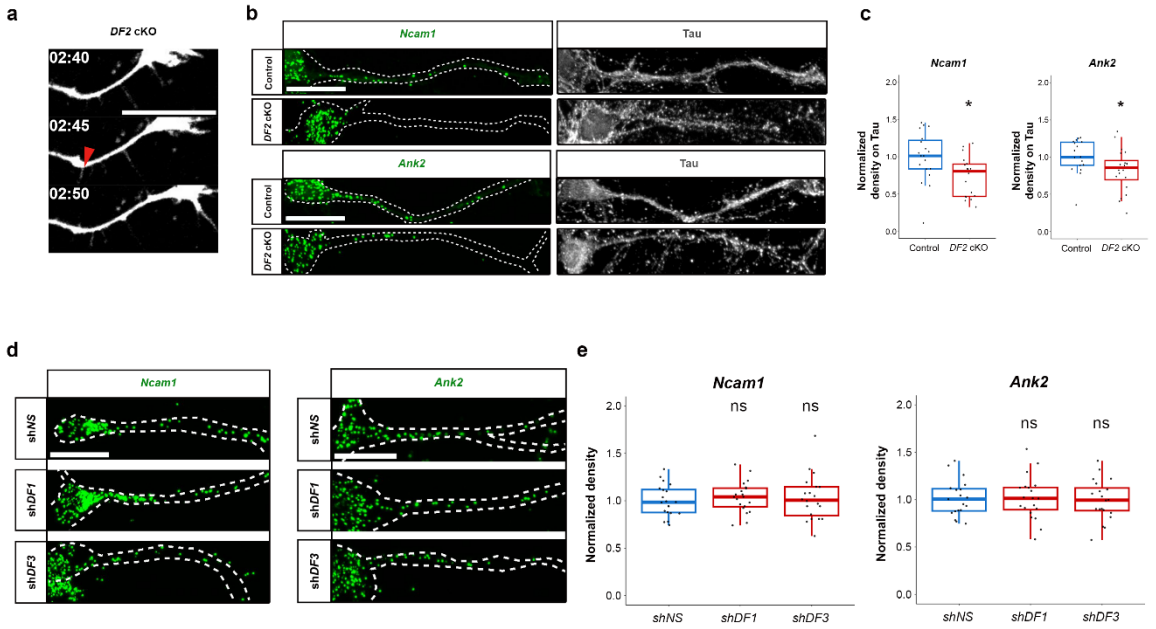

Revised Extended Data Fig. 7. Loss of *Ythdf2* leads to a disrupted RNA localization and neuron projection. (a) The transient protrusion detected (red arrow) during *DF2* cKO neuron live imaging. (scale bars: 20 μm) **(b-c)** *DF2* cKO primary cultured neurons showed reduced axonal RNA localization. Shown in (b) are representative smFISH signals (Green) representing endogenous *Ncam1* and *Ank2* (Scale bars: 20 μm) with axon marker Tau staining. The relative density is quantified in (c). **(d-e)** *DF1* and *DF3* KD primary cultured neurons does not showed reduced axonal RNA localization. Shown in (d) are representative smFISH signals representing endogenous *Ncam1* and *Ank2* (Scale bars: 20 μm) with axon marker Tau staining. The relative density is quantified in (e). Significance was evaluated using two-tailed unpaired Student's t-tests (c and e). ns, not significant; $*P < 0.05$. Statistical details and sample sizes are provided in the supplementary table5.

Fourth, we compared our target RNAs with high-confidence APC CLIP-seq datasets.[2] As a result, we observed only limited overlap among CC-seq DEGs, Q2 transcripts, and APC targets (Reviewer Fig. 1). Of the 260 APC target RNAs, 35 overlapped with m^{6}A-modified transcripts that were downregulated in CC-seq. Moreover, only 11 transcripts overlapped with our Q2 set (i.e., our transcripts of interest).

These results indicate that the target mRNAs described in this manuscript are largely distinct from the transcripts transported by APC, as reported by L. Broix et al., and suggest that the YTHDF1–APC axis does not directly mediate the axonal localization of these mRNAs.

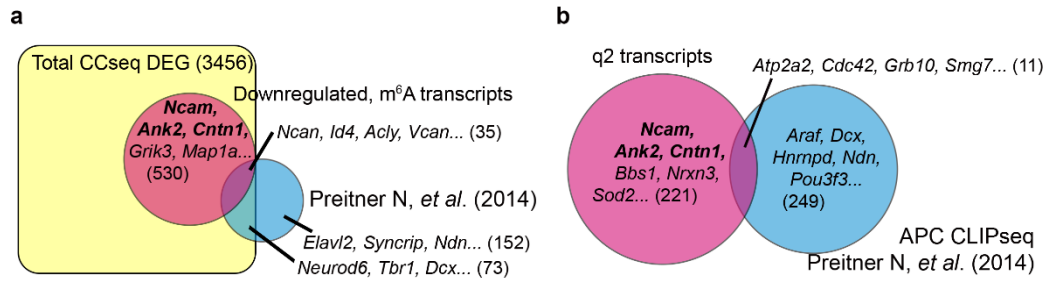

Reviewer Figure. 1. APC binding transcripts weakly overlapped with our targets. (a) Venn diagram comparing the CC-seq datasets and APC CLIPseq dataset. (b) Venn diagram comparing the q2 transcripts and APC CLIPseq dataset.

Fifth, as shown in our previous revision, *YTHDF1* and *YTHDF3* knockdown did not alter the dynamics of growth cones or protrusion formation in cultured primary cortical neurons (Extended Data Fig. 6b-e), suggesting that YTHDF1 and YTHDF3 do not play redundant roles in compensating for these aspects of YTHDF2 loss of function.

Collectively, these results support a non-redundant, YTHDF2-specific role in promoting distal mRNA transport in neurites. Importantly, our findings are not in conflict with the role of YTHDF1 proposed by L. Broix et al.; rather, their work suggests that YTHDF1 mediates the transport of a distinct set of mRNAs via a separate transport protein complex. *These two distinct mechanisms together provide a more comprehensive understanding of m^{6}A-mediated mRNA transport.*

Changes in the text:

(Line 357-359) Notably, we did not detect an interaction between YTHDF1 and microtubules in Tau-positive axons, in contrast to YTHDF2 (Extended Data Fig. 8a–b).

(Line 479-504) The three YTHDF paralogs—YTHDF1, YTHDF2, and YTHDF3—share highly conserved protein sequences and have been reported to exhibit functional redundancy in several cellular contexts [43–45]. However, emerging evidence suggests that differences in their low-complexity domains and post-translational modifications confer distinct physiological functions [46–48]. Consistent with this, our data indicate that YTHDF proteins are not functionally redundant in regulating mRNA transport during early neuronal differentiation. Instead, YTHDF2 appears to play a selective and direct role in promoting mRNA localization in neurites. For example, although all three YTHDF proteins are expressed at comparable levels in the postnatal brain (data not shown), *DF2* cKO mice exhibit subviability, neurological deficits, and impaired axon projection (Fig. 4 and Extended Data Fig. 6), suggesting that YTHDF1 and YTHDF3 do not compensate for the loss of YTHDF2 *in vivo*. In addition, we find that YTHDF2, but not YTHDF1, associates with neurite microtubules and motor proteins in an m^{6}A-dependent manner, suggesting that the subcellular compartment of YTHDF2 function differs from

that of YTHDF1 (Extended Data Fig. 8). Consistent with this, loss of *Ythdf2*—but not *Ythdf1* or *Ythdf3*—disrupts neurite localization of target mRNAs and impairs growth cone dynamics (Extended Data Fig. 6 and Extended Data Fig. 7). A recent study demonstrating that YTHDF1 regulates APC mRNA translation in soma and indirectly modulates axonal mRNA transport via APC-associated ribonucleoprotein complexes[7]. In contrast, our data support a model in which YTHDF2 directly engages the cytoskeletal transport machinery to mediate the localization of m^{6}A-tagged mRNAs. Notably, neither YTHDF1 nor APC was identified in the YTHDF2 interactome in our *in vivo* co-immunoprecipitation and mass spectrometry analyses (Fig. 5 and Supplementary Table 4), suggesting YTHDF2-transport complex mediates the transport of a distinct set of mRNAs via a separate transport protein complex from the APC-dependent transport machinery. Together, these findings support a model in which YTHDF family proteins function through mechanistically distinct, non-redundant pathways, with YTHDF1 proposed to regulate APC translation in the soma, whereas YTHDF2 directly controls mRNA transport in neurites.

3. The authors proposed that YTHDF2 promote distal transportation of select mRNAs through its interaction with FMRP and KIF5C, but evidence showing that the other two reader proteins do NOT interact with FMRP or HUBB3 or KIF5C was not presented. In fact, an interaction between YTHDF1 and FMRP regulated by the phosphorylation state of FMRP has been reported (PMCID: PMC10872974). If the same logic applies, what mechanisms enable YTHDF2 to promote mRNA transport, whereas YTHDF1 does not?

We appreciate the reviewer's suggestion. We understand that this concern is closely related to the point raised in Comment 2, and we hope that *our responses to Comment 2 provides sufficient clarification*.

To further address this question, we performed additional PLA experiments. In our data, YTHDF1–TUBB3 (Extended Data Fig. 8a-b) and YTHDF1–KIF5C PLA signals (Extended Data Fig. 8c-d) were markedly weaker than those observed for YTHDF2, indicating limited association of YTHDF1 with the transport machinery. These results suggest that YTHDF1 preferentially associates with a distinct RNP complex rather than a transport complex.

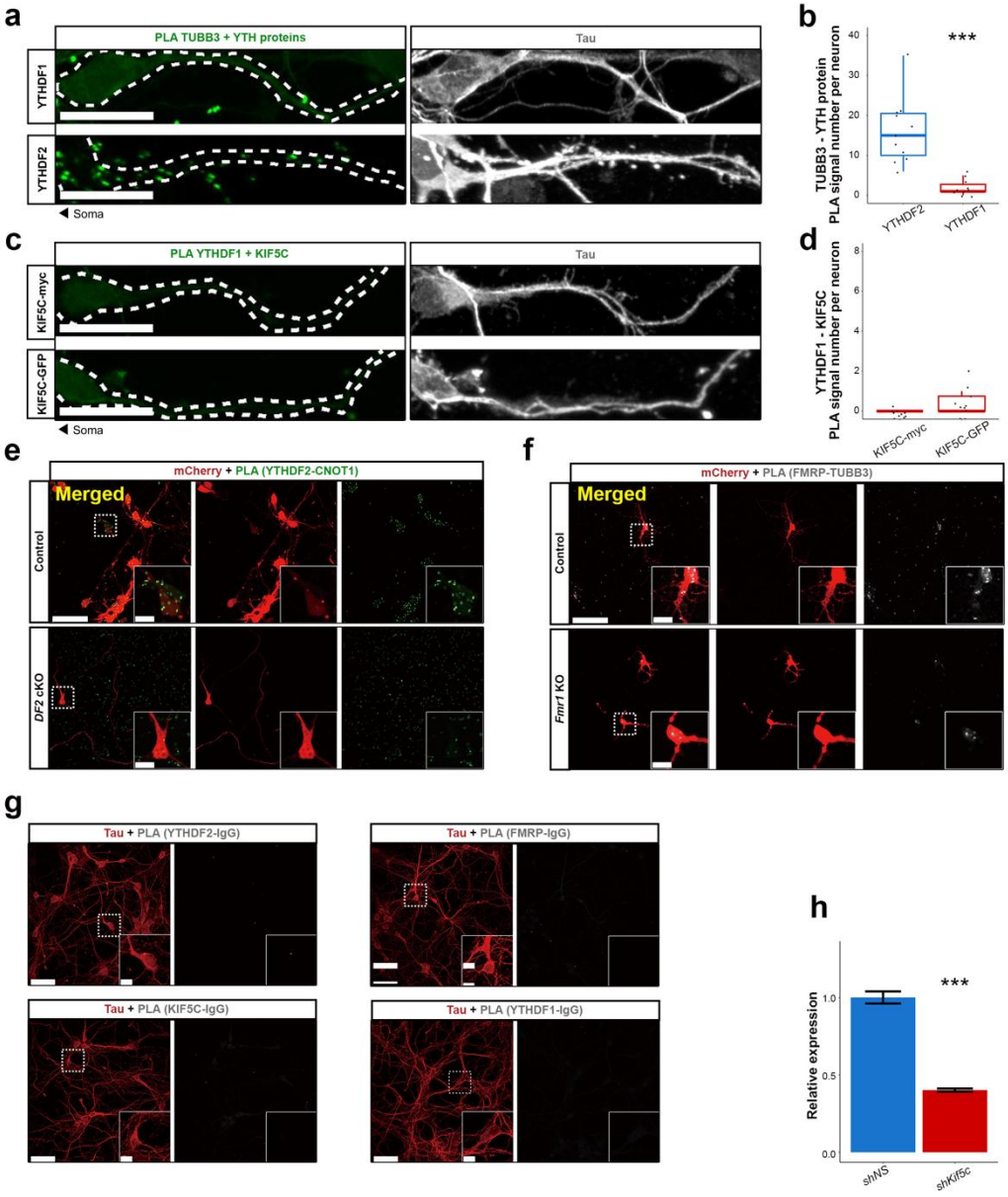

Extended Data Fig. 8. Validation of PLA experiments and YTHDF1 interacting proteins.

(a-b) TUBB3 interacts with YTHDF2, not with YTHDF1. Shown in (a) are representative PLA signals (Green) showing endogenous YTH proteins-TUBB3 association (Scale bar: 20μm). The number of signals per neuron was quantified in (b). **(c-d)** KIF5C not interacts with YTHDF1. Shown in (c) are representative figure of YTHDF1-KIF5C association (Scale bar: 20μm). The number of signals per neuron was quantified in (d). **(e-f)** Validation of Proximity Ligation Assay (PLA) experiments with negative control. YTHDF2-CNOT1 PLA signal significantly reduced in *DF2* cKO represented on **(e)**

(scale bar: 50μm, lower panel scale bar: 10μm). FMRP-TUBB3 PLA signal significantly reduced in *Fmr1* KO represented on **(f)** (scale bar: 50μm, lower panel scale bar: 10μm). Signals appearing in mCherry-negative areas are presumed to originate from cells that were not infected by AAV-mCherry-IRES-Cre viruses. **(g)** YTHDF2, FMRP, KIF5C, and YTHDF1 PLA with IgG control. PLA signal significantly reduced with IgG represented on (c) (scale bar: 50μm, lower panel scale bar: 10μm). **(h)** Validation of *Kif5c* KD in N2A by qPCR. Values represent mean ± SEM after being normalized by GAPDH expression. Significance was evaluated using two-tailed unpaired Student's t-tests (d). ***$P < 0.001$. Statistical details and sample sizes are provided in the supplementary table5.

Finally, as the reviewer noted, Zou et al. (PMID: 37949069) reported that FMRP interacts with YTHDF1 to regulate activity-dependent protein translation. In their Figures 1H and 1I, YTHDF1–RPS6 and YTHDF1–FMRP PLA signals are predominantly localized in the neuronal soma rather than in neurites, further supporting the notion that YTHDF1 functions (translation regulation in the soma) differently from YTHDF2 (mRNA transport in neurites).

Altogether, we suggest that YTHDF1 interacts with the translational machinery, as described in previous studies[1,3], whereas YTHDF2 interacts with the transport machinery in neurites.

Changes in the text:

(Line 365-366) Again, we did not detect a robust interaction between YTHDF1 and KIF5C in neurites (Extended Data Fig. 8c-d).

4. Finally, the mechanism of promoting axonal mRNA transport by YTHDF2 remains unclear. Interactions between YTHDF2 and microtubule, motor proteins, and FMRP do not suggest a positive role of YTHDF2 for transportation. The evidence that does support a positive role of YTHDF2 is the KD and live-cell imaging experiments, however the mechanistic link is unaddressed in these experiments. A shift of mRNAs between granule complexes upon YTHDF2 KD will address this question better than FMRP KD.

We thank Reviewer 1 for this thoughtful suggestion. However, we respectfully disagree with the point that "a shift of mRNAs between granule complexes upon YTHDF2 knockdown would better address this question than FMRP knockdown." In our study, YTHDF2 knockdown reduced neurite localization of target mRNAs and impaired anterograde transport (Fig. 4i–n). While these findings demonstrate the functional role of YTHDF2 in mRNA transport, they do not directly address the mechanistic distinction between YTHDF2-associated degradation and transport complexes.

A central finding of this study is that YTHDF2 recognizes and recruits m^{6}A-modified mRNAs, whereas the downstream fate of these transcripts is determined by context-specific YTHDF2-interacting proteins. These interactions give rise to distinct YTHDF2-containing complexes that mediate either mRNA degradation or transport.

Instead, analysis of protein interactions under *Fmr1* knockdown conditions provides clearer mechanistic insight. For example, we examined the YTHDF2–TUBB3 interaction using PLA and found that YTHDF2 localization to neurite microtubules was significantly reduced upon *Fmr1* knockdown (Revised Fig. 6f–g). We next assessed the YTHDF2–KIF5C interaction and similarly observed a significant reduction following *Fmr1* knockdown (Revised Fig. 6m–n). Together, these results indicate that FMRP facilitates YTHDF2 interactions with motor proteins and neurite microtubules, thereby promoting the distal localization of m^{6}A target mRNAs.

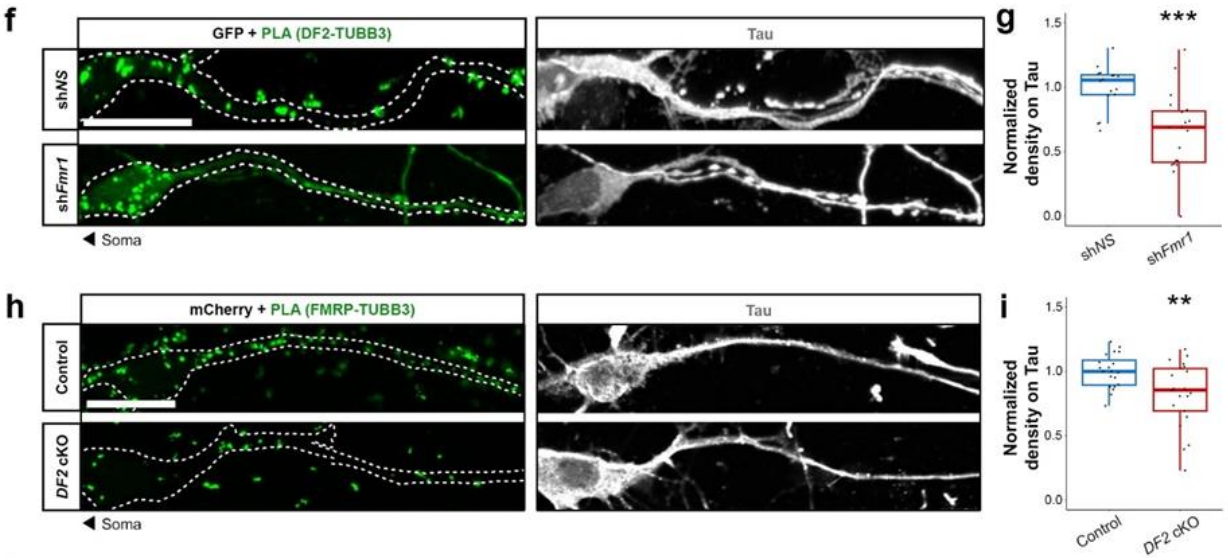

Revised Fig. 6. FMRP interacts with YTHDF2 to assist m^{6}A-tagged mRNA transport to distal neurites of developing neurons.

(f-g) YTHDF2 localization to axons decreased in *Fmr1* KD mouse primary neurons. Shown in (f) are representative PLA signals and Tau staining indicating endogenous YTHDF2-TUBB3 associations in control and *Fmr1* KD mouse primary neurons (Scale bar: 20μm). The relative density on tau is quantified in (g). **(h-i)** FMRP localization to axons decreased in *DF2* cKO mouse primary neurons. Shown in (h) are representative PLA signals and Tau indicating endogenous FMRP-TUBB3 associations in control and *DF2* cKO mouse primary neurons (Scale bar: 20μm). The relative density on Tau is quantified in (i).

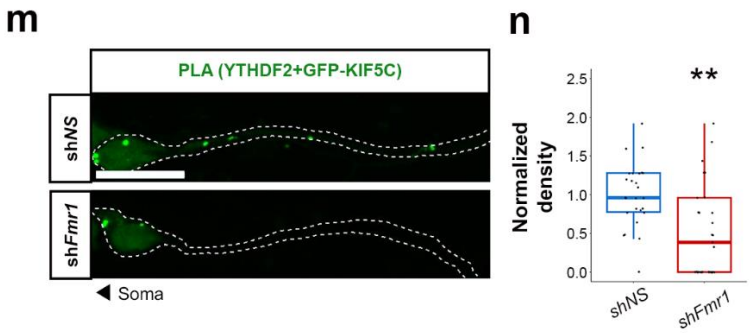

Revised Fig. 6. FMRP interacts with YTHDF2 to assist m^{6}A-tagged mRNA transport to distal neurites of developing neurons.

(m-n) YTHDF2-KIF5C complex localization to distal neurites decreased in *Fmr1* KD mouse primary neurons. Shown in (m) are representative PLA signals showing YTHDF2+GFP-KIF5C association (Scale bar: 20μm). The relative density is quantified in (n).
Significance was evaluated using two-tailed unpaired Student's t-tests (e, g, i, k, l, and n). ns, not significant; $*P < 0.05$, $**P < 0.01$, $***P < 0.001$, $****P < 0.0001$. Statistical details and sample sizes are provided in the supplementary table5.

In addition, knockdown of *Fmr1* significantly increased the interaction between YTHDF2 and CNOT1, indicating that FMRP competitively inhibits the association of m⁶A-tagged mRNAs/YTHDF2 with the mRNA degradation machinery (Revised Fig. 6d–e). These findings further support the model which FMRP facilitates neurite localization of a subset of m⁶A-tagged mRNAs by promoting YTHDF2 interactions with motor proteins and microtubules, while simultaneously limiting target mRNA degradation by competing with the RNA degradation machinery for YTHDF2 binding. We have incorporated these new data into the revised text and Discussion.

We hope that these additional data address Reviewer 1's concern and clarify the mechanistic regulation of YTHDF2-degradation complex and YTHDF2-transport complex by FMRP.

Changes in the text:

(Line 395-406) To evaluate the functional significance of FMRP in the association of YTHDF2 with microtubules, we conducted a PLA experiment between YTHDF2 and TUBB3 in control shRNA (*shNS*) and sh*Fmr1*-treated mouse primary neurons. The results revealed a significant decrease in YTHDF2-TUBB3 PLA signals in the axons of *Fmr1* knockdown neurons compared to those in control neurons (Fig. 6f-g, Extended Data Fig. 9d-e), suggesting that FMRP facilitates the microtubule association of YTHDF2. Conversely, FMRP-TUBB3 PLA signals were markedly reduced in the axons of *Ythdf2* knockout neurons compared to those in control neurons (Fig. 6h-l, Extended Data Fig. 9f-g). In addition, the YTHDF2–KIF5C PLA signal was reduced in *shFmr1*-treated neurons, indicating that FMRP facilitates the association of YTHDF2 with motor proteins in axons (Fig. 6m–n). Collectively, these findings suggest a cooperative interaction between YTHDF2 and FMRP that links m⁶A-tagged mRNAs to microtubules and motor proteins within neurites.

(Line 451-463) Furthermore, FMRP inhibits the interaction of YTHDF2 with the RNA degradation machinery (Fig. 6d-e). These results suggest that m6A-tagged mRNAs are selectively recognized either by the degradation or the transport complex, with FMRP playing a pivotal role in regulating the degradation and transport of m6A-tagged mRNAs. Specifically, FMRP protects a subset of m⁶A-tagged mRNAs from degradation by inhibiting the interaction between YTHDF2 and the RNA degradation machinery, while simultaneously promoting their transport by enhancing the association of YTHDF2 with microtubules and motor proteins (Fig. 6f-g and Fig. 6m-n). Indeed, known FMRP target mRNAs have higher m6A stoichiometry compared to FMRP non-target mRNAs (Extended Data Fig. 9a), and high m6A stoichiometric mRNAs are less affected in their stability compared to low m6A stoichiometric mRNAs upon Mettl14 depletion (Fig. 2g).

Consistently, Drosophila YTHDF directly interacts with FMRP to cooperatively inhibit the translation of mRNAs involved in axonal growth regulation

Minor Comments:

1.Fig 1b, statistics appears only to be applied at the distal part after midline. Please add statistics to the proximal part before midline for a full examination.

We thank the reviewer for this valuable suggestion. We have now included statistical analyses for the proximal bins before the midline (Revised Fig. 1b). In addition, we excluded somatic bins as an experimental control and labeled them with a gray square for improved visualization. The results show that both distal and proximal axon projections are reduced in the *Mettl14* cKO condition compared with the control, indicating that Mettl14 plays a key role in contralateral axon projection.

We apologize for the incorrect information in the initial submission. We have corrected the sample size from “n = 3 per group” to “n = 6 per group” and updated the figure legend accordingly:

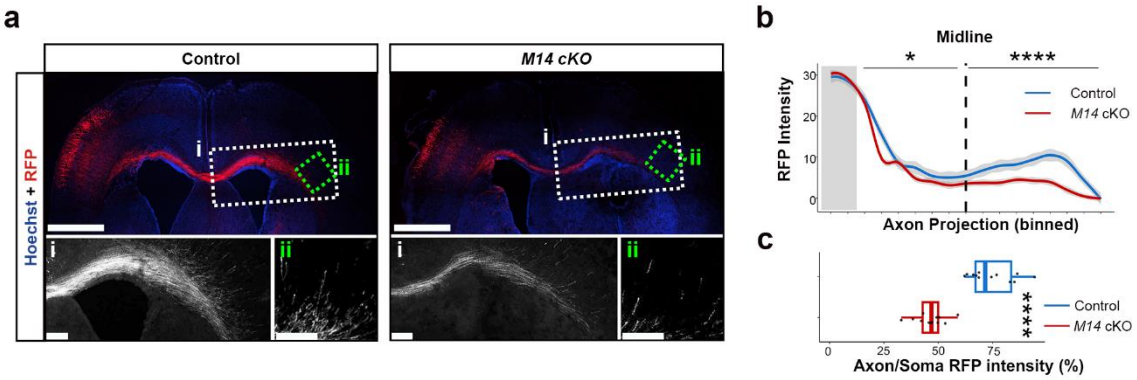

Revised Fig. 1. *Mettl14* deletion during corticogenesis leads to reduced axon projection, shorter neurite length, increased axon collaterals, and slower growth cone dynamics. **(a-c)** Corpus callosal axon projection in control (*Mettl14*$^{+/f}$) and *Mettl14*$^{f/f}$ P5 brains after electroporation of hCRE-IRES-GFP-RV and pCAG-RFP plasmids at E14.5 **(a)** The upper panel shows ipsilateral to contralateral axon projections crossing the white matter and corpus callosum area in coronal sections. The lower panels (i, ii) are selected to magnify the corpus callosum and projected axon terminals (scale bars: 1 mm, i, ii; scale bars: 200 μm). **(b)** The frequency distribution plot represents RFP intensity during axon projections from the ipsilateral to the contralateral position. **(c)** The integrated density of the RFP signal per soma was quantified.

Changes in the text:

(Line 843-847) Callosal axon projection values were normalized by RFP-positive soma (grey zone) and binned by axon projection before and after midline. Contralateral fluorescence intensity of the layer 1~6 values were normalized to relative RFP-positive soma at the ipsilateral position with the S1 region z-stacked image.

2.Fig 1d, RFP signals in the contralateral cortex in cKO appear in abundance next to the inset, possibly comparable to Het (M14f/+ if I understood correctly). The authors need to explain why those signals were excluded from the analysis. Is it possible that the axons are mistargeted to the neighboring region?

We appreciate the reviewer's feedback and apologize for any confusion caused by the presentation of Fig. 1d. We would like to clarify that no RFP signals were manually excluded from our analysis. As described in our previous response, we re-imaged both the soma and the contralateral axon regions at higher magnification for quantification and generation of representative images.

To address this concern, we have provided selected z-stacked raw image sections used for quantification in Reviewer Fig. 2, and we have replaced the lower panel representative image with a z-projected raw image (Revised Fig. 1d). RFP signals in cortical layers above the white matter (WM) were included in the quantification.

Moreover, to minimize any potential confusion, we have adjusted the red and blue channel balance in the upper panel of Revised Fig. 1d.

We have also added a more detailed description in the Methods section outlining how axonal RFP signals were quantified, as follows:

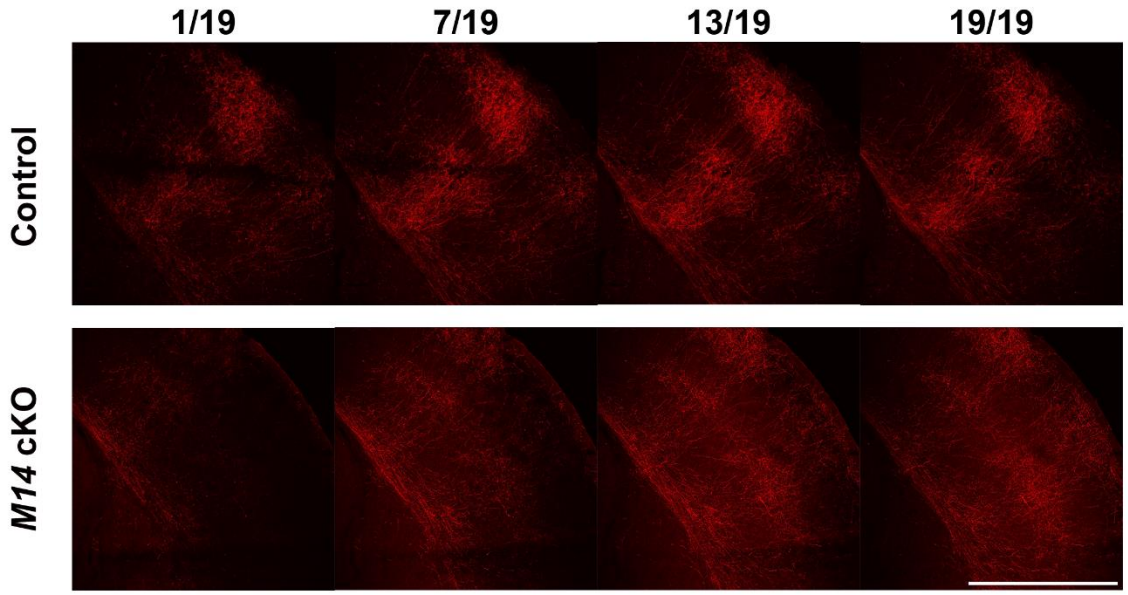

Reviewer Fig. 2. The raw data of Fig. 1d. (scale bars: 1000 μm)

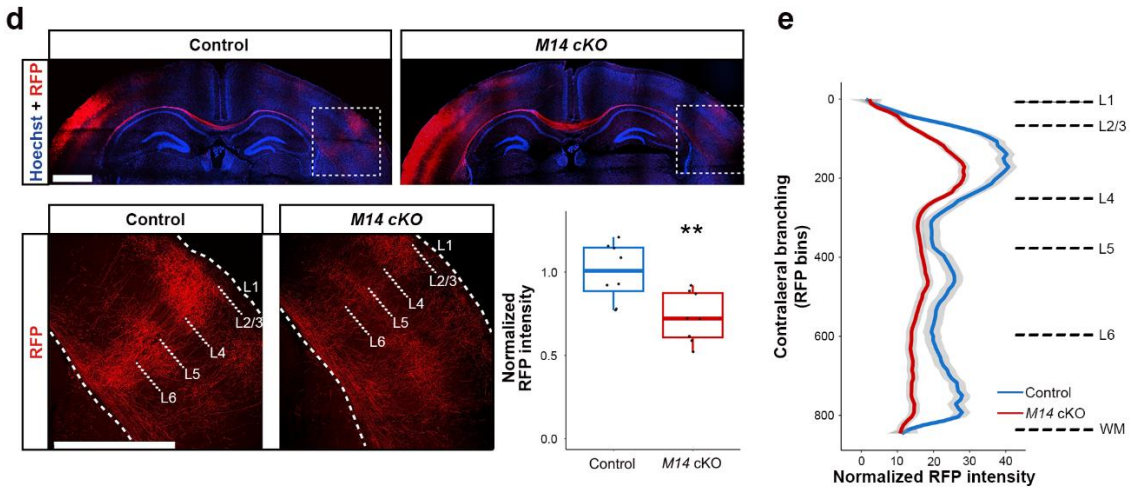

Revised Fig. 1. *Mettl14* deletion during corticogenesis leads to reduced axon projection, shorter neurite length, increased axon collaterals, and slower growth cone dynamics. **(d-e)** Corpus callosal axon projection in control and *Mettl14*$^{f/f}$ P14 brains after electroporation of Dcx-CRE-IRES-GFP and pCAG-RFP plasmids. **(d)** The upper panels show representative images of ipsilateral to contralateral axon projections. The lower panels display z-projected images with higher magnification of axonal arborization in the S1 region. (scale bars: 1 mm). The plot represents the quantitative intensity of RFP in total contralateral branching, projections, and arborization normalized to the RFP^{+} soma intensity of upper-layer neurons. **(e)** Quantitative analysis of contralateral branching distribution along the radial axis of the cortical wall. (confidence level=0.99)

Changes in the text:

(Line 841-847) **Image analysis**

For the acquisition and quantification of images, we utilized the open-source online tool Fiji [8]. To ensure linearity and consistency across samples, minimum and maximum threshold signals were determined. Quantification was performed to obtain binary values from pixel intensity. Callosal axon projection values were normalized by RFP-positive soma (grey zone) and binned by axon projection before and after midline. Contralateral fluorescence intensity of the layer 1~6 values were normalized to relative RFP-positive soma at the ipsilateral position with the S1 region z-stacked image.

3.Fig 1f, the DIV6 cortical neurons appear to have tau staining in the dendrites M14 cKO, resulting in very distinct morphology between Control and M14 cKO. For projection and length analysis, a “filler” will serve better than tau staining. Is it possible that tau is subcellularly mistargeted?

We appreciate the reviewer’s suggestion. To avoid potential confusion, we have decided to go back to mCherry filler, we used in the original submission (Revised Fig. 1f-h). Moreover, we performed quatification again with mCherry filler and result dose not alter our original interpretation.

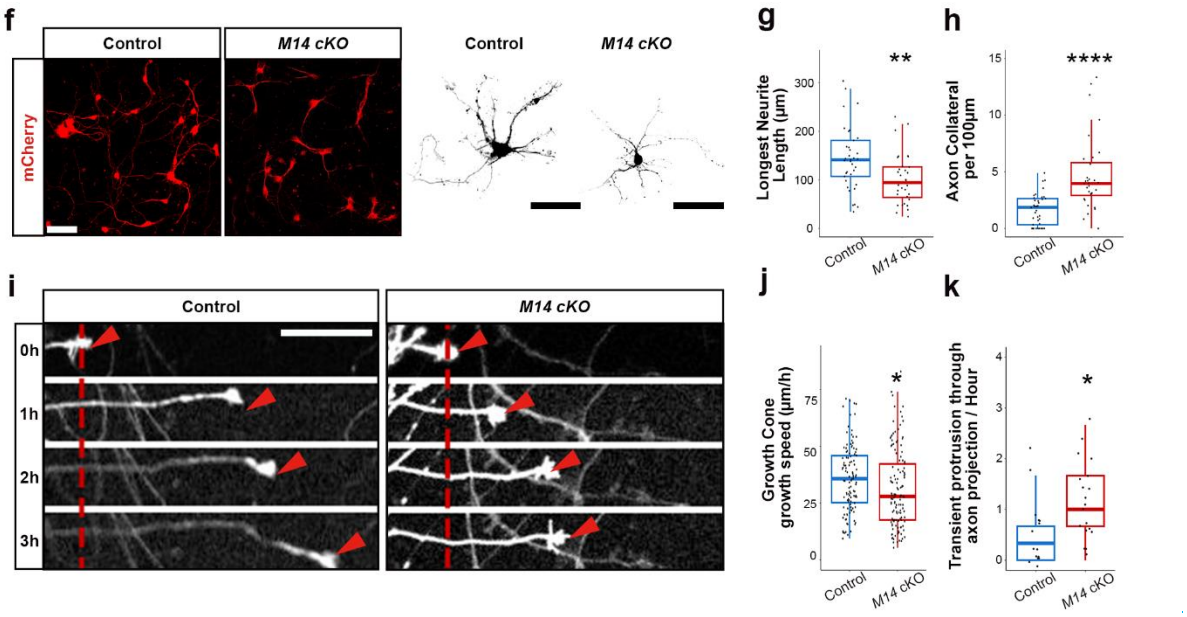

Revised Fig. 1. *Mettl14* deletion during corticogenesis leads to reduced axon projection, shorter neurite length, increased axon collaterals, and slower growth cone dynamics.

(f-k) *M14* cKO primary neurons exhibited abnormal neurite growth at DIV6. Shown in **(f)** are representative confocal images and skeletal images (scale bars: 100 μm). Neurite length and collateral branching frequency were quantified in **(g)** and **(h)**. **(i)** Live imaging of growth cones in control and *M14* cKO neurons over 3 hours at DIV6. Red arrowheads indicate the locations of growth cones (scale bar: 20 μm). Shown in **(j)** is the quantification of total growth length divided by tracking time and **(k)** is the quantification of the transient protrusion. Significance was evaluated using two-tailed unpaired Student's t-tests (c, d, g, h, and j). The significance of RFP intensity across the midline was evaluated using two-way ANOVA (b). **P* < 0.05, ***P* < 0.01, *****P* < 0.0001. Statistical details and sample sizes are provided in the supplementary table5.

4.Fig 1k, For "Transient protrusion through axon projection/ Hour" quantification, please demonstrate the representative images to help readers understand what is being quantified.

We appreciate the reviewer's suggestion. We have added a representative image of "transient protrusions" to Supplementary Figure 1 (Revised Extended Data Fig. 1k), indicated by a red arrow. We have also clarified the method used to quantify "transient protrusions per axon projection per hour" in the Image Analysis section, as described below:

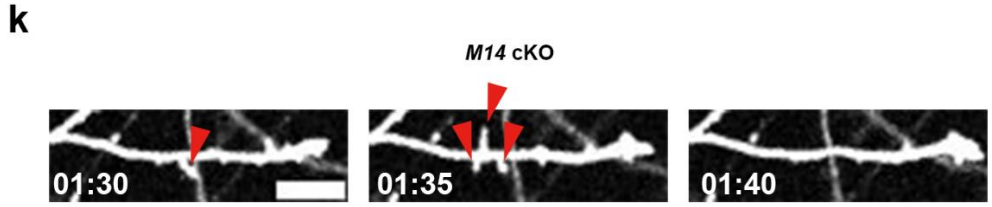

Revised Extended Data Fig. 1. Loss of Mettl14 leads to reduced contralateral axon projection. (k) The transient protrusion detected (red arrow) during *M14* cKO neuron live imaging. (scale bars: 20 μm)

Changes in the text:

(Line 847-850) For tracking in vitro primary neuron samples, the Fiji plugin NeuronJ was used. The neurite length was measured as the distance between a clearly identifiable neurite tip and the center of the nucleus along axonal tracks labeled with Tau. The protrusion transiently disappeared within 15 min were counted during neuron live imaging.

5.Fig 3b, this figure compares stabilization with localization in M14cKO/ WT, but the authors do not clarify if the localization is for neurites or axons.

We appreciate the reviewer's suggestion. Although we previously stated that the corpus callosum (CC) is enriched in axons in the previous paragraph— "we conducted RNA-seq using microdissected tissue from the axon-enriched CC of cortical projection neurons (layer 2/3) at P4 (referred to as CC-seq)" —we agree that each figure should include a clear, self-contained definition. To address this, we have revised the description of Fig. 3b as follows:

Changes in the text:

(Line 210-212) To further investigate the relationship between RNA stability and localization, we compared our axon-enriched CC-seq results with the RNA stability assay in WT and M14 cKO primary neurons

6.Fig 3g, earlier smFISH experiments show staining(e) and quantification of distance from soma (f) for the transcript of interest but panel g mentions the relative density of smFISH puncta in neurites which is not shown in e or in extended figures.

In the previous round of peer review, we agreed with this reviewer's feedback that *"distance from the nucleus" alone is insufficient to assess axonal distribution and that a measure of "density" should be included*. To address this, we reanalyzed the same images and quantified the density of the smFISH/PLA signals. As indicated in the figure legend, Fig. 3e provides representative images corresponding to the quantifications shown in Figs. 3f and 3g.

7.Fig 3i-n,Why different time stamps (3i, 3l) are displayed when showing the anterograde/retrograde/interrupted RNA localization. Also, what is "interrupted"? For how long were the granules tracked? Please clarify.

RNA molecules in neurites exhibit extremely rapid (~3 μm/s) and unpredictable movement during MS2-based live imaging, making it technically challenging to present different experimental conditions using identical time scales. Accordingly, we display representative examples of clearly moving "anterograde" granules within a 30-second time window in the control group, and "interrupted" granules over a 5-minute time window in the *Mettl14* cKO, m^6A mutant reporter, and *Ythdf2* cKO groups, capturing their behavior across the full imaging period. Collectively, these data highlight our key message: depletion of m^6A or its reader proteins reduces anterograde RNA transport in neurites.

We have already provided a detailed definition of "interrupted" granules in the Methods section and

in our previous response letter, with appropriate references, as follows:

(Line 856-860) For RNA live images, RNA molecules observed > 60 frames were selected for consistency. Movements longer than 2 μm were categorized to antero or retro group and less than 2 μm were categorized as interrupted group[9].

Also, we have also provided a detailed description of the RNA live imaging methodology in the Methods section and in our previous response letter, as follows:

(Line 633-639) For the RNA live imaging, we co-electroporated phage-ubc-nls-ha-tdMCP-gfp, with pcDNA-puro-TagBFP-β-ACTIN-3′UTR-24xMS2 reporters which retains the endogenous 3′UTR m^{6}A motif (the 1217th position, 5nt after the STOP codon) to cortical neurons on a confocal glass-bottom dish and culture to the DIV5~6. Live images were acquired with a Nikon Eclipse Ti inverted microscope equipped with a CSU-10 spinning disk (Yokogawa, Tokyo, Japan), an EMCCD camera, and a 100× oil immersion objective (NA 1.49) for 5minutes with 500ms intervals.

8.Fig 3j, m, it appears that there are differences in the retrograde RNA location as well, however this was not addressed by the authors. A graph before normalization may also help address this question.

We thank the reviewer for raising this important point. In the previous revision, we performed RNA live imaging to directly demonstrate reduced RNA motility in the *Mettl14* cKO, m^{6}A mutant reporter, and *Ythdf2* cKO conditions. However, the percentage bar graphs in Fig. 3j and 3m may have led to confusion, suggesting decreased anterograde movement and increased retrograde movement.

To address this, we revised the statistical analysis from a chi-square test to a t-test to better reflect our comparisons and improve clarity (Revised Fig. 3j, m). We also provide Reviewer Fig. 3 with detailed analysis of retrograde RNA motility, showing that it is not significantly altered by m^{6}A depletion.

In addition, we performed additional rounds of RNA live imaging using the m6A mutant reporter to confirm reproducibility.

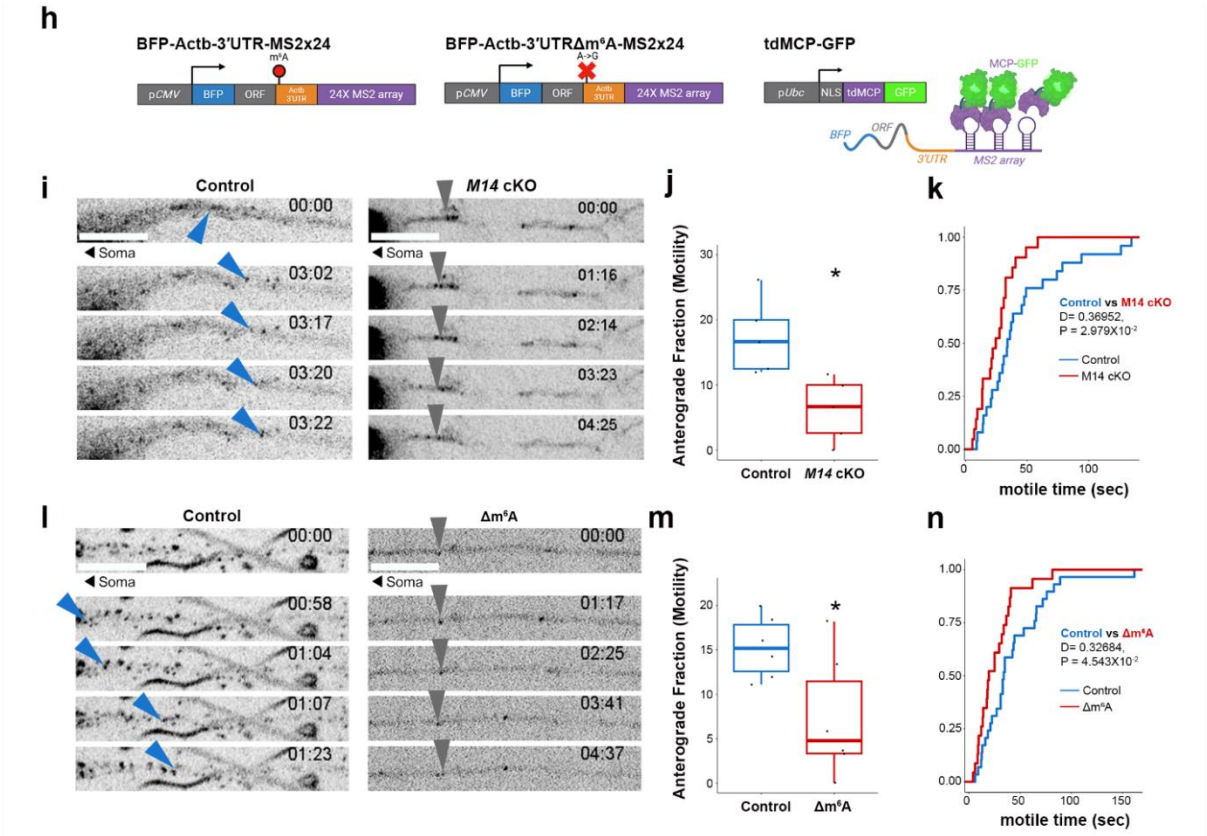

Revised Fig. 3. m^{6}A modification is crucial for the distal translocation of cytoskeletal mRNAs in differentiating neurons. (h) The schematic diagram of the RNA live imaging MS2 system. **(i-k)** *M14* cKO primary cultured neurons show depleted anterograde RNA localization. Shown in (i) anterograde (blue arrowheads) and interrupted (grey arrowheads) RNA reporter are indicated (scale bars: 10 μm). The anterograde fraction of RNA reporter motility was quantified in (j) and the total motile time of RNA granules was compared with each condition in (k). **(l-n).** The m^{6}A point-mutated reporter granules showed depleted anterograde RNA localization. Shown in (l) anterograde (blue arrowheads) and interrupted (grey arrowheads) RNA reporter granules are indicated (scale bars: 10 μm). The anterograde fraction of RNA reporter motility was quantified in (m) and the total motile time of RNA granules was compared with each condition in (n). Significance was evaluated using two-tailed unpaired Student's t-tests (f, g, j, and m). The significance of two RNA motility time sets was evaluated using the Kolmogorov-Smirnov test (k, n). ns, not significant, $*P < 0.05$, $**P < 0.01$, $***P<0.001$, $****P < 0.0001$. Statistical details and sample sizes are provided in the supplementary table5.

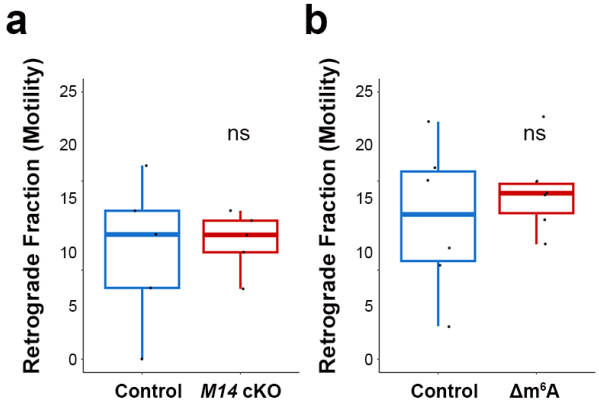

Reviewer Fig. 3. Retrograde RNA localization not affected by *M14* cKO and m^{6}A deletion. (a) The retrograde fraction of RNA reporter motility in control and *M14* cKO was quantified in (a). (n=5 for each, *P*=0.7869) **(b)** The retrograde fraction of RNA reporter motility in control and m^{6}A point-mutation was quantified in (a). (n=6 for each, *P*=0.4587) Significance was evaluated using two-tailed unpaired Student's t-tests (a and b). ns, not significant.

9.Fig 4b: Statistical analysis could be applied before the "midline" in order to highlight the significant difference at the contralateral side.

We thank the reviewer for this valuable suggestion. As noted in Minor Point #1, we have added statistical analyses for the proximal region before the midline, as well as the somatic region as an experimental control (Revised Fig. 4b). In addition, the soma is now labeled with a gray square for clarity. The results show that both distal and proximal axon projections are reduced in the *Ythdf2* cKO condition compared with the control, indicating that YTHDF2 plays a key role in contralateral axon projection.

We apologize for the incorrect information in the initial submission. We have corrected the sample size from "n = 3 per group" to "n = 6 per group" and updated the figure legend and Methods section accordingly:

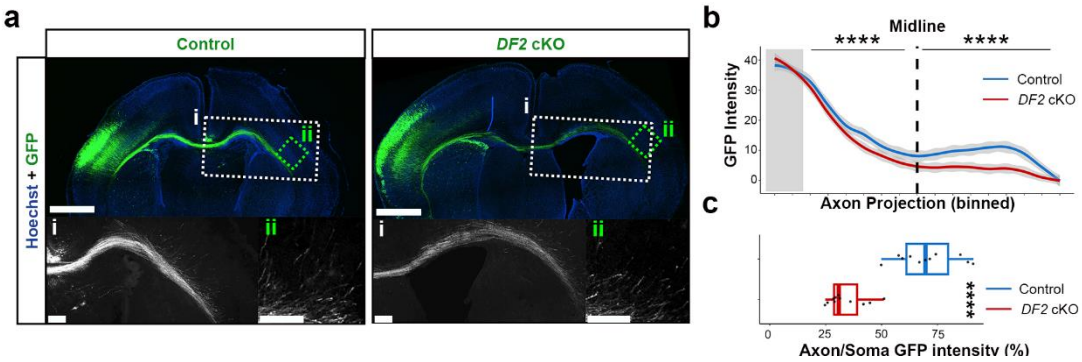

Revised Fig. 4. *Ythdf2* deletion reduces axonal projection and neurite length and impairs growth cone dynamics in *DF2* cKO. (a-c) Corpus callosal axon projections in control (*YTHDF*$^{+/f}$) and *YTHDF2*$^{f/f}$ cKO P5 brains, examined by *in utero* electroporation. **(a)** The upper panel shows ipsilateral to contralateral axon projections crossing the white matter and corpus callosum area in coronal sections. The lower panels (i, ii) are selected to magnify the corpus callosum and projected

axon terminals (scale bars: 1 mm, i, ii; scale bars: 200 μm). **(b)** The frequency distribution plot represents GFP intensity during axon projections from the ipsilateral to the contralateral position. (confidence level=0.99). **(c)** The integrated density of the GFP signal of axons per soma was quantified.

Changes in the text:

(Line 843-847) Callosal axon projection values were normalized by RFP-positive soma (grey zone) and binned by axon projection before and after midline. Contralateral fluorescence intensity of the layer 1~6 values were normalized to relative RFP-positive soma at the ipsilateral position with the S1 region z-stacked image.

10.Fig 4f: Please clarify in the text/methods what "transient protrusion" means in this panel.

We appreciate the reviewer's suggestion. We have added a representative image of "transient protrusions" to Supplementary Figure 7 (Revised Extended Data Fig. 7a), indicated by a red arrow. We have also clarified the method used to quantify "transient protrusions per axon projection per hour" in the Image Analysis section, as described below:

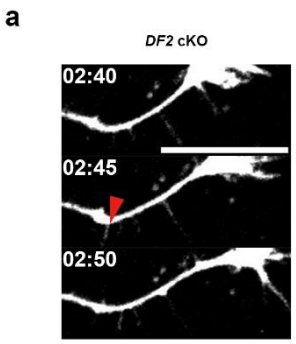

Revised Extended Data Fig. 7. Loss of *Ythdf2* leads to a disrupted RNA localization and neuron projection. (a) The transient protrusion detected (red arrow) during *DF2* cKO neuron live imaging. (scale bars: 20 μm)

Changes in the text:

(Line 847-850) For tracking in vitro primary neuron samples, the Fiji plugin NeuronJ was used. The neurite length was measured as the distance between a clearly identifiable neurite tip and the center of the nucleus along axonal tracks labeled with Tau. The protrusion transiently disappeared within 15 min were counted during neuron live imaging.

11.Fig 4h, The panel discussing M14 when the focus is YTHDF2's role in axonal projection, is confusing. Is this information important for interpreting the proceeding panels?

We appreciate the reviewer's suggestion. Although we initially found the negative correlation between Mettl14-dependent stability and YTHDF2-dependent stability to be interesting, this comparison is not directly related to our central hypothesis. We agree that it is not essential for interpreting the role of YTHDF2 in axonal projection. To avoid potential confusion, we have removed the Mettl14–YTHDF2 stability comparison data from the manuscript (previously Fig. 4h).

Accordingly, we have revised the text as follows:

Changes in the text:

(Line 305-308) Unexpectedly, m6A-modified transcripts showed only a slight stability change in the DF2 cKO condition (Fig. 4g, Supplementary Table 3). ~~We compared the stability difference in the DF2 cKO condition with the stability difference in the M14 cKO condition (Extended Data Fig. 2f) for each gene. In fact, the relative differences of RNA stability in DF2 and M14 cKO compared to controls show a weak negative correlation, especially on m6A-modified genes. For example, the stability of Ncam1, Cntn1, and Ank2 mRNAs increased in M14 cKO condition, while their stability decreased in the DF2 cKO condition (Fig. 4h).~~ Altogether, we hypothesized that YTHDF2 does not simply degrade RNAs in neuronal context and may protect and promote distal localization of selected mRNA.

12.Fig 4l, It would be helpful to show a representation of the "retrograde" movement and what its relevance is to DF2's role in axonal trafficking.

We thank the reviewer for raising this issue. In the previous revision, we performed RNA live imaging to directly demonstrate reduced RNA motility in the *Mettl14* cKO, m^{6}A mutant reporter, and *Ythdf2* cKO conditions. However, the percentage bar graphs in Fig. 4l and 4m may have caused confusion, suggesting decreased anterograde movement and increased retrograde movement.

To address this, we revised the statistical analysis from a chi-square test to a t-test to better align with our comparisons and improve clarity (Revised Fig. 4l). In addition, we provide Reviewer Fig. 4 with detailed analysis of retrograde RNA motility, showing that it is not significantly altered by m^{6}A depletion.

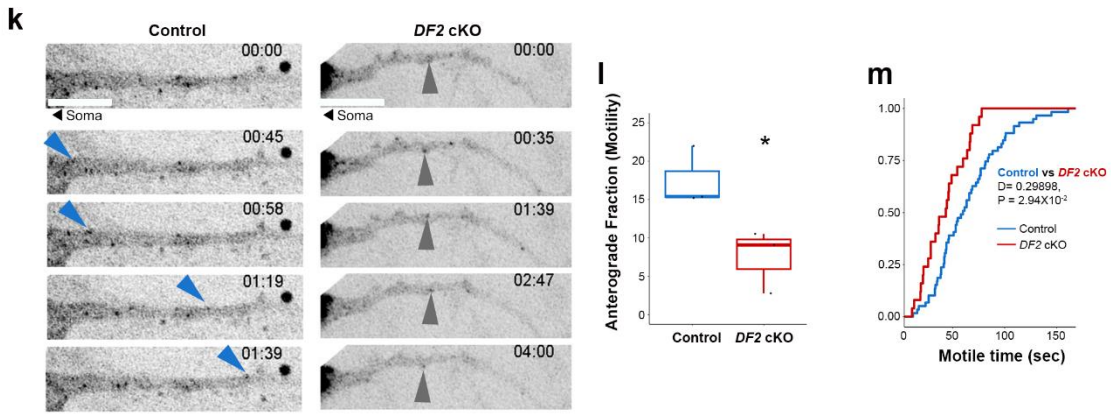

Revised Fig. 4. *Ythdf2* deletion reduces axonal projection and neurite length and impairs growth cone dynamics in *DF2* cKO. (k-m) *DF2* cKO primary cultured neurons show depleted anterograde RNA localization. Shown in (k) anterograde (blue arrowheads) and interrupted (grey arrowheads) RNA reporter granules are indicated (scale bars: 10 μm). The anterograde fraction of RNA reporter motility was quantified in (l), and the total motile time of RNA granules was compared with each condition in (m). The significance was evaluated using two-tailed unpaired Student's t-tests (c, e, f, g, i, j, and l). The significance of GFP intensity across the midline was evaluated using two-way ANOVA (b). The significance of RNA motility time sets was evaluated using the Kolmogorov-Smirnov test (m). ns, not significant, *$P < 0.05$, **$P < 0.01$, ***$P<0.001$, ****$P < 0.0001$. Statistical details and sample sizes are provided in the supplementary table5.

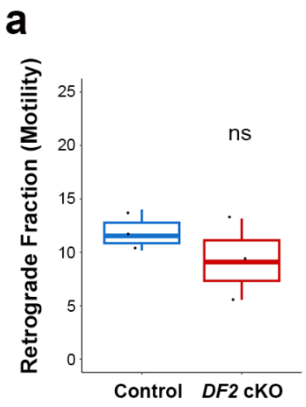

Reviewer Fig. 4. Retrograde RNA localization not affected by *DF2* cKO. (a) The retrograde fraction of RNA reporter motility in control and *DF2* cKO was quantified in (a). (n=3 for each, *P*=0.3455) Significance was evaluated using two-tailed unpaired Student's t-tests (a and b). ns, not significant.

13.Fig 4j-m: A lot of information (eg. n numbers, p-values) is given. I suggest the authors organize the information to be given in a more concise/organized manner.

We appreciate reviewer's suggestion. We move the detailed statistics to the Supplementary Table 5 for the overall figure legends and organize the information in order.

14. Fig 5b, According to the text, 283 proteins showed reduced DF2 interaction while 87 had enhanced interaction in DF2-cKO versus WT mice. This is not reflected in the graph.

We quantified protein expression using PSM values, which are inherently discrete and therefore yield integer-based measurements. As a result, the plotted data points appear limited. To provide a more comprehensive view, we have already included a Table S4 showing protein expression changes between *Mettl14* WT and cKO. We did not perform the same analysis for *Ythdf2* WT and cKO, and thus focus here on the functional role of YTHDF2 in the context of m^{6}A.

Furthermore, we update the text for the clear LC-MS/MS target filtering matched with Fig. 5b as below:

Changes in the text:

(Line 787-791) LC-MS/MS analysis-based protein expression levels are calculated by normalizing the PSM value of the Ythdf2 antibody pull-down sample with the IgG control sample and significantly changed proteins were identified by Log2foldchange > |0.5|. Gene ontology-based compare cluster analysis and gene-concept network analysis were conducted with the R package clusterProfiler (v 4.6.2).

15.Fig 5 legend - "Red circles highlight proteins involved in transport system as categorized by

gene ontology analysis" - labeling method of 'transport-relevant' / microtubule proteins is confusing to readers.

We agree that this simplified description of gene ontology categories may be unclear. To address this, we have revised the legend to more precisely reflect the specific terms used in the graph.

Changes in the text:

(Line 1014-1015) Red circles highlight proteins involved in the RNA localization process (GO:0006403).

16.Fig 5f, g: Experiments done on N2A and HEK293T cells show that DF2 and KIF5C or FMRP, respectively, interact with one another. However, these experiments do not show their interactions are dependent on m6A, particularly m6A modifications on the interacting mRNAs.

We had already performed co-immunoprecipitation of YTHDF2 followed by mass spectrometry in WT and *Mettl14* cKO brain tissue (Fig. 5a–d), which revealed m^6A-dependent interactions between YTHDF2 and KIF5C or FMRP. In addition, YTHDF2–KIF5C PLA experiments showed significantly higher PLA signals in WT neurons compared to Mettl14 cKO neurons (Fig. 5n–o), further supporting m^6A-dependent interactions between YTHDF2 and KIF5C.

Together, these results provide evidence that these interactions are m^6A-dependent under physiologically relevant conditions.

17.Fig 5k-m: Transition from DF2-TUBB3 interaction (5h-j) to the role of KIF5C in this interaction is unclear.

We appreciate reviewer's suggestion. While we already described the importance of the neuron specific motor protein KIF5C in the former LC-MS/MS and Co-IP paragraphs, but not on the PLA part. To address this, we have revised the text to improve the logical transition, as follows:

Changes in the text:

(Line 354-361) The results revealed a significant reduction in PLA signals in the axons of *M14* cKO neurons compared to those in the axons of WT neurons. This observation suggests that m^6A modification is crucial for the interaction between YTHDF2 and microtubules in the axons (Fig. 5h-j, Extended Data Fig. 8a-e). So, we hypothesize this interaction is mediated by neuron-specific motor proteins such as KIF5C. To address this, we performed YTHDF2-TUBB3 PLA after the knockdown of *Kif5c*, a neuron-specific motor protein, in primary cortical neurons.

18.Fig 6d is insufficient to support the claim that YTHDF2 interacts with two protein complexes (presumably CNOT1-DF2-FXR versus DF2-FMRP-KIF5C). A staining of CNOT1 – DF2 – FMR1 – quantifies co-localization is required. SuperRes imaging of either SIM or STORM would be helpful. Biochemical analysis such as co-immunoprecipitation will also do.

We appreciate the reviewer's suggestion. However, triple staining of CNOT1, YTHDF2, and FMRP is technically challenging due to limitations in antibody host compatibility. In addition, CNOT1 immunostaining yields highly diffuse signals, which preclude precise subcellular localization and reliable co-localization analysis.

In contrast, the Proximity Ligation Assay (PLA) enables direct visualization of protein–protein interactions in situ and is widely used in neuroscience to resolve interactions at high spatial resolution[10–13]. We therefore consider PLA to be a more suitable approach for addressing this question.

Moreover, conventional co-immunoprecipitation from whole-cell lysates cannot distinguish between distinct protein complexes or their spatial context. For these reasons, we believe that our PLA-based analyses provide more relevant and informative evidence for the existence of functionally distinct YTHDF2-associated complexes.

19.Fig 6 (d-e): There is a typo in the figure legend which does not match the quantification in the figure. It says “YTHDF2-CNOT1 associations decreased in Fmr1 KD mouse primary neurons.”, whereas there is an increase following Fmr1 KD.

We apologize for the incorrect description in the original figure legend (Revised Fig. 6d). We have corrected the legend as follows:

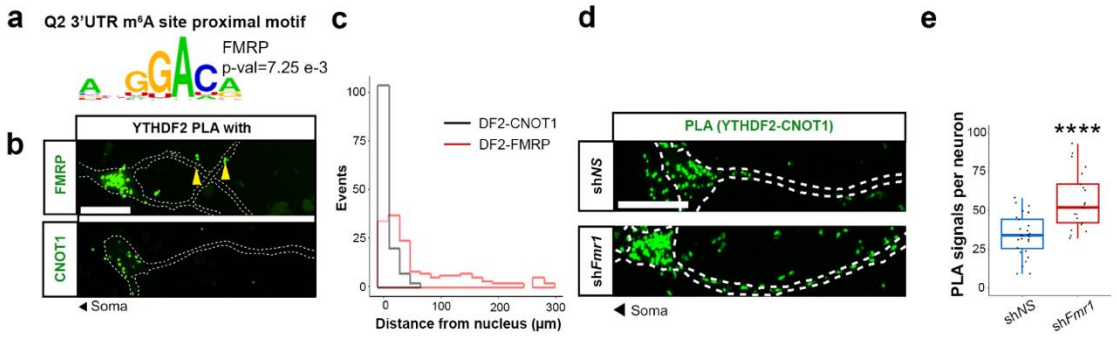

Revised Fig. 6. FMRP interacts with YTHDF2 to facilitate transport of m⁶A-tagged mRNAs to distal neurites in developing neurons.
(a) Motif enrichment analysis of the Q2 3’UTR m^{6}A proximal sequence (±50 bp). **(b-c)** YTHDF2 is associated with functional cofactors in different subcellular locations. Shown in (b) are representative PLA signals (green), representing endogenous YTHDF2-CNOT1 and YTHDF2-FMRP associations (Scale bar: 20μm). The yellow arrowheads indicate PLA signals in the distal neurites. The distribution of PLA signals in neurites is quantified in (c). **(d-e)** YTHDF2-CNOT1 associations increased in *Fmr1* KD mouse primary neurons. Shown in (d) are representative PLA signals (green) indicating endogenous YTHDF2-CNOT1 associations in control and *Fmr1* KD mouse primary neurons (Scale bar: 20μm). The number of PLA signals per neuron was quantified in (e) (Control: n=28, *Fmr1* KD: n=21, *P*=9.43e-06).

20.Lines 22, 41, 147, etc: replace “base-pair” with “nucleotide”.

We appreciate reviewer’s suggestion. We replaced “base-pair” to “nucleotide” as below:

(Line 22) A single nucleotide resolution map of m6A epitranscriptome in the postnatal brain suggests an additional function of m6A modification beyond mRNA degradation

(Line 41) Furthermore, m6A-SAC-seq to identify a single nucleotide resolution m6A maps in the perinatal brain uncovers m6A-tagged transcripts associated with synapse organization,

(Line 95) Employing a single nucleotide resolution m6A profiling using m6A-selective allyl chemical

labeling and sequencing (m6A-SAC-seq),

(Line 147-149) A single nucleotide resolution, quantitative m6A mapping reveals transcripts related to axon development with high m6A stoichiometry

To investigate the landscape of the m6A epitranscriptome in the brain at single nucleotide resolution, we used m6A-SAC-seq on the P0 mouse forebrain (Extended Data Fig. 2a).

(Line 427) A single nucleotide resolution m6A mapping and microdissected axon RNA-seq identified m6A-tagged mRNAs related to cytoskeletal regulation.

(Line 935) Fig. 2. A single nucleotide resolution, quantitative m6A mapping revealed transcripts related to axon development with high m6A stoichiometries

(Line 1094) Extended Data Fig. 2. Unique characteristics of single nucleotide resolution m6A map in the developing brain through m6A-SAC-seq.

21.Line 91, 111, PMID: 40402742 directly addresses this question.

We have added this reference to the Discussion section.

22.Line 139 “formation of distal neuronal processes is impaired”. What mechanisms may support specific deficits in forming “distal” neuronal processes?

We appreciate the reviewer’s suggestion. To avoid overinterpretation, we have revised the text to more directly reflect our experimental data, as follows:

(Line 137-140) We observed a significant reduction in the longest neurite length of M14 cKO neurons and an increase in axon collateral branching compared with control neurons at DIV6 (Fig. 1f-h), suggesting that the neurite development is impaired after m^{6}A depletion.

23.Line 196-200, better suit discussion.

We removed the sentence from the text.

(Line 193-198) Of note, the results of m^{6}A-SAC-seq and mRNA stability assay imply that high m^{6}A stoichiometry transcripts related to axon development (Fig. 2h, Extended Data Fig. 3e) are not solely regulated at the level of RNA stability as previously described [14]. ~~One possible explanation is that m^{6}A-tagged transcripts are differentially associate with effector complexes—some promoting decay, others conferring stability—resulting in variable m^{6}A stoichiometry among transcript populations.~~ This suggests that m^{6}A may exert additional functions beyond promoting mRNA degradation, potentially influencing mRNA localization, translation efficiency, or RNP complex stabilization in neurons.

24.Line 238-239, why not translation of the target proteins?

We appreciate the reviewer’s suggestion. Our smFISH experiments indicate that Ncam1, Cntn1, Ank2, and Actb mRNAs are already reduced in neurites in *Mettl14* cKO neurons compared with controls, prior to translation. While we cannot exclude a role for local translation in further regulating these mRNAs, we are pursuing this question in a separate study.

25.Line 240-253. m6A-Actb-MS2 reporter showed an overall reduced motility in M14 KO neurons,

whereas deltam6A-Actb-MS2 showed deficits in anterograde movement. How to reconcile the difference in phenotypes?

We apologize missing the description of overall reduced motility in the Δm⁶A-Actb-MS2 RNA live imaging and thanks to reviewer raising this issue. (Revised Fig. 3n) To address this, we add a sentence as below:

(Line 248-251) As a result, anterograde RNA movement was markedly reduced in the Δm⁶A reporter (Fig. 3l-m, Extended Movie 5,6). Also, the total motile time of RNA was reduced in the Δ m⁶A reporter (Fig. 3n). These findings demonstrate that a single m⁶A modification within the 3′UTR is critical for efficient anterograde transport of Actb mRNAs in developing neurons.

26. Lines 307-308, it is unclear what dataset “m6A-modified transcripts” refer to or where the mRNA stability dataset is used.

We apologize missing data citation. We cited *Ythdf2* cKO RNA stability assay dataset to the text as bellow:

(Line 305-306) Unexpectedly, m⁶A-modified transcripts showed only a slight stability change in the *DF2* cKO condition (Fig. 4g, Supplementary Table 3).

27.Lines 315, 321, replace “selected” with “select”..

We appreciate the reviewer’s suggestion. However, we have retained the term “selected” rather than “select,” as “select mRNA” is not grammatically appropriate in this context.

1. Broix, L. *et al.* m6A RNA methylation-mediated control of global APC expression is required for local translation of β-actin and axon development. *Cell Rep.* **44**, 115727 (2025).
2. Zaccara, S. & Jaffrey, S. R. A Unified Model for the Function of YTHDF Proteins in Regulating m6A-Modified mRNA. *Cell* **181**, 1582-1595.e18 (2020).
3. Zaccara, S. & Jaffrey, S. R. Understanding the redundant functions of the m6A-binding YTHDF proteins. *Rna* **30**, 468–481 (2024).
4. Lasman, L. *et al.* Context-dependent functional compensation between Ythdf m6A reader proteins. *Genes Dev.* **34**, 1373–1391 (2020).
5. Chen, Y. *et al.* O-GlcNAcylation determines the translational regulation and phase separation of YTHDF proteins. *Nat. Cell Biol.* **25**, 1676–1690 (2023).
6. Sikorski, V., Selberg, S., Lalowski, M., Karelson, M. & Kankuri, E. The structure and function of YTHDF epitranscriptomic m6A readers. *Trends Pharmacol. Sci.* **44**, 335–353 (2023).
7. Zou, Z., Sepich-Poore, C., Zhou, X., Wei, J. & He, C. The mechanism underlying redundant functions of the YTHDF proteins. *Genome Biol.* **24**, 17 (2023).
8. Schindelin, J. *et al.* Fiji: an open-source platform for biological-image analysis. *Nat. Methods* **9**, 676–682 (2012).

9. Bauer, K. E. *et al.* Live cell imaging reveals 3′-UTR dependent mRNA sorting to synapses. *Nat. Commun.* **10**, 3178 (2019).

10. Vitet, H. *et al.* Huntingtin recruits KIF1A to transport synaptic vesicle precursors along the mouse axon to support synaptic transmission and motor skill learning. *Elife* **12**, e81011 (2023).

11. Cardoso Dos Santos, L. M. *et al.* Apelin is expressed in intimal smooth muscle cells and promotes their phenotypic transition. *Sci. Rep.* **13**, 18736 (2023).

12. Alegre-Martí, A. *et al.* A hotspot for posttranslational modifications on the androgen receptor dimer interface drives pathology and anti-androgen resistance. *Sci. Adv.* **9**, eade2175 (2026).

13. Avallone, M. *et al.* Visualizing Arc protein dynamics and localization in the mammalian brain using AAV-mediated in situ gene labeling. *Front. Mol. Neurosci.* **Volume 16-2023**, (2023).

14. Loedige, I. *et al.* mRNA stability and m6A are major determinants of subcellular mRNA localization in neurons. *Mol. Cell* **83**, 2709–2725 (2023).